

**DEVELOPMENT OF NANOPARTICLES LOADED 3D PRINTED  
MICROCHANNEL FOR FLUORIDE REMOVAL FROM WATER**

**A thesis submitted to the  
*University of Petroleum and Energy Studies***

For the award of  
***Doctor of Philosophy***  
in  
Electrical and Electronics Engineering

BY  
Ravi Kumar Patel

June 2020

**Supervisor(s)**

Dr. Jitendra Kumar Pandey  
Dr. Amit Kumar Chawla



**Research and Development  
School of Engineering  
University of Petroleum & Energy Studies  
Dehradun - 248007: Uttarakhand**

# **DEVELOPMENT OF NANOPARTICLES LOADED 3D PRINTED MICROCHANNEL FOR FLUORIDE REMOVAL FROM WATER**

**A thesis submitted to the  
University of Petroleum and Energy Studies**

For the award of  
*Doctor of Philosophy*  
in  
Electrical and Electronics Engineering

BY  
Ravi Kumar Patel  
SAP ID 500057321

June 2020

Supervisor

Prof. (Dr.) Jitendra Kumar Pandey  
*Associate Dean-Research*  
University of Petroleum and Energy Studies

Co-Supervisor

Assoc. Prof. (Dr.) Amit Kumar Chawla  
University of Petroleum and Energy Studies



**Research and Development  
School of Engineering  
University of Petroleum & Energy Studies  
Dehradun - 248007: Uttarakhand**

*Dedicated*

*To*

*My father,*

*Lal Bahadur Patel*

*And*

*My mother,*

*Chhohagi Devi*

**June 2020**

**DECLARATION**

I declare that the thesis entitled “DEVELOPMENT OF NANOPARTICLES LOADED 3D PRINTED MICROCHANNEL FOR FLUORIDE REMOVAL FROM WATER”, has been prepared by me under the guidance of Prof. (Dr.) Jitendra Kumar Pandey, Associate Dean-Research, University of Petroleum and Energy Studies, Dehradun and Assoc. Prof. (Dr.) Amit Kumar Chawla, University of Petroleum and Energy Studies, Dehradun. No part of this thesis has formed the basis for the award of any degree or fellowship previously.



Ravi Kumar Patel

*Doctoral Research Fellow*  
University of Petroleum and Energy Studies  
Dehradun

## CERTIFICATE

I certify that Ravi Kumar Patel has prepared his thesis entitled “DEVELOPMENT OF NANOPARTICLES LOADED 3D PRINTED MICROCHANNEL FOR FLUORIDE REMOVAL FROM WATER”, for the award of Ph.D. degree of the University of Petroleum & Energy Studies, under our guidance. He has carried out the work at the Department of Electrical and Electronics Engineering, University of Petroleum & Energy Studies, Dehradun.



Supervisor

Prof. (Dr.) Jitendra Kumar Pandey  
*Associate Dean-Research*  
University of Petroleum and Energy Studies  
Dehradun



Co-Supervisor

Assoc. Prof. (Dr.) Amit Kumar Chawla  
University of Petroleum and Energy Studies  
Dehradun

## **ABSTRACT**

3D printing or additive manufacturing is a process of making solid three-dimensional objects from a digital file. A 3D printed object is created using additive processes. An object is created in an additive process by laying out successive layers of material until the object is created. One could see each of these layers as a thinly sliced horizontal cross-section of the eventual object. 3D printing is the opposite of subtractive manufacturing, in which a piece of metal or plastic with, for example, a milling machine is cut/hollowed out. 3D printing enables complex shapes to be produced using less material than traditional methods of production. Stereolithography (SLA) is a 3D printing process where an object is created by using an ultraviolet (UV) laser beam to selectively curate a polymer resin layer by layer. The materials used in SLA are thermoset polymers that come in a liquid form and are photosensitive. SLA is the most cost-effective 3D printing technology for better parts with high precision or smooth surface finishing.

In addition to being essential to human health and well-being, exposure to clean drinking water is now recognised as a human right. The facility of safe drinking water is critical and crucial for overall growth achievements, including sufficient nutrition, training, equality between men and women in poorly-developed countries, and especially poverty eradication.

Groundwater supplies are commonly considered to be of good microbiological and chemical consistency, and usually need little to no additional treatment when used as appropriate drinking water supplies. Its use for water supply is therefore related to low possessions, low operational, and maintenance costs.

It is also the most enticing means of drinking water supply is mostly distributed, remote communities of developing countries. Nonetheless, issues will also occur with groundwater chemistry to consider it unhealthy due to increased amounts of certain substances that may influence the user's safety. Therefore, a certain type of treatment is needed to provide clean drinking water through groundwater supplies in these circumstances. Fluoride is among the water quality criteria of significance, the concentration (beyond 1.5 mg / L, the World Health Organisation (WHO) standard value) of which pollutes groundwater supplies in certain areas of the world and does not make it secure for human use, resulting in adverse health consequences. Although optimal fluoride content (0.5-1mg/L) in drinking water is ideal for oral health and healthy bone growth, the harmful effects on human health have been documented for centuries when taken in large amounts (more than 1.5 mg/L). The human health risks of excess fluoride consumption include the occurrence of fluorosis, alterations in DNA structure, reduction of children's IQ, involvement with the functioning of the kidney, and perhaps even death once doses meet quite high concentrations (about 150-250 mg/L).

Owing to the persistent hazard and also the absence of recognized successful fluorosis treatment and other associated health hazards, defluoridation of fluoride polluted groundwater supplies suitable for use is a must, in order to avoid consumption of excessive fluoride as a precautionary measure.

The ultimate research aim was (i) to develop a 3D printed model with the focus to perform a continuous contaminated water treatment. The various researchers have shown the application of 3D printing for microfluidic applications. Adopting this printed model a 3D model is printed here for the

continuous treatment of contaminated water on a small scale. The technique used for printing of the device is stereolithography (SLA). (ii) laboratory synthesis of fluoride adsorbent materials. Various characterization methods were used to analyze the physicochemical properties of the adsorbents, synthesized for removal of fluoride. These involved: X-ray diffraction (XRD), scanning electron microscopy (SEM), energy-dispersive X-ray (EDX) analysis, Fourier transform infrared (FTIR) analysis, and Brunauer-Emmett-Teller (BET) specific surface area analysis and (iii) Defluoridation efficiency of 3D printed model loaded with synthesized adsorbent materials. Lab-scale continuous flow tests were performed to test the efficiencies in the removal of fluoride from the adsorbent loaded 3D printed model.

For the fabrication of a 3D device, the MiiCraft 3D printer was used. Here stereolithography (SLA), the printing process was used for printing the device that belongs to the vat photopolymerization family. In such a method, a structure is formed by selectively curing the polymer resin layer-by-layer using ultraviolet (UV) laser light. The materials used for SLA are photosensitive thermoset polymers that are available in a liquid form. During the fabrication of a 3D device various designs were printed and tested for the applicability as per the requirement. After so many changes and modifications the final printed design was divided into three parts: (i) inlet section, (ii) cylindrical structure, and (iii) outlet section. The cylindrical structure consists of a microchannel having a diameter of 1.5 mm and 2 mm on separate devices. These printed channels were further tested for their continuity and then loaded with the synthesized adsorbent at the second stage.



After the finalization of the 3D printed model, adsorbent preparation was carried out. Hematite, titanium dioxide and activated carbon adsorbent were synthesized at lab scale to perform the fluoride removal study. The characterization results of adsorbents shown that the adsorbents required were synthesized successfully. These adsorbents were then used for the defluoridation study.

In the final stage after the successful printing of the 3D model and synthesis of adsorbent required to study the fluoride removal efficiency was performed. The synthesized adsorbent was loaded in the 3D printed microchannel by suspending adsorbent in the double distilled water to form a thick paste solution. The formed paste was poured in microchannels followed by drying in the oven at 40°C for 2 hrs and this process was repeated 5-7 times. The adsorption capacity of 2.47 mg/g for the hematite adsorbent 4.59 mg/g for titanium dioxide and 14.45 mg/g for activated carbon adsorbent was observed respectively for the fluoride removal process using the proposed system. This adsorption capacity was obtained for a lower fluoride concentration of 3 mg/L. The device used to obtain this adsorption capacity was having a 2 mm diameter channel and adsorbent dosage of 4 g for hematite and titanium dioxide whereas 1 g for activated carbon. The leach test was also performed for the detection of heavy metals in the treated water. It was found that there was no occurrence of leaching during the treatment process. For the real time application developed system, the spiraled microchannel having a 2 mm pore size was loaded with 1 g activated carbon at fluoride concentration of 5.3 mg/L. The adsorption capacity observed for this setup was around 18.39 mg/g. The estimated

value for producing per litre of purified water was 12.9 INR using the laboratory based single device. The value was calculated for 5 regeneration-reuse recycles.

Finally a 3D printed model setup was established which might be an alternative approach in accordance with the available traditional column. Here in reference to the traditional single channel column the device designed consists of the multiple numbers of channels that support the proper holding of the loaded adsorbent and also the active sites of loaded adsorbent for effective adsorption process. The proposed model may be used for small scale applications. Since the gravitational flow or overhead pressure was taken into account to resemble the real conditions where external forces may not be applied during the implementation of a 3D printed system. This is the first attempt to develop such type of devices that have shown a clear potential for removal of fluoride from the spiked water and bench scale prototype described here is a real device tested in our laboratory.

## **ACKNOWLEDGEMENT**

I would first like to thank my Ph.D. supervisors, Dr. Jitendra Kumar Pandey and Dr. Amit Kumar Chawla, for encouraging me to take this research problem on ‘Development Of Nanoparticles Loaded 3D Printed Microchannel For Fluoride Removal From Water’. My supervisors has been a source of inspiration and motivation to me throughout this work. Without them, this work would never have been completed.

I am thankful to Chancellor Dr. S. J. Chopra, Vice-Chancellor Dr. Sunil Rai, CEO Mr. Sharad Mehra, and Dean SOE Dr. Kamal Bansal. I would like to mention a special thanks to team R&D UPES for providing constant guidance and support.

I would like to thank Ms. Rakhi Ruhai, Mr. Sony Sandeep Farmer, and other staff members for their help and numerous occasions.

I am also grateful to the lab staff and their support at our Institute (UPES, Dehradun) and at the Indian Institute of Technology, Roorkee (IIT-R) for my research and experimental analysis.

I would like to thank my parents for their constant support at every stage of my life. Completing this degree would never be possible without their continuous encouragement. Finally, I’m thankful to all of my dear colleagues for their continuous help and support in this long journey of Ph.D. course.

## TABLE OF CONTENTS

DECLARATION .....	i
CERTIFICATE .....	ii
ABSTRACT.....	iii
ACKNOWLEDGEMENT .....	viii
TABLE OF CONTENTS.....	ix
LIST OF SYMBOLS .....	xiii
LIST OF ABBREVIATIONS.....	xiv
LIST OF FIGURES .....	xvi
LIST OF TABLES .....	xx
CHAPTER 1 INTRODUCTION .....	1
1.1 General.....	1
1.2 Water Scenario.....	1
1.3 Global Scenario of Fluoride Concentration .....	3
1.3.1 World Scenario .....	3
1.3.2 Indian Scenario .....	4
1.4 Additive Manufacturing.....	7
1.5 Problem Statement.....	9
1.6 Research Contribution .....	9
1.7 Outline of the Thesis.....	9
1.8 References.....	10
CHAPTER 2 LITERATURE REVIEW .....	16
2.1 Introduction.....	16
2.2 Fluoride Removal Techniques .....	16
2.2.1 Ion Exchange Process .....	17
2.2.2 Coagulation and Electrocoagulation .....	18
2.2.3 Membrane .....	20
2.2.4 Adsorption.....	21
2.3 Nanoadsorbents for Fluoride Removal .....	24
2.3.1 Carbon Nanotubes.....	24
2.3.2 Metal Based .....	25
2.3.3 Miscellaneous .....	29
2.3.3.1 Calcium Based.....	29

2.3.3.2 Natural Materials .....	30
2.3.3.3 Agricultural Residues .....	30
2.3.3.4 Industrial Residues .....	31
2.3.3.5 Building Materials .....	31
2.4 3D Printing.....	37
2.5 3D Printed Material Applications .....	40
2.5.1 Spacer.....	40
2.5.2 Membrane .....	44
2.5.3 Adsorbent.....	49
2.6 Conclusion .....	51
2.7 References.....	52
<b>CHAPTER 3 MATERIALS AND METHODS .....</b>	<b>68</b>
3.1 Materials .....	68
3.2 Instruments.....	69
3.2.1 X-ray Diffraction .....	69
3.2.2 Scanning Electron Microscope .....	70
3.2.3 Brunauer Emmett and Teller.....	71
3.2.4 Fourier Transform Infrared Spectroscopy .....	72
3.2.5 Ion Selective Electrode Meter.....	73
3.2.6 Inductively Coupled Plasma-Optical Emission Spectrometry....	74
3.2.7 3D Printer.....	75
3.2.8 Thermal Mechanical Analyzer.....	76
3.3 Experimental Plan.....	77
3.4 Conclusion .....	77
<b>CHAPTER 4 FABRICATION OF MICROCHANNELS BY 3D</b>	
<b>PRINTING.....</b>	<b>78</b>
4.1 General.....	78
4.2 3D Printing of Microchannels.....	79
4.3 Solid Modelling .....	80
4.4 Device Design.....	80
4.4.1 Cuboid Structure .....	81
4.4.2 Cylindrical Structure .....	84
4.5 TMA analyzer .....	91

4.6 Conclusion .....	92
4.7 References.....	92
CHAPTER 5 SYNTHESIS AND CHARACTERIZATION OF	
ADSORBENT.....	95
5.1 Defluoridation Adsorbents.....	95
5.1.1 Hematite.....	97
5.1.2 Titanium Dioxide .....	98
5.1.3 Activated Carbon .....	98
5.2 Synthesis of Adsorbents .....	99
5.2.1 Hematite Adsorbent .....	99
5.2.2 Titanium Dioxide Adsorbent .....	100
5.2.3 Activated Carbon Adsorbent.....	101
5.3 Characterization of Adsorbents .....	102
5.3.1 Hematite.....	102
5.3.2 Titanium Dioxide .....	106
5.3.3 Activated Carbon .....	110
5.4 Conclusion .....	113
5.5 References.....	113
CHAPTER 6 DEFLOURIDATION MODEL EFFICIENCY .....	
6.1 Defluoridation Model .....	115
6.2 Stock Solution and Adsorption Study.....	116
6.3 Leach Test.....	117
6.4 Regeneration of Adsorbents.....	118
6.5 Hematite Loaded Model .....	118
6.5.1 Leach Test of Hematite.....	124
6.5.2 Regeneration of Hematite .....	124
6.6 Titanium Dioxide Loaded Model .....	125
6.6.1 Leach Test of Titanium Dioxide.....	128
6.6.2 Regeneration of Titanium Dioxide .....	128
6.7 Activated Carbon Loaded Model.....	129
6.7.1 Regeneration of Activated Carbon.....	131
6.8 Conclusion .....	131
6.9 References.....	131

CHAPTER 7 DEVELOPMENT OF REAL TIME APPLICATION SYSTEM.....	134
7.1 General.....	134
7.2 System Development .....	135
7.3 Fluoride Removal Efficiency .....	138
7.4 Water Quality Quantification.....	139
7.5 Regeneration of Loaded Adsorbent .....	139
7.6 Cost Analysis .....	140
7.7 Conclusion .....	140
7.8 References.....	141
CHAPTER 8 CONCLUSION AND RECOMMENDATION .....	142
8.1 Conclusion .....	142
8.2 Recommendations.....	143

## LIST OF SYMBOLS

$\lambda$  : Wavelength of X-ray

$\theta$  : Angle between incident ray and scattering plane

$T_g$  : glass-transition temperature

$\mu$  : electronic chemical potential

$\eta$  : chemical hardness

$E$  : electronic energy of the ground state

$V$  : potential

$I$  : ionization energy

$A$  : electron affinity

$\chi$  : absolute electronegativity

$\mu_A^0$  and  $\mu_B^0$  : neutral state chemical potentials

$\Delta N$  : number of electrons transferred

At % : atomic percentage

Wt % : weight percentage

$C_o$  : initial concentration of fluoride

$C_e$  : equilibrium concentration of fluoride

$q_{t_e}$  : quantity of adsorbed fluoride at service time

$m$  : adsorbent dosage

$Q_v$  : volumetric flow rate of effluent

$t_e$  : service time in the exhausted column

$C_t$  : concentration of fluoride observed at different interval of time



## LIST OF ABBREVIATIONS

AM.....	ADDITIVE MANUFACTURING
3DP.....	3-DIMENSIONAL PRINTING
RP.....	RAPID PROTOTYPING
2D.....	2-DIMENSIONAL
3D.....	3-DIMENSIONAL
SLA.....	STEREOLITHOGRAPHY
CAD.....	COMPUTER AIDED DESIGN
FDM.....	FUSED DEPOSITION MODELLING
FFF.....	FUSED FILAMENT FABRICATION
LOM.....	LAMINATED OBJECT MANUFACTURING
SDL.....	SELECTIVE DEPOSITION LAMINATION
SLS.....	SELECTIVE LASER SINTERING
DMLS.....	DIRECT METAL LASER SINTERING
SLM.....	SELECTIVE LASER MELTING
EBM.....	ELECTRON BEAM MELTING
EBM-I.....	ELECTRON BEAM MELTING-I
EBM-II.....	ELECTRON BEAM MELTING-II
.STL.....	STANDARD TESSELLATION LANGUAGE
UV.....	ULTRAVIOLET
BIM.....	BUILDING INFORMATION MODEL
WHO.....	WORLD HEALTH ORGANIZATION
IEP.....	ION EXCHANGE PROCESS
SWM.....	SPIRAL WOUND MEMBRANE
TPMS.....	TRIPLY PERIODIC MINIMAL SURFACE
DLP.....	DIGITAL LIGHT PROCESSING
RO.....	REVERSE OSMOSIS
BWRO.....	BRACKISH WATER REVERSE OSMOSIS
MFS.....	MEMBRANE FOULING SIMULATOR
NF.....	NANOFILTRATION
UF.....	ULTRAFILTRATION
MF.....	MICROFILTRATION
ABS.....	ACRYLONITRILE BUTADIENE STYRENE

PES..... POLYETHERSULFONE  
 NIPS ..... NON-SOLVENT INDUCED PHASE SEPARATION  
 PA ..... POLYAMIDE  
 MDC ..... MICROBIAL DESALINATION CELL  
 EDTA..... ETHYLENEDIAMINETETRAACTIC ACID  
 TPU..... THERMOMOPLASTIC POLYURETHANE  
 4D.....4-DIMENSIONAL  
 CNT..... CARBON NANOTUBE  
 HA-MWCNT ..... HYDROXYAPATITE-MULTI-WALLED CARBON  
 NANOTUBE  
 LDH ..... LAYERED DOUBLE HYDROXIDES  
 MA ..... MESOPOROUS ALUMINA  
 AA..... ACTIVATED ALUMINA  
 XRD ..... X-RAY DIFFRACTION  
 FWHM ..... FULL WIDTH AT HALF MAXIMUM  
 SEM ..... SCANNING ELECTRON MICROSCOPE  
 FESEM.....FIELD EMISSION SCANNING ELECTRON MICROSCOPE  
 EDAX ..... ENERGY DISPERSIVE X-RAY  
 BET..... BRUNAUER-EMMETT-TELLER  
 FTIR..... FOURIER-TRANSFORM INFRARED  
 ISE..... ION SELECTIVE ELECTRODE  
 ORP..... OXIDATION-REDUCTION POTENTIAL  
 ICP-OES ..... INDUCTIVELY COUPLED PLASMA - OPTICAL EMISSION  
 SPECTROMETRY  
 TMA..... THERMAL MECHANICAL ANALYZER  
 HSAB..... HARD-SOFT ACID-BASES  
 EDS ..... ENERGY-DISPERSIVE X-RAY SPECTROSCOPY  
 IUPAC..... INTERNAL UNION OF PURE AND APPLIED CHEMISTRY  
 HDPE ..... HIGH-DENSITY POLYETHYLENE  
 TISAB ..... TOTAL IONIC STRENGTH ADJUSTMENT BUFFER

## LIST OF FIGURES

Figure 1.1 Fluoride concentration and its health effect .....	2
Figure 1.2 Skeletal fluorosis, India .....	3
Figure 1.3 Countries affected with high fluoride concentration > 1.5 in water.....	4
Figure 1.4 (a) State wise fluoride distribution in Indian groundwater and (b) Fluoride affected districts in India(in percentage) .....	6
Figure 1.5 3D printing process.....	8
Figure 2.1 IEP shows anion exchange using strong base anion exchange using chloride form.....	17
Figure 2.2 Schematic of a coagulation process.....	19
Figure 2.3 Membrane technology .....	20
Figure 2.4 Flow chart of the adsorption phenomenon .....	22
Figure 2.5 Suggested mechanism for the adsorption of F on $\gamma$ -Fe <sub>2</sub> O <sub>3</sub> .....	28
Figure 2.6 Improved configuration of Fe <sub>2</sub> (OH) <sub>6</sub> (H <sub>2</sub> O) <sub>4</sub> , Fe <sub>2</sub> (OH) <sub>5</sub> (H <sub>2</sub> O) <sub>4</sub> F and Fe <sub>2</sub> (OH) <sub>4</sub> (H <sub>2</sub> O) <sub>4</sub> F <sub>2</sub> clusters (Blue colour Fe, Red colour O, Off white colour H and Off green colour F).....	28
Figure 2.7 Types of 3D printing technologies .....	37
Figure 2.8 3D printing technology properties.....	38
Figure 2.9 Representation of spiral wound membrane module component with spacer and the dimensions for the parts of a membrane unit along with existing resolution restrictions of 3D printing.....	41
Figure 2.10 Existing constraint in resolution of 3D printing technology when applied for membrane research .....	45
Figure 2.11 Composite membrane schematics: 3D printing of wavy design support layer was performed while the selective layer at the top was first casted by the non-solvent induced phase separation (NIPS) and then the casted membrane is attached by vacuum filtration to the 3D-printed support .....	46
Figure 2.12 Top shows flat and patterned membranes along with pattern schematic and Bottom shows example of patterned membranes.....	47
Figure 2.13 (a) Adsorption capacity comparison of Cu (II) for 3D printed chitosan filters of various structures (T= 25°C and pH 5.5) (b) 3D printed hydrogels for heavy metal removal .....	50

Figure 3.1 Bruker D8 Advance Eco X-ray diffractometer .....	69
Figure 3.2 SEM (FEI Quanta 200F) .....	71
Figure 3.3 Accelerated Surface Area and Porosimetry System, Micromeritics, ASAP 2020 .....	72
Figure 3.4 PerkinElmer Frontier FTIR .....	73
Figure 3.5 Thermo Scientific Orion Dual Star pH/ISE.....	74
Figure 3.6 PlasmaQuant PQ9000 ICP-OES.....	75
Figure 3.7 (a) MiiCraft printer (b) Printing process .....	75
Figure 3.8 Thermal Mechanical Analyzer .....	76
Figure 4.1 Additive Manufacturing Process .....	79
Figure 4.2 Stereolithography printing process.....	80
Figure 4.3 (a) Drawing and CAD model (isometric view) (b) 3D printed device .....	81
Figure 4.4 Drawing of cube structure .....	82
Figure 4.5 CAD models of the cuboid design (a) 2 mm and (b) 1.5 mm pore size .....	83
Figure 4.6 3D printed (a) 2 mm and (b) 1.5 mm pore size model .....	83
Figure 4.7 Tradition column prototype.....	84
Figure 4.8 Inlet and outlet section.....	85
Figure 4.9 Cylindrical structure of the device .....	85
Figure 4.10 Final assembled CAD model.....	85
Figure 4.11 (a) Drawing and (b) CAD model of cylindrical design .....	86
Figure 4.12 (a) Drawing and (b) CAD model of a channel having 1.5 mm pore size .....	86
Figure 4.13 Printing errors.....	87
Figure 4.14 Truncated cone (a) Elongation of cone (b) Splitting edge .....	87
Figure 4.15 Cylindrical structure deformation.....	87
Figure 4.16 Printing error parameters .....	88
Figure 4.17 (a) Inlet and outlet section (b) Cylindrical structure .....	88
Figure 4.18 3D printed parts of the filter .....	89
Figure 4.19 Drawing of spiraled microchannels.....	90
Figure 4.20 Cross-sectional CAD view showing the internal pattern of channel .....	90

Figure 4.21 Stress and strain analysis response .....	91
Figure 5.1 Crystal structure of hematite .....	97
Figure 5.2 Lattice of anatase form of titanium dioxide .....	98
Figure 5.3 Hematite synthesis procedure.....	99
Figure 5.4 Titanium dioxide synthesis process.....	100
Figure 5.5 Activated carbon synthesis process using jute fiber.....	101
Figure 5.6 X-ray diffraction of hematite.....	102
Figure 5.7 (a), (b), (c) and (d) Scanning electron microscope images of $\alpha$ - $\text{Fe}_2\text{O}_3$ nanoparticles.....	103
Figure 5.8 EDS spectrum of $\alpha$ - $\text{Fe}_2\text{O}_3$ nanoparticles (a) showing the area considered for EDS while (b) showing the EDS pattern .....	103
Figure 5.9 $\text{N}_2$ adsorption /desorption isotherm on $\alpha$ - $\text{Fe}_2\text{O}_3$ nanoparticles.....	104
Figure 5.10 FTIR of hematite adsorbent.....	105
Figure 5.11 XRD pattern of synthesized anatase $\text{TiO}_2$ nanopowder .....	106
Figure 5.12 (a), (b), (c) and (d) Scanning electron microscope images of $\text{TiO}_2$ nanopowder.....	107
Figure 5.13 EDS spectrum of $\text{TiO}_2$ nanoparticles (a) showing the area considered for EDS while (b) showing the EDS pattern .....	107
Figure 5.14 $\text{N}_2$ adsorption/desorption isotherm of synthesized $\text{TiO}_2$ nanopowder .....	108
Figure 5.15 FTIR spectrum of $\text{TiO}_2$ nanoparticle.....	109
Figure 5.16 XRD profile of activated carbon .....	110
Figure 5.17 (a) and (b) SEM photographs of activated carbons .....	110
Figure 5.18 $\text{N}_2$ Adsorption/desorption isotherms of activated carbon.....	111
Figure 5.19 FTIR spectrum of activated carbon .....	112
Figure 6.1 Final 3D printed device .....	115
Figure 6.2 Glass wool for packing.....	116
Figure 6.3 Sampling process.....	118
Figure 6.4 Process for hematite adsorbent loading of 3D printed channel....	119
Figure 6.5 Hematite loaded parts of the model.....	119
Figure 6.6 (a) Assembled parts of device (b) Final assembly of the device with Hematite adsorbent .....	119
Figure 6.7 Experimental set up for hematite loaded device.....	120

Figure 6.8 Removal efficiency results of the process flow setup for Hematite adsorbent (a) 3g of adsorbent dosage loaded in 1.5 mm pore size channels (b) 4g of adsorbent dosage loaded in 2 mm pore size channels was tested for the 3, 6 and 10 mg/L of fluoride concentration .....	121
Figure 6.9 XRD analysis before and after fluoride removal.....	123
Figure 6.10 FTIR analysis before and after fluoride removal .....	123
Figure 6.11 Titanium dioxide adsorbent loading procedure for 3D printed channel .....	125
Figure 6.12 Titanium dioxide loaded parts of the model.....	126
Figure 6.13 (a) Assembled parts of the device (b) Final assembly of the device with Titanium dioxide adsorbent .....	126
Figure 6.14 Removal efficiency results for 4 g adsorbent loaded on 2 mm diameter channel for Titanium dioxide adsorbent .....	127
Figure 6.15 Removal efficiency results for 1 g adsorbent loaded on 2 mm diameter channel for activated carbon adsorbent.....	129
Figure 7.1 Fluoride concentration in groundwater, Madhya Pradesh, India .....	134
Figure 7.2 Highest range of fluoride in each district of M.P .....	135
Figure 7.3 Developed system for groundwater analysis .....	136
Figure 7.4 Primary elements, secondary elements, major cations and anions in groundwater .....	138
Figure 7.5 Spiraled microchannel 3D model .....	138
Figure 7.6 Fluoride removal efficiency of spiraled microchannel.....	139

## LIST OF TABLES

Table 2.1 A comparative analyses of the removal technologies of toxic ions in water.....	23
Table 2.2 Adsorption capacity of various adsorbents under defined parameters for the removal of fluoride.....	32
Table 2.3 Materials, pros, and cons of 3D printing techniques .....	38
Table 3.1 Reagents used for adsorbent synthesis.....	68
Table 3.2 Reagents used during fluoride removal study.....	69
Table 3.3 Major specification of ISE meter.....	74
Table 3.4 Composition/Information on ingredients for 3D printer.....	76
Table 5.1 Chemical composition of Fe <sub>2</sub> O <sub>3</sub> nanoparticles in terms of atomic percentage (At %) and weight percentage (Wt %) from energy dispersive spectra (EDS) measurement.....	104
Table 5.2 Chemical composition of TiO <sub>2</sub> nanoparticles in terms of atomic percentage (At %) and weight percentage (Wt %) from energy dispersive spectra (EDS) measurement.....	108
Table 6.1 Typical ICP-OES operating conditions. ....	117
Table 6.2 Comparison of adsorption capacity with Hematite adsorbent. ....	124
Table 6.3 Comparison of adsorption capacity with Titanium dioxide nanopowder.....	128
Table 6.4 Comparison of adsorption capacity with activated carbon adsorbent.....	130
Table 7.1 Cost calculation for laboratory prototype .....	140

# CHAPTER 1

## INTRODUCTION

*This chapter discusses an overview of natural water resources, the discharge of fluoride impact water from different industries into the local environment, along with additive manufacturing and its day-to-day application. At the end of this chapter the purpose and structure of the thesis research are outlined.*

### 1.1 GENERAL

Nowadays, clean drinking water has become a commodity but unfortunately, not available in every region of the world. Numerous people living in underdeveloped areas are deprived of safe drinking water and witness several lethal diseases that cost their lives. Groundwater supply in such areas is generally without any purification, cleaning, and treatment that may have harmful pollutants. Water gets contaminated due to natural disasters or anthropogenic happenings of human beings. The demand for our water systems increases as water scarcity increases and population increases. Technological development such as additive manufacturing helps to develop cutting-edge technology that might improve our world and change vulnerable communities.

### 1.2 WATER SCENARIO

Fluoride is considered as major groundwater pollutant due to the natural presence of various forms of fluoride (Sellaite ( $\text{MgF}_2$ ), Fluorapatite ( $3\text{Ca}_3(\text{PO}_4)_2 \cdot \text{CaF}_2$ ), Fluorspar ( $\text{CaF}_2$ ), and Cryolite ( $\text{Na}_3\text{AlF}_6$ )). These forms of fluoride are due to the interaction of water rocks, recharge of groundwater and various anthropogenic activities (Ayoob & Gupta, 2006; J. K. Fawell & Bailey, 2006; Ghosh, Mukherjee, Ghosh, & Saha, 2013; Suthar et al., 2008). Fluoride is one of the toxic ion present in the potable water all over the world which is affecting many people and as per the report, it is observed that



approximately 7 million people in India and approximately 200 million people from 25 nations are affected with severe health risks due to high fluoride concentrations in groundwater (Lapworth, Baran, Stuart, & Ward, 2012). Fluoride in drinking water can have both the effects on human health, either beneficial or detrimental (Biswas, Bandhoyapadhyay, & Ghosh, 2007; Edition, 2011; J. Fawell, Bailey, Chilton, Dahi, & Magara, 2006; Madhnure, Sirsikar, Tiwari, Ranjan, & Malpe, 2007). The prescribed amount is mandatory for good health particularly in tooth development, dental health, and bone development. As per WHO guidelines and recommendations the optimal concentration of fluoride in warm and cold areas is 1 mg/L and 1.2 mg/L, respectively (Organization, 1996; WHO, 2011). The differences are due to the fact that people in warm areas perspire more, therefore, drink more water. The Indian standard for drinking water recommends maximum permissible and tolerance limit of fluoride as 1 mg/L and 1.5 mg/L, respectively (Standards), 2012). The excess of fluoride above permissible and tolerance limit, affects the human health (Fig 1.1) by causing dental fluorosis (1.0-3.0 mg/L) (Miretzky & Cirelli, 2011), rigid bones/weak bones (3.0-4.0 mg/L) (Miretzky & Cirelli, 2011), defects in knee, hip bones and paralysis (4.0-6.0 mg/L) (Alarcon-Herrera, MartIn-Dominguez, Trejo-Vázquez, & Rodriguez-Dozal, 2001; Cauley, Buhari, Murphy, & Riley, 1995; Li et al., 2001; Maheshwari, 2006).

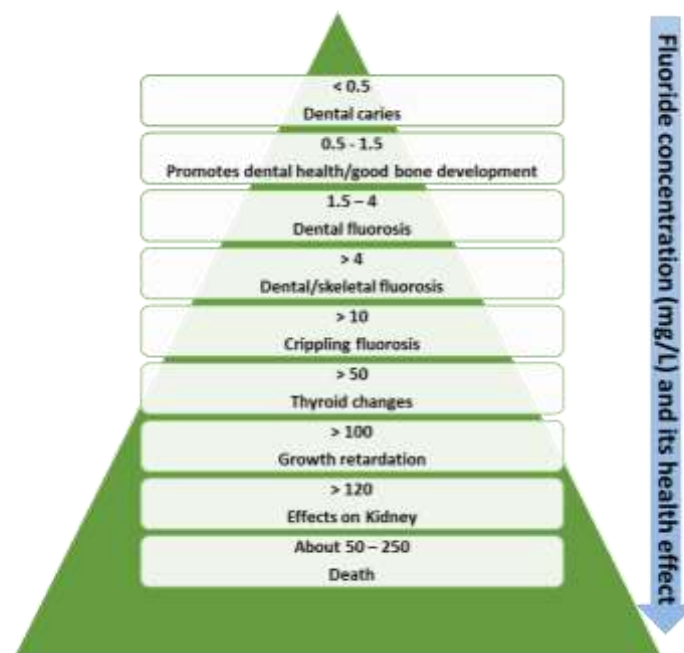


**Fig 1.1** Fluoride concentration and its health effect

Fig 1.2 shows skeletal fluorosis cases from India. Apart from fluorosis, the excessive fluoride consumption causes cancer, thyroid disorder, urinary tract and allergic manifestation, brain damage, Alzheimer's syndrome, neurological and muscular problems (Chinoy, 1991; Standard, 1991).



**Fig 1.2** Skeletal fluorosis, India (Source: UNICEF, 2004 and UNICEF 2001)

### **1.3 GLOBAL SCENARIO OF FLUORIDE CONCENTRATION**

#### **1.3.1 WORLD SCENARIO**

A major challenge is the issue of the harmful concentration of fluoride in drinking water. Endemic fluorosis affects both developed and developing nations (Ayoob & Gupta, 2006; Bell & Ludwig, 1970; Smet, 1992). The concentration of elevated fluoride in groundwater is based on the geology of various parts of the world; it has a cumulative accumulation of 85 million tons in the earth's crust mostly in mid-latitude regions (Pokhraj Sahu et al., 2018; Teotia & Teotia, 1994). High fluoride-containing groundwater exists in large parts of Africa, China, the Middle East, and southern Asia (India and Sri Lanka). WHO confirmed that large fluoride belts spread across Malawi from Eritrea, Syria to Turkey, Afghanistan, India, and China. Similarly other

fluoride belts are also found in America, Kenya, Iraq, Japan, and Iran (Pokhraj Sahu et al., 2018). Strong fluorine region in Northern China, in the Huaibei Plain (Hu, Xia, Dong, & Liu, 2017). The magnitude and severity of fluoride have varied with references to geographic environmental sitting as shown in Fig 1.3.

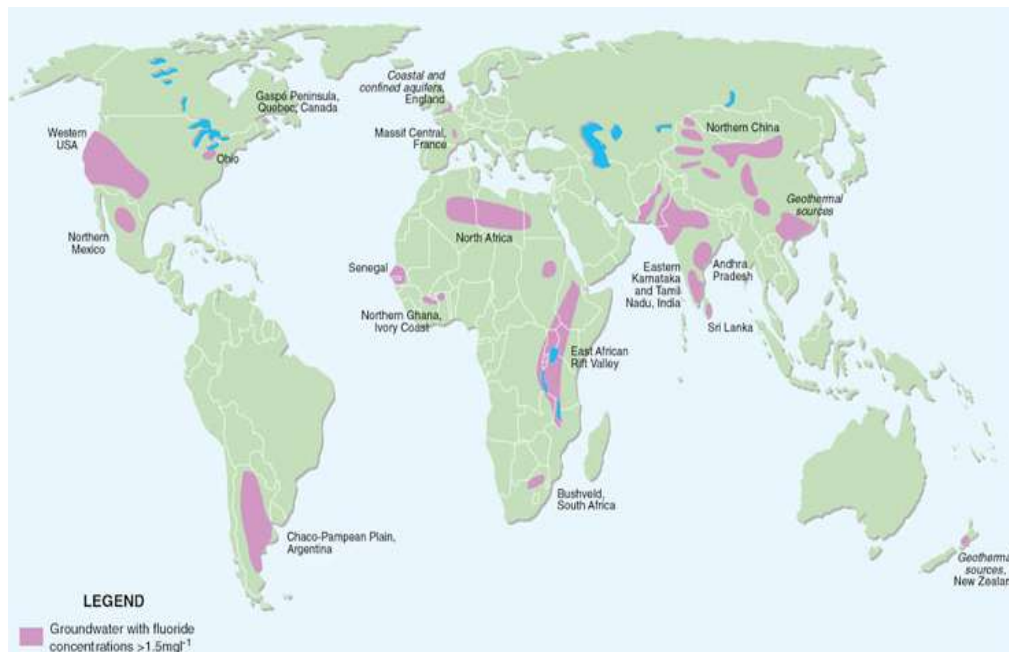


**Fig 1.3** Countries affected with high fluoride concentration > 1.5 mg/ L in water (Smedley)

The indication of fluorosis is observed on the resident of those areas where the concentration of fluoride was more than 1.5 mg/L. WHO (2011) (Edition, 2011) has recommended 1.5 mg/L of fluoride in drinking water, although it is not adopted throughout the country as it varies based on the quantity of potable water taken, climate, and diet (Dharmshaktu, 2013).

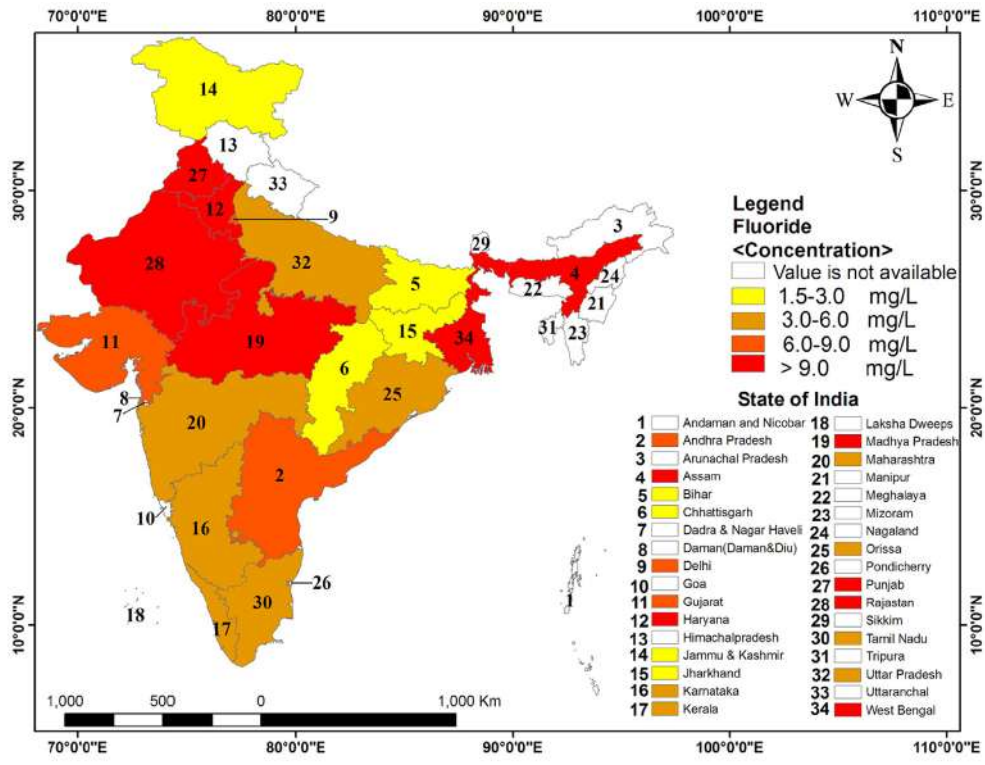
### 1.3.2 INDIAN SCENARIO

India is one of the countries most impacted by groundwater contamination by fluoride. Fluoride is greater than the permissible level in groundwater and is a major health issue. Up to 12 million of the 85 million tons of fluoride

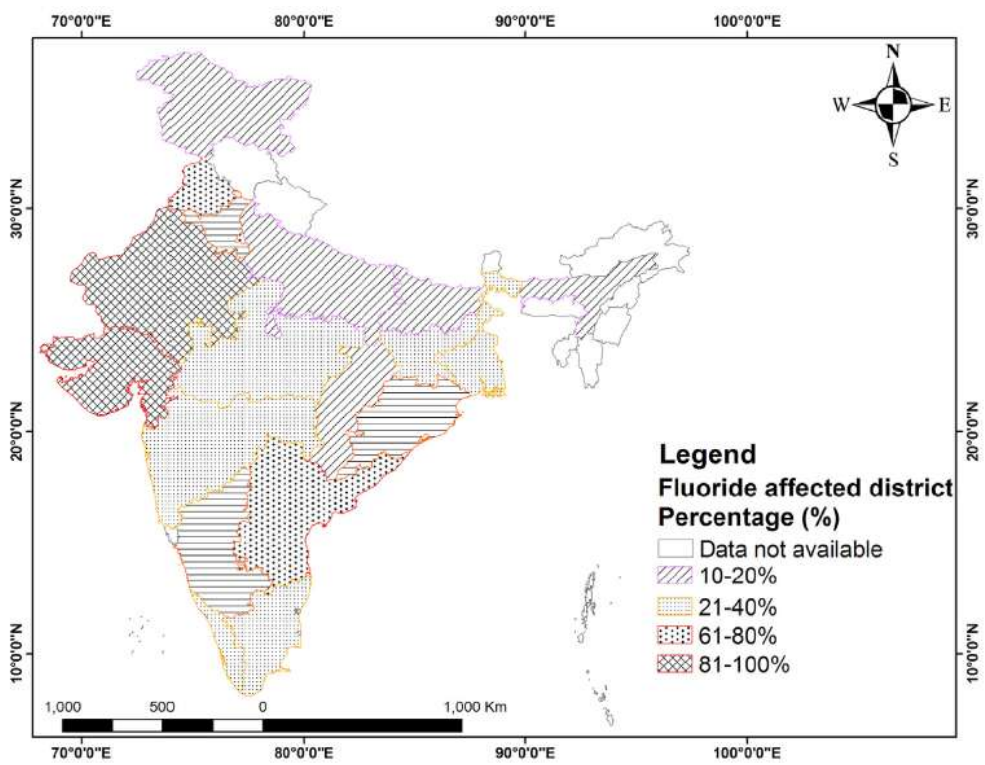
concentrations on the earth's crust are located in India, which could be the reason for high fluoride in groundwater. Arsenic and fluoride are regarded as the two major pollutants in terms of the number of people affected and the area of distribution (Paulami Sahu, 2019).

Fluoride contamination has indeed been recognized as among the most serious problems of natural groundwater quality impacting India's arid and semi-arid areas. High levels of fluoride have been identified for instance in Andhra Pradesh's Nalgonda district. Earlier, several areas of the country were found with elevated fluoride concentrations, among which Andhra Pradesh, Rajasthan, Haryana, Punjab, Gujarat, and Assam were the severely affected states (Kumar, Das, Das, Goswami, & Singh, 2016).

Groundwater in semi-arid areas of Gujarat is considered to have fluoride concentration above the World Health Organization's drinking water limit (1.5 mg/L) (Raza, Farooqi, Niazi, & Ahmad, 2016). Groundwater fluoride concentrations below 5 mg/L were recorded in the Indian states of Bihar, Chhattisgarh, Jammu and Kashmir, Jharkhand, Karnataka, Maharashtra, Tamil Nadu, and Uttar Pradesh. Concentrations of fluoride between 5 and 10 mg/L were recorded in Andhra Pradesh, Bihar, Gujarat, Kerala, Orissa, and West Bengal. In areas of Punjab, Assam and Haryana, fluoride concentrations of approximately 10–20 mg/L were recorded. It has been confirmed that the average fluoride concentration exceeded 20 mg/L in many areas of Rajasthan (CGWB, 2014). The maximum regions affected by fluoride were recorded to be Rajasthan and Gujarat (80–100 per cent) preceded by Andhra Pradesh and Punjab (60–80 per cent). Approximately 21– 40 per cent of affected regions by fluoride contamination is in Madhya Pradesh, Maharashtra, Kerala, Tamil Nadu, Jharkhand, West Bengal, and Sikkim. The fluoride enrichment is limited in some parts of India and is present in very few areas of Haryana, Jammu and Kashmir, Karnataka, Uttar Pradesh, and Assam (10–20 per cent).



(a)



(b)

**Fig 1.4** (a) State wise fluoride distribution in Indian groundwater and (b) Fluoride affected districts in India (in percentage) (CGWB, 2010)

About 70 per cent of the districts of Andhra Pradesh are impacted by groundwater contamination from fluoride. In Delhi, fluoride contamination impacts primarily the Northwest and West Parts. Fluoride contamination affects approximately 92 per cent of Gujarat districts and has recorded up to 7.5 mg/L. 97 per cent of districts (mainly arid regions) in Rajasthan are severely affected and have reported up to 38 mg/L fluoride level. In West Bengal, fluoride contamination region is occupied by 37 per cent of districts. In Punjab, concentrations of fluoride in Sangrur and Ghorenab regions were found up to 11.30 mg/L, while approximately 77 per cent of the other districts are at high risk of contamination of fluoride. 60 per cent of the districts in Orissa are in strong fluoride quality regions (CGWB, 2010). Fig 1.4 (a) and (b) shows the fluoride concentration scenario in various parts of India.

There are various technologies that are existing for the removal of fluoride from water as discussed in Chapter 2. However it is evident from Chapter 2, there is a scope for the application of additive manufacturing technology for developing a fluoride removal device. So, in the following subsection basics of the additive manufacturing technology have been discussed.

#### **1.4 ADDITIVE MANUFACTURING**

Additive manufacturing (AM), categorized as 3-dimensional printing (3DP) and rapid prototyping (RP). The model was created bottom-up, by the deposition of one layer at a time (Hull, 1986). It has the ability of creating any complex shape or model with various available materials and also with varying scales (Rengier et al., 2010). Initially, the inkjet printing technique was used for sequentially depositing 2D material layer-by-layer on a powder bed for forming a 3D structure (Russell et al., 1999). Later on 3D printing has gained popularity depending upon its working and end product due to which various other printing techniques were evolved such as stereolithography (SLA) (Cohen, Laviv, Berman, Nashef, & Abu-Tair, 2009), sintering (Deckard, 1989), and extrusion-based process (Crump, 1992). AM begins with a computer-aided design (CAD) drawing of the 3D model to be printed. This

design is sliced into layers and printed layer-by-layer, forming a 3D structure (Peltola, Melchels, Grijpma, & Kellomäki, 2008) (Fig 1.5).

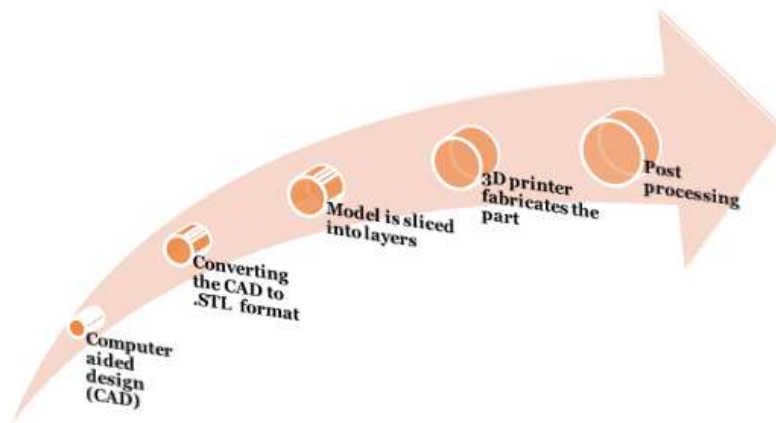


**Fig 1.5** 3D printing process

Materials being used for printing are metals (DebRoy et al., 2018), ceramic (Ianko, Panov, Sushchyns'ky, Pylypenko, & Dmytrenko, 2018), graphene-based materials (Zhu et al., 2015), thermoplastics (Caminero, Chacón, García-Moreno, & Rodríguez, 2018), polymers (Stansbury & Idacavage, 2016) and possible variations in hybrid, composite or functionally graded materials (FGMs) form (Lee, An, & Chua, 2017; Tofail et al., 2018). AM has covered a wide range of areas for its application like manufacturing and engineering (Kim et al., 2014; Tseng, Murray, Kim, & Di Carlo, 2014), art (Séquin, 2005), medicine (Murphy & Atala, 2014; Rengier et al., 2010) and education (Gonzalez-Gomez, Valero-Gomez, Prieto-Moreno, & Abderrahim, 2012; Kostakis, Niaros, & Giotitsas, 2015). Recently, the use of AM has extended its application in the domain of water treatment (Badalov & Arnusch, 2016; Femmer, Kuehne, Torres-Rendon, Walther, & Wessling, 2015; Femmer, Kuehne, & Wessling, 2014).

3D printing technology is starting a water revolution when we need it most. It has the ability to cost-efficient disposal of polluted water in wastewater sectors. Breakthrough 3D printing technologies open the possibility for water infrastructure transformation.

## **1.5 PROBLEM STATEMENT**

Fluoride presence in water shows both beneficial and detrimental health effects depending upon its concentration presence as per WHO guidelines. To maintain the required fluoride concentration in water various fluoride removal technologies have been used such as ion exchange, coagulation and electrocoagulation, membrane, and adsorption. These techniques were found to be expensive or ineffective or possibility of introducing undesirable chemical components in water during the purification procedure. These shortcomings are largely addressed if the 3D printing technology is integrated with the available adsorption technology for the removal of fluoride from water. In recent years various adsorbents have shown their better potential for the removal of anionic constituents from water. The better adsorption capacity of these adsorbents was due to the high surface area available for the removal process. These adsorbents when integrated with 3D printing technology develop a system that is durable, cost-effective, ease to operate, robust, and needs very less operational usage information.

## **1.6 RESEARCH CONTRIBUTION**

- The major contribution of this thesis is the development of 3D printed microchannel of polymeric resin by Stereolithography technique, loaded with synthesized nanoparticles
- The other contribution of the thesis is to study its retention time, the efficiency of fluoride removal, and the durability of 3D printed microchannels loaded with nanoparticles with respect to the amount of contamination.

## **1.7 OUTLINE OF THE THESIS**

This thesis is made up of 8 chapters:

- After this introductory chapter, **Chapter 2** concludes the literature review about the application of 3D printing in the field water treatment and also brief literature on the various adsorbents that are reported by the researchers for the removal of fluoride from water.



- **Chapter 3** presents materials and methods. The chapter discusses the materials used and the applicable methods for the preparation and characterization of nanoadsorbents and also the preparation of spiked fluoride and its quantification before and after treatment.
- **Chapter 4** focuses on the development of 3D printed channels using the Stereolithography (SLA) technique. Here the fabrication of 3D printed microchannel using the MiiCraft printer is discussed.
- **Chapter 5** illustrates the synthesis of nanoadsorbents applicable for the removal of fluoride from water. The characterization of synthesized nanoadsorbents is performed for their further analysis.
- **Chapter 6** presents work on the fluoride removal efficiency using prepared nanoadsorbents under laboratory conditions and also focuses on the installation of nanoadsorbent loaded 3D printed device applicable for the removal of fluoride from water.
- **Chapter 7** describes the real-time developed system for the removal of fluoride from water using spiraled microchannel.
- And finally, **Chapter 8** provides the overall conclusion and recommendation for further research.

## 1.8 REFERENCES

- Alarcon-Herrera, M. T., MartIn-Dominguez, I. R., Trejo-Vázquez, R., & Rodriguez-Dozal, S. (2001). Well water fluoride, dental fluorosis, and bone fractures in the Guadiana Valley of Mexico. *Fluoride*, 34(2), 139-149.
- Ayoob, S., & Gupta, A. K. (2006). Fluoride in drinking water: a review on the status and stress effects. *Critical Reviews in Environmental Science and Technology*, 36(6), 433-487.
- Badalov, S., & Arnusch, C. J. (2016). Ink-jet printing assisted fabrication of thin film composite membranes. *Journal of membrane science*, 515, 79-85.

- Bell, M., & Ludwig, T. (1970). The supply of fluoride to man: ingestion from water, fluorides and human health, WHO Monograph series 59. *World Health Organization, Geneva*.
- Biswas, K., Bandhoyapadhyay, D., & Ghosh, U. C. (2007). Adsorption kinetics of fluoride on iron (III)-zirconium (IV) hybrid oxide. *Adsorption, 13*(1), 83-94.
- Caminero, M., Chacón, J., García-Moreno, I., & Rodríguez, G. (2018). Impact damage resistance of 3D printed continuous fibre reinforced thermoplastic composites using fused deposition modelling. *Composites Part B: Engineering, 148*, 93-103.
- Cauley, J. A., Buhari, A. M., Murphy, P. A., & Riley, T. J. (1995). Effects of fluoridated drinking water on bone mass and fractures: the study of osteoporotic fractures. *Journal of Bone and Mineral Research, 10*(7), 1076-1086.
- CGWB. (2010). Central Ground Water Board (CGWB), 2010. *Ground Water Quality in Shallow Aquifers of India. Ministry of Water Resources Government of India*. Retrieved from <http://cgwb.gov.in/>
- CGWB. (2014). Central Ground Water Board (CGWB). *Uttar Pradesh*.
- Chinoy, N. (1991). Effects of fluoride on physiology of animals and human beings. *Indian J Environ Toxicol, 1*(1), 17-32.
- Cohen, A., Laviv, A., Berman, P., Nashef, R., & Abu-Tair, J. (2009). Mandibular reconstruction using stereolithographic 3-dimensional printing modeling technology. *Oral Surgery, Oral Medicine, Oral Pathology, Oral Radiology, and Endodontology, 108*(5), 661-666.
- Crump, S. S. (1992). Apparatus and method for creating three-dimensional objects. In: Google Patents.
- DebRoy, T., Wei, H., Zuback, J., Mukherjee, T., Elmer, J., Milewski, J., Zhang, W. (2018). Additive manufacturing of metallic components—process, structure and properties. *Progress in Materials Science, 92*, 112-224.
- Deckard, C. R. (1989). Method and apparatus for producing parts by selective sintering. In: Google Patents.

- Dharmshaktu, N. (2013). A review of the effect of high fluoride content of water on health and environment and the strategy adopted for its prevention and control, with special reference to India.
- Edition, F. (2011). Guidelines for drinking-water quality. *WHO chronicle*, 38(4), 104-108.
- Fawell, J., Bailey, K., Chilton, J., Dahi, E., & Magara, Y. (2006). *Fluoride in drinking-water*: IWA publishing.
- Fawell, J. K., & Bailey, K. (2006). *Fluoride in drinking-water*: World Health Organization.
- Femmer, T., Kuehne, A. J., Torres-Rendon, J., Walther, A., & Wessling, M. (2015). Print your membrane: Rapid prototyping of complex 3D-PDMS membranes via a sacrificial resist. *Journal of membrane science*, 478, 12-18.
- Femmer, T., Kuehne, A. J., & Wessling, M. (2014). Print your own membrane: direct rapid prototyping of polydimethylsiloxane. *Lab on a Chip*, 14(15), 2610-2613.
- Ghosh, A., Mukherjee, K., Ghosh, S. K., & Saha, B. (2013). Sources and toxicity of fluoride in the environment. *Research on Chemical Intermediates*, 39(7), 2881-2915.
- Gonzalez-Gomez, J., Valero-Gomez, A., Prieto-Moreno, A., & Abderrahim, M. (2012). A new open source 3d-printable mobile robotic platform for education. In *Advances in autonomous mini robots* (pp. 49-62): Springer.
- Hu, Y., Xia, C., Dong, Z., & Liu, G. (2017). Geochemical characterization of fluoride in the groundwater of the Huaibei Plain, China. *Analytical Letters*, 50(5), 889-903.
- Hull, C. W. (1986). Apparatus for production of three-dimensional objects by stereolithography. In: Google Patents.
- Ianko, T., Panov, S., Sushchyns'ky, O., Pylypenko, M., & Dmytrenko, O. (2018). Zirconium alloy powders for manufacture of 3D printed articles used in nuclear power industry.

- Kim, K., Zhu, W., Qu, X., Aaronson, C., McCall, W. R., Chen, S., & Sirbuly, D. J. (2014). 3D optical printing of piezoelectric nanoparticle–polymer composite materials. *ACS nano*, 8(10), 9799-9806.
- Kostakis, V., Niaros, V., & Giotitsas, C. (2015). Open source 3D printing as a means of learning: An educational experiment in two high schools in Greece. *Telematics and informatics*, 32(1), 118-128.
- Kumar, M., Das, A., Das, N., Goswami, R., & Singh, U. K. (2016). Co-occurrence perspective of arsenic and fluoride in the groundwater of Diphu, Assam, Northeastern India. *Chemosphere*, 150, 227-238.
- Lapworth, D., Baran, N., Stuart, M., & Ward, R. (2012). Emerging organic contaminants in groundwater: a review of sources, fate and occurrence. *Environmental pollution*, 163, 287-303.
- Lee, J.-Y., An, J., & Chua, C. K. (2017). Fundamentals and applications of 3D printing for novel materials. *Applied Materials Today*, 7, 120-133.
- Li, Y., Liang, C., Slemenda, C. W., Ji, R., Sun, S., Cao, J., Ying, P. (2001). Effect of Long-Term Exposure to Fluoride in Drinking Water on Risks of Bone Fractures. *Journal of Bone and Mineral Research*, 16(5), 932-939.
- Madhnure, P., Sirsikar, D., Tiwari, A., Ranjan, B., & Malpe, D. (2007). Occurrence of fluoride in the groundwaters of Pandharkawada area, Yavatmal district, Maharashtra, India. *Current Science*, 675-679.
- Maheshwari, R. (2006). Fluoride in drinking water and its removal. *Journal of Hazardous Materials*, 137(1), 456-463.
- Miretzky, P., & Cirelli, A. F. (2011). Fluoride removal from water by chitosan derivatives and composites: a review. *Journal of Fluorine Chemistry*, 132(4), 231-240.
- Murphy, S. V., & Atala, A. (2014). 3D bioprinting of tissues and organs. *Nature biotechnology*, 32(8), 773.
- Organization, W. H. (1996). Health criteria and other supporting information. *Guidelines for drinking-water quality*, 2, 796-803.
- Peltola, S. M., Melchels, F. P., Grijpma, D. W., & Kellomäki, M. (2008). A review of rapid prototyping techniques for tissue engineering purposes. *Annals of medicine*, 40(4), 268-280.

- Raza, M., Farooqi, A., Niazi, N. K., & Ahmad, A. (2016). Geochemical control on spatial variability of fluoride concentrations in groundwater from rural areas of Gujrat in Punjab, Pakistan. *Environmental Earth Sciences*, 75(20), 1364.
- Rengier, F., Mehndiratta, A., Von Tengg-Kobligk, H., Zechmann, C. M., Unterhinninghofen, R., Kauczor, H.-U., & Giesel, F. L. (2010). 3D printing based on imaging data: review of medical applications. *International journal of computer assisted radiology and surgery*, 5(4), 335-341.
- Russell, D. B., Anderson, T., Bredt, J. F., Vogel, M. J., Seymour, M., Bornhorst, W. J., & Hatsopoulos, M. I. (1999). Method and apparatus for prototyping a three-dimensional object. In: Google Patents.
- Sahu, P. (2019). Fluoride pollution in groundwater. In *Groundwater Development and Management* (pp. 329-350): Springer.
- Sahu, P., Kisku, G. C., Singh, P. K., Kumar, V., Kumar, P., & Shukla, N. (2018). Multivariate statistical interpretation on seasonal variations of fluoride-contaminated groundwater quality of Lalganj Tehsil, Raebareli District (UP), India. *Environmental Earth Sciences*, 77(13), 484.
- Séquin, C. H. (2005). Rapid prototyping: a 3d visualization tool takes on sculpture and mathematical forms. *Communications of the ACM*, 48(6), 66-73.
- Smedley, P. Fluoride in groundwater. Retrieved from <https://www.bgs.ac.uk/research/groundwater/health/fluoride.html>
- Smet, J. (1992). *Fluoride in drinking water*. Paper presented at the Symposium on Endemic Fluorosis in developing countries.
- Standard, I. (1991). Drinking water-specification. *1st Revision, IS, 10500*.
- Standards), B. B. o. I. (2012). Specification for drinking water IS 10500: 2012. In. New Delhi, India.
- Stansbury, J. W., & Idacavage, M. J. (2016). 3D printing with polymers: Challenges among expanding options and opportunities. *Dental Materials*, 32(1), 54-64.

- Suthar, S., Garg, V. K., Jangir, S., Kaur, S., Goswami, N., & Singh, S. (2008). Fluoride contamination in drinking water in rural habitations of Northern Rajasthan, India. *Environmental Monitoring and Assessment*, *145*(1), 1-6.
- Teotia, S., & Teotia, M. (1994). Dental caries: a disorder of high fluoride and low dietary calcium interactions (30 years of personal research). *Fluoride*, *27*, 59-59.
- Tofail, S. A., Koumoulos, E. P., Bandyopadhyay, A., Bose, S., O'Donoghue, L., & Charitidis, C. (2018). Additive manufacturing: scientific and technological challenges, market uptake and opportunities. *Materials today*, *21*(1), 22-37.
- Tseng, P., Murray, C., Kim, D., & Di Carlo, D. (2014). Research highlights: printing the future of microfabrication. *Lab on a Chip*, *14*(9), 1491-1495.
- WHO. (2011). *Guidelines for drinking water quality*. World Health Organ. Retrieved from
- Zhu, C., Han, T. Y.-J., Duoss, E. B., Golobic, A. M., Kuntz, J. D., Spadaccini, C. M., & Worsley, M. A. (2015). Highly compressible 3D periodic graphene aerogel microlattices. *Nature communications*, *6*, 6962.

## **CHAPTER 2**

### **LITERATURE REVIEW**

*This chapter discusses the available fluoride removal technique and various adsorbents used applicable for the removal of fluoride alongwith their adsorption capacity, kinetics, isotherm, and thermodynamics. Detailed literature on 3D printing application for water treatment is also described.*

#### **2.1 INTRODUCTION**

To maintain the WHO permissible limit, various fluoride removal methods have been reported in the literature that has their own merits and demerits with respect to their operational conditions *e.g.*, optimal pH, temperature, removal efficiency, operational costs as well as their disposal. And also various available additive manufacturing (AM) techniques alongwith their materials used specific benefits and drawbacks which allow them more suitable for particular implementations than others are discussed here.

#### **2.2 FLUORIDE REMOVAL TECHNIQUES**

The overview of major techniques used to remove the contaminants are ion exchange (Markovski, Garcia, Hristovski, & Westerhoff, 2017; Mondal et al., 2018; Y.-X. Zhang & Jia, 2018), coagulation (Dubey, Agarwal, & Gupta, 2018; Gan et al., 2019), electrocoagulation (Behbahani, Moghaddam, & Arami, 2011; López-Guzmán, Alarcón-Herrera, Irigoyen-Campuzano, Torres-Castañón, & Reynoso-Cuevas, 2019; Mena et al., 2019), membrane filtration (Nunes-Pereira et al., 2018; Richards, Vuachère, & Schäfer, 2010; J. Zhang, Chen, Su, Li, & Feng, 2017) and adsorption (Bhatnagar, Kumar, & Sillanpää, 2011; Gong, Qu, Liu, & Lan, 2012; Kuang, Liu, Fu, & Zhao, 2017; Wang, Wu, Li, Tang, & Zhang, 2018) are described in the continuing subdivision.

### 2.2.1 ION EXCHANGE PROCESS

The ion exchange process (IEP) occurs as a reversible exchange of ions between solid and liquid phases (Etzel & Wachinski, 1997). Ion exchange resin is a solid phase, insoluble in water and carries exchangeable ion, without significant structural changes. The ion exchangers are divided into cation and anion exchangers. Typically used cation and anion exchange reactions are shown in (1) and (2), respectively, where U is the structural unit of the ion exchanger. Both the reaction is reversible in nature. The reaction (1) is considered for the water softening process (Helfferich, 1995).

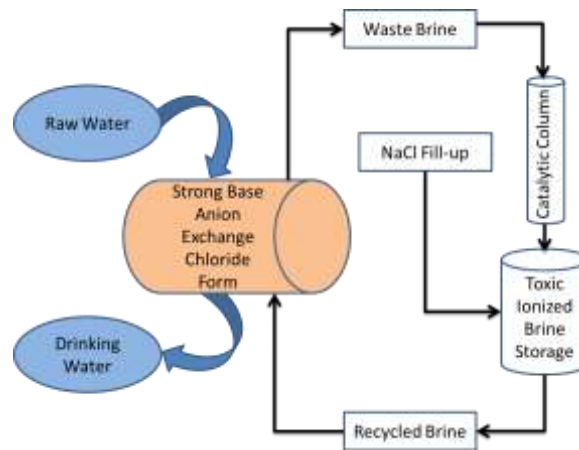
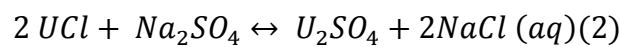
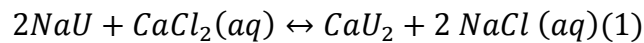


**Fig 2.1** IEP shows anion exchange using strong base anion exchange using chloride form (Patel et al., 2019)

Fig 2.1 shows the mechanism of the ion exchange process that consists of the following steps:

- Contaminated water passed through the ion exchanger for anion/cation exchange.
- Waste brine generated passed through the catalytic column and collected in brine storage.
- Waste Brine is recycled by continuous sodium chloride salts which are again given to the ion exchanger.

In the ion exchanger, the main requirements are hydrophilicity, chemical, and physical stability, a high rate of ion exchange with a surplus capacity of ion



exchange. Although this process can effectively remove ions but, adversely affected due to the presence of other ions. The medium operational cost may get expensive due to the waste brine generated which requires disposal arrangement and the ion exchange resin.

Many sources emphasized the effectiveness of ion exchange with other techniques (Onyango, Kojima, Kuchar, Osembo, & Matsuda, 2005; Onyango et al., 2006). Typically, the removal of fluoride occurs through adsorption in the ion exchange process rather exchange of ions. The main explanation, presence of fluoride concentration in water is less in comparison to other ions present in water. For  $F^-$  removal cation exchange resins are more selective than anion exchange resins (Meenakshi & Viswanathan, 2007). The fluoride removal ability and selectivity for fluoride however depend on the resin form. The packing of metal ions has an intense impact on fluoride elimination owing to differences in its properties (Luo & Inoue, 2004). Therefore optimizing the defluoridation efficiency of ion exchange resins, while at the same time increasing the selectivity of fluoride is complex.

Indion FR 10 ion exchanger which is commonly available was used for the removal of fluoride by Viswanathan and Meenakshi. Chemically modified  $Ce^{3+}$ ,  $Fe^{3+}$ ,  $La^{3+}$ , and  $Zr^{4+}$  compounds have been used to study their defluoridation selectivity. The average defluoridation potential of all adjusted resins was approximately 0.5 mg/g. The researchers found out that defluoridation was allied to electrostatic adsorption and complexation. Further Indion FR 10 has been altered into  $Na^+$  and  $Al^{3+}$  forms by packing metal ions into  $H^+$  resin form (Viswanathan & Meenakshi, 2008, 2009).

### **2.2.2 COAGULATION AND ELECTROCOAGULATION**

In the coagulation process (Fig 2.2) the contaminated water is collected in a coagulation tank where organic or mineral coagulants (alum, lime and carbon dioxide *etc.*) are added. During this process, the smaller particles stick to one another forming a larger particle. The formed larger particles are heavy enough to settle down in a sedimentation tank and the water is allowed to pass through the filtration set up where fine, granulated materials are used like sand/sand with coal as per requirement. Filtrated water is passed for a

disinfectant process where bacteria, viruses, and other microbes are removed and finally the pH of water is maintained.

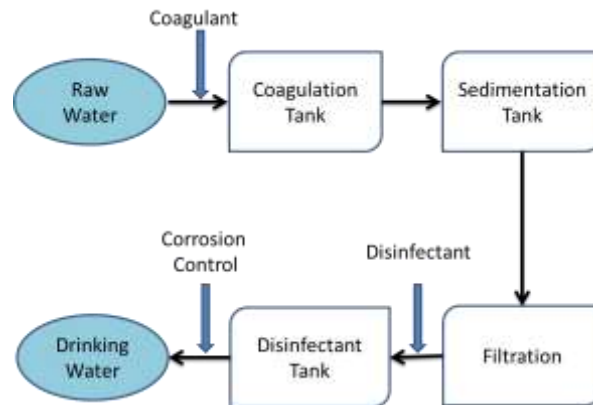
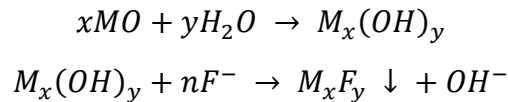


**Fig 2.2** Schematic of a coagulation process

Around 70% removal efficiency is reported with coagulation, but due to high maintenance cost and a large area for sludge drying, unpleasant water taste and a very high residual amount limit its operation spectrum.

The key reaction is as follows:

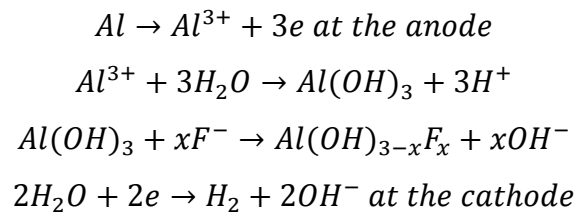


where “M” used here denotes metal.

One of the oldest techniques to use aluminum salt, lime, and bleaching powder in coagulation for removing fluoride from water and accompanied by filtration (Nawlakhe, WG, & KR, 1975). For coagulating fluoride from water sodium dihydrogen phosphate and calcium chloride blended bone charcoal (Dahi, 1996), magnesium oxide (Rao & Mamatha, 2004), calcite (Aldaco, Garea, & Irabien, 2007) have also been used. These processes were commonly being used in the Indian villages and were efficiently capable for the removal of fluoride from water. Further these treatment procedures leaves residual metal ions in water at harmful concentrations. Coagulation of fluoride containing water using aluminum salt, lime, and alum found to introduce aluminum ions in undesirable concentrations (George, Pandit, & Gupta, 2010). Similarly, phosphate ions were observed in treated water at harmful concentrations when coagulation was performed using dihydrogen phosphate containing bone charcoal (Ritz, Hahn, Ketteler, Kuhlmann, & Mann, 2012).

Electrocoagulation deals with electrochemical development of destabilizing agents which lead to electric charge neutralization for pollutant removal. Charged particles together coagulate to form a mass. Effective removal of pollutants by flotation and sedimentation is intensified by metal-based coagulants having a similar effect as anode-produced metal cations.

The basic reactions are as follows (Zuo, Chen, Li, & Chen, 2008):



The choice of electrode materials in electrocoagulation depends on different factors, including cost-effectiveness, low oxidation capacity, stiffness in the underlying structure, etc. Different electrodes such as carbon (Alvarez-Gallegos & Pletcher, 1999), iron (Yildiz, 2007), titanium graphite (Linares-Hernández, Barrera-Díaz, Roa-Morales, Bilyeu, & Ureña-Núñez, 2007), aluminium (Bi, Wang, Cao, & Zhang, 2004; Ghosh, Medhi, & Purkait, 2008) and mild steel (Golder, Hridaya, Samanta, & Ray, 2005) have been reported in literature. In favorable conditions of activity, aluminum was seen to be very productive and effective in the removal of fluoride (Ghosh et al., 2008).

### 2.2.3 MEMBRANE

In membrane technology (Fig 2.3) the defined processes are microfiltration, ultrafiltration, nanofiltration, and reverse osmosis. For the removal of harmful ions, nanofiltration and reverse osmosis are generally being applied. These processes are effective but, operational cost, wastage of water and total dissolved solid disposal are very high.

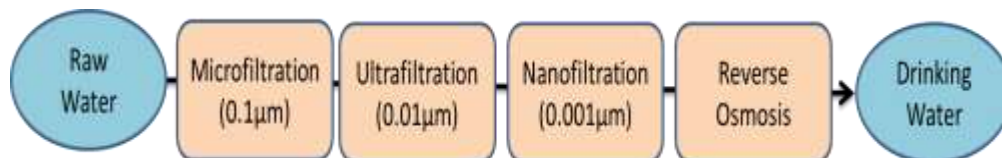


**Fig 2.3** Membrane Technology

In comparison to reverse osmosis (RO), ultrafiltration (UF), and microfiltration (MF), nanofiltration (NF) is a comparatively new method and

is emerging as a technically operational technology in the treatment of industrial wastewaters. Nanofiltration is defined by reverse osmosis (RO) to ultrafiltration (UF) features. Apart from the similarities in process with RO, NF is performed at a comparatively lower pressure producing the same permeate flux even at reduced pressure. Less than 60 per cent of monovalent ions are removed using NF whereas RO membranes removed 90 per cent. For complete demineralization of water RO is the best technique (Alarcón-Herrera et al., 2013). In fact, nominal removal of fluoride may be accomplished by modifying the functional variables for the NF process; thus maintaining the necessary fluoride concentration in the water at the same time.

NF90 and NF400 are the two most widespread NF membranes that are used for the removal of fluoride from water (Tahaikt et al., 2007). For lower fluoride concentration removal, the NF400 membrane shown better results. But for higher fluoride concentration the water has to be passed twice through the membrane so as to reduce the fluoride concentration up to an acceptable range (Elazhar et al., 2009). The fluoride removal efficiency of negatively charged thin-film composite (TFC) NF membranes was studied. The researchers also reported that high pressure has a major positive impact on fluoride removal along with enhanced flux (K. Hu & Dickson, 2006).

For promoting the removal of fluoride and chloride, the NF membrane that are commercially available were altered layer by layer assembly of alternating polyelectrolyte thin films (Malaisamy, Talla-Nwafo, & Jones, 2011). Here the anionic polyelectrolyte was polystyrene sulfonate (PSS) and the cationic polyelectrolyte was poly diallyl dimethyl ammonium chloride (PDADMAC). The substrate membrane was deposited with a thin range (0.5 – 8.5 mm) bilayers of PDADMAC/PSS. The modified membrane showed better fluoride removal efficiency in comparison to the unmodified membrane that is around 70 per cent and 40 per cent respectively. The selectivity for chloride was observed to be much better with respect to fluoride (Malaisamy et al., 2011).

#### **2.2.4 ADSORPTION**

Due to the cost-effectiveness, easy to operate, environment-friendly nature adsorption has been a process of a chance to remove contaminants. The

selection of adsorption has a major role in the removal efficiency of contaminants depending on the capability to adsorb from an aqueous solution that depends on the pH range, adsorbent stability, effective adsorption capacity, adsorption rate, and cost-effectiveness. The adsorption process consists of the following major steps (Fig 2.4)(Fan, Parker, & Smith, 2003):

- i. Mass exchange of toxic matters to the outer surface of the adsorbent.
- ii. Toxic matter adsorption onto outside molecule surface.
- iii. Intra-molecule dispersion of the toxic matters from the outside surface and conceivable interchanges with components on pore surface inside particles.

Generally, the adsorbate is dispersed on the surface of adsorbents and after the dispersion on the outer surface of the adsorbent, adsorbate is diffused on accessible pores of the adsorbent. All accessible uncovered dynamic areas are possessed through the adsorption procedure directed by either physisorption or chemisorption phenomena.

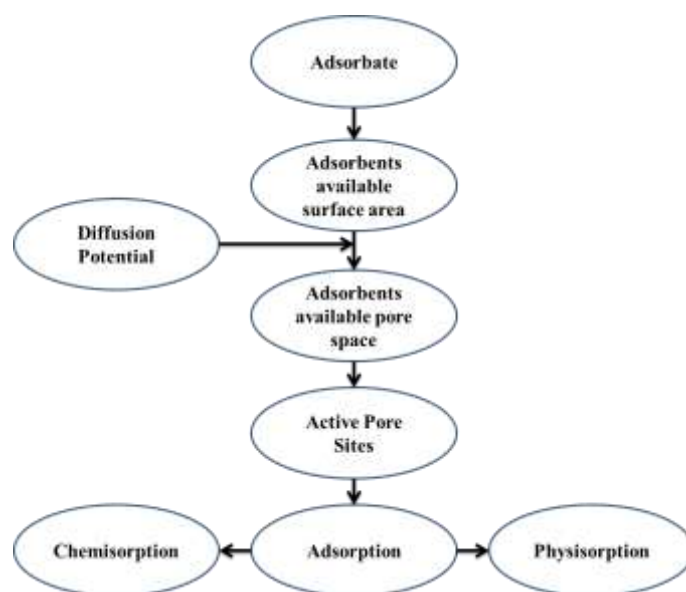
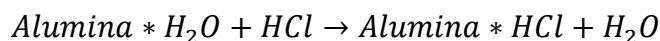


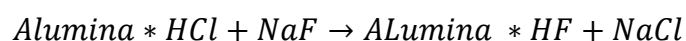
**Fig 2.4** Flow chart of the adsorption phenomenon (Lata & Samadder, 2016)

The most popular and extensively used adsorbent for the removal of fluoride as per many research reports is activated alumina (Chauhan, Dwivedi, & Iyengar, 2007). Its popularity as adsorbents is due to its structural stability without shrinkage, swelling, or disintegration in water (Serbezov, Moore, &

Wu, 2011). For adsorption the major parameter is specific surface area and the granules of activated alumina were having a very high specific surface area of ~200-300 m<sup>2</sup>/g due to which for adsorption the number active sites were extensively available. The process occurs in the following way,



(\* activated state)



In addition, regeneration is done first with alkaline solution treatment of an adsorbent followed by acid washing (Bansiwal, Pillewan, Biniwale, & Rayalu, 2010; Ghorai & Pant, 2005).

The comparative analyses of all the existing Fluoride removal technologies are discussed in Table 2.1.

**Table 2.1** A comparative analysis of the removal technologies of toxic ions in water.

Technologies	Operational Parameter and Efficiency				
	pH and Temperature	Post-treatment	Removal Efficiency	Operational Cost	Disposal
Ion Exchange	Not important	Required due to corrosivity of product water	Approx. 90%	Medium	Waste brine
Coagulation-Precipitation	Important	Required due to the production of by-products	>60-70%	High	Waste
Membrane Process	Not important	Required due to corrosivity of product	>95%	High	High total dissolved solids (TDS)

		water			
Adsorption	Important	Often not required	Varies with adsorbent	Medium	Saturated / spent adsorbent

## 2.3 NANOADSORBENTS FOR FLUORIDE REMOVAL

Extensively utilized adsorbents for the adsorption of toxic ions are carbon nanotubes, activated carbon, metal composites, mixed metal oxides, clay minerals, biomaterials, and zeolites. Besides the above, natural materials, industrial residues, as well as agricultural residues, are also utilized as cost-effective adsorbents. In this section, different adsorbents, focused on their adsorption capacity, concentration range, contact time, pH, kinetic model, isotherm model, and thermodynamics are discussed for the removal of fluoride and summarized in Tabel 2.2.

### 2.3.1 CARBON NANOTUBES

Carbon nanotubes (CNTs) have shown their role in the removal of organic and inorganic contaminants present in water. Hydroxyapatite-multi-walled carbon nanotubes (HA-MWCNTs) of 25 nm having a surface area of 180.5 m<sup>2</sup>/g were prepared via the sol-gel method by Ruan et al. (Ruan et al., 2017). The prepared HA-MWCNTs showed 1.6 times more adsorption capacity as compared to only hydroxyapatite (HA). The adsorbent showed a decrease in the concentration of fluoride from 8.79 to 0.25 mg/L in 3h duration and at neutral pH. This ability suggests that the above adsorbent can be used as a cost-effective, better adsorbent for the treatment of water contaminated with fluoride.

Tang et al. (Tang, Duan, Li, Zhang, & Wu, 2018), also reported hydroxyapatite modified CNT (CNT-HAP) as an adsorbent for fluoride removal under acidic conditions, claiming an increased adsorption capacity of the adsorbent to 11.05 mg/g. The nano alumina modified CNT (Smitha & Thampi, 2017), aligned CNT (Y.-H. Li et al., 2003), and Al<sub>2</sub>O<sub>3</sub> supported CNT (Y.-H. Li et al., 2001) were also reported to be adsorbent at different pH range. The adsorption capacity of aligned CNT was relatively lower (4.5

mg/g) as compared to nano alumina CNT and CNT-HAP, having an adsorption capacity of 11 mg/g. The use of nano alumina CNT may be a better option for the removal of fluoride as it required only 1h to attain the equilibrium at pH 6-7. All of them observed to be following the Freundlich adsorption isotherm suggesting the multiple layer adsorption process over modified CNT. This offers them a better applicant to use an adsorbent for fluoride removal from an aqueous solution between pH 5-9.

### **2.3.2 METAL BASED**

The use of cost-effective iron oxide nanoparticles, the composite material has gained attention due to its use as an adsorbent. Various researchers had prepared these materials and tested their efficiency under a different experimental condition involving pH, time, temperature, and concentration of fluoride ion solution. The efficiency of the above-prepared material varies greatly with the size, coating as well as experimental conditions. The kinetics, as well as isotherm behaviour, also observed to be varied.

Iron oxide prepared by wet chemical precipitation route and treated with ethanol was reported to be a better adsorbent having 60.8 mg/g adsorption capacity at pH 3.5-10.3 (C. Zhang, Li, Wang, Jiang, & Fok, 2017).

Modified and unmodified magnetic iron oxide nanoparticles were found to be better adsorbents for fluoride ion removal. Fe<sub>3</sub>O<sub>4</sub> nanoparticles coated with alginate-lanthanum have shown the adsorption capacity 45.2 mg/g at pH 4 by Zhang et al.(Y. Zhang, Lin, Zhou, & Luo, 2016). Magnetic nano-adsorbent of iron aluminium oxide was prepared by mixing graphene oxide by Li et al.(Liu, Cui, Ma, Cui, & Zhang, 2016) they claimed that the adsorbent was pH-independent, paramagnetic, and highly selective for fluoride ion. The recovery of the adsorbent from the solution was very easy as it required only the external magnetic field. The adsorption was found to be due to electrostatic attraction, anion exchange, and inner-sphere complex formation.

The use of non-magnetic iron oxide-hydroxide nanoparticles having a spherical shape for the removal of fluoride from water is reported by Raul et al.(Raul et al., 2012). They claimed that up to 70% of fluoride can be removed depending upon the optimized parameters. They also studied the impact of



other anions for e.g., fluoride, iodate, iodide, and sulphate as co-contaminants. They observed that their adsorbent was highly selective for fluoride ion.

Li and Qi et al. (Li Li, Zhu, Man, & Xing, 2017) prepared a Fe-Al-La tri-metal hydroxide adsorbent having a surface area of 371.47 m<sup>2</sup>/g by utilizing iron and aluminium as the main raw material from red mud. High fluoride removal efficiency in a wide pH range from 3-9, with a capacity of 74.07 mg/g was observed through electrostatic interaction and ion-exchange by trivalent metals of composites.

The fluoride adsorption onto the hydroxide flocs of Al(III), Fe(III), and their mixture was studied by Hamamoto et al. (Hamamoto & Kishimoto, 2017) where they found that Al(III) hydroxide flocs have maximum adsorption capacity at the equilibrium concentration of 8 mg/L. The adsorption occurs via a two-step process and the simultaneous dosing of Al (III) and Fe (III) appears to be an effective option for fluoride removal.

Zhou et al. (Jian Zhou et al., 2018), prepared a high-performance Zr-Al-La tri-metal composite (AZL) having a robust adsorption capacity of 90.48 mg/g at pH 3 and room temperature. They claimed that the incorporation of lanthanum in the composite was the key factor to improve the active sites, resulting in the better removal of fluoride.

Reusable MnO<sub>2</sub> coated by Na-bentonite of 5.91 nm and 58.25 m<sup>2</sup>/gm surface area was reported to be robust adsorbent having a 91 per cent removal capacity (for a fluoride solution of 5 mg/L) and following Langmuir model by Mudzielwana et al. (Mudzielwana, Gitari, Akinyemi, & Msagati, 2017).

Earlier researches have shown strong fluoride removal capacity using titanium dioxide (TiO<sub>2</sub>) and TiO<sub>2</sub> composites from an aqueous solution (Chen, He, He, Wang, Su, & Jin, 2012; Suriyaraj, Bhattacharyya, & Selvakumar, 2015; Suriyaraj, Vijayaraghavan, Biji, & Selvakumar, 2014; Yan, Song, Wang, Hu, & Yang, 1998). Microbially prepared TiO<sub>2</sub> nanoadsorbent was investigated for the removal of fluoride and it was observed that the anatase TiO<sub>2</sub> shown better fluoride adsorption in comparison to other phases of TiO<sub>2</sub> (Suriyaraj et al., 2014). Researchers also investigated that if other materials can be loaded with TiO<sub>2</sub> nanoadsorbent, it can overcome the following limitations like easy agglomeration, regeneration, and reduce the possible contamination of the

environment (Chen, He, He, Wang, Su, & Jin, 2012). In comparison, the composite TiO<sub>2</sub> nanoadsorbent demonstrated significantly greater efficiency in terms of the absorption of fluoride from the aqueous medium than the pure TiO<sub>2</sub> adsorbents (Chen, He, He, Wang, Su, Zhang, et al., 2012; J. Wu, Zhou, Chen, & Zhao, 2012; Yan et al., 1998). Ishihara et al. used titanium hydroxide and TiO<sub>2</sub> rutile for fluoride removal at pH 5 (Ishihara et al., 2002). Hydrated TiO<sub>2</sub> has shown better removal capacity for arsenic compounds and halogens present in water (Tokunaga et al., 1995; Masamichi Tsuji & Abe, 1986; M Tsuji & Abe, 1991). Various other researchers have also performed the study to analyze the efficiency of titanium dioxide and its composite for the removal of fluoride from water (Babaeiveli & Khodadoust, 2013; Liang, Xue, Gao, & Yang, 2017).

Lithium/aluminium layered double hydroxides (Li/Al-LDHs) having petal-like assemblies and hexagonal nanosheets of different size were prepared by Zhou et al. (Jiabin Zhou, Cheng, Yu, & Liu, 2011) using the hydrothermal route. The prepared sample has high hierarchical pores, small, large as well as macropores of different sizes. They showed an excellent fluoride adsorption capacity of 158.7 mg/g for fluoride concentration up to 200 mg/L, under acidic as well as basic pH range.

Jayarathna et al. (Jayarathna, Bandara, Ng, & Weerasooriya, 2015) studied  $\gamma$ -Fe<sub>2</sub>O<sub>3</sub> nanoparticles synthesized by the co-precipitation method. The synthesized nanoparticles were around 5-20 nm and they studied the batch adsorption process for the adsorption efficiency of the same for fluoride removal. During the process, it was observed that these iron nanoparticles showed high efficiency of adsorption at initial duration for about 15 min and it removed 95% of fluoride and after that, it reached an equilibrium condition. Adsorption of fluoride completely depends on the pH of the water and it was seen that for higher adsorption rate pH should be lower. In Fig 2.5, the mechanism is explained for the adsorption of fluoride using  $\gamma$ -Fe<sub>2</sub>O<sub>3</sub> nanoparticles whereas Fig 2.6, shows an improved configuration of Fe<sub>2</sub>(OH)<sub>6</sub>(H<sub>2</sub>O), Fe<sub>2</sub>(OH)<sub>5</sub>(H<sub>2</sub>O)<sub>4</sub>F and Fe<sub>2</sub>(OH)<sub>4</sub>(H<sub>2</sub>O)<sub>4</sub>F<sub>2</sub> clusters.

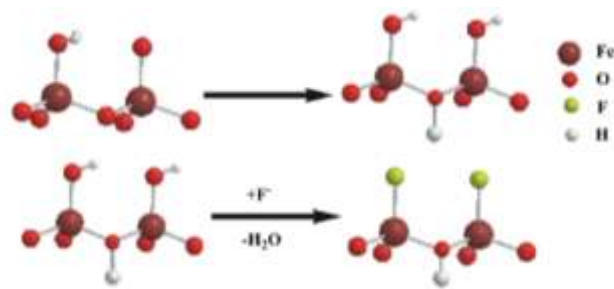


**Fig 2.5** Suggested mechanism for the adsorption of F on  $\gamma$ -Fe<sub>2</sub>O<sub>3</sub> nanoparticles (Jayarathna et al., 2015)



**Fig 2.6** Improved configuration of Fe<sub>2</sub>(OH)<sub>6</sub>(H<sub>2</sub>O)<sub>4</sub>, Fe<sub>2</sub>(OH)<sub>5</sub>(H<sub>2</sub>O)<sub>4</sub>F and Fe<sub>2</sub>(OH)<sub>4</sub>(H<sub>2</sub>O)<sub>4</sub>F<sub>2</sub> clusters (Blue colour Fe, Red colour O, Off white colour H and Off green colour F) (Jayarathna et al., 2015)

Alumina adsorbent was used for fluoride (Ghorai & Pant, 2005; Ku & Chiou, 2002; Maliyekkal, Shukla, Philip, & Nambi, 2008; Tripathy, Bersillon, & Gopal, 2006), removal from water. The regular alumina adsorbents have undefined pore structures along with less adsorption capacity and due to this, the removal efficiency of the toxic matter is having a slow rate. In order to have better removal efficiency, the adsorbent should have equally available pores, an interlinked pore framework, a high surface area, and physical as well as chemical stability.

Lee Grace et al. (G. Lee, Chen, Yang, & Ahn, 2010) studied two types of mesoporous alumina (MA) samples. These MA models were arranged by utilizing aluminium tri-sec-butoxide in the occurrence of cetyltrimethylammonium bromide (MA-1) moreover stearic acid (MA-2) as structure leading cause, and then tried on the defluoridation of water. These ingredients comprise a wormhole - mesoporous structure with an external area of 421 and 650 m<sup>2</sup>/g along with the pore capacity of 0.96 and 0.59 cm<sup>3</sup>/g. Mesoporous alumina showed an essentially enhanced adsorption limit of 14.26

mg/g and an adsorption rate of 14.6 mg/g min that is much higher than the available regular activated alumina (AA) during defluoridation method. MA-2 exhibited an effective adsorption limit of fluoride from water in comparison to the commercially available gamma-alumina. Textural highlights of the bigger external region and moderately small pore measure in MA-2 in comparison to contrasted with the AA are accepted to be an efficient sorbent for adsorption processes.

Qiao et al. (Qiao, Cui, Sun, Hu, & Guan, 2014) studied the performance of Al-Fe (hydr)oxides for the removal of fluoride from the water. A series of Al-Fe (hydr)oxides with different ratios of Al : Fe was synthesized using the co-precipitation method for various Al : Fe ratio. During the adsorption, behaviour of the prepared sample was found to be better for the adsorbent having Al: Fe (4:1) at the pH range of 5-9. The removal efficiency increases with increasing Al content in adsorbent in the pH range of 6.5. The order of the adsorption capacity of adsorbents for removing fluoride from the water was followed by 4Al : Fe > Al : Fe > Al : 4Fe > Fe.

Wu et al. (K. Wu et al., 2017) showed the adsorption efficiency of Mn-Al binary oxide (MABO) for the removal of As(III/V) and F. The efficiency of MABO was affected by As(III/V), pH, and Mn/Al molar ratios and the adsorption rate of As (V), As(III) and F ions vary on the active surfaces of MABO.

### **2.3.3 MISCELLANEOUS**

#### **2.3.3.1 CALCIUM BASED**

Calcium salt shows a great affinity towards fluoride, therefore, extensive researches are reported for the removal of fluoride. Turner *et al.* (Turner, Binning, & Stipp, 2005) demonstrated fluoride removal using crumpled calcium carbonate adsorbent (150-300  $\mu\text{m}$ ) for fluoride ion concentration in between 3-2100 mg/L.

For defluoridation of water, activated quicklime adsorbent (<150  $\mu\text{m}$ ) was reported by Islam and Patel (Islam & Patel, 2007). They observed that more than 80 per cent of fluoride was removed from a fluoride solution of 50 mg/L

concentration. Langmuir maximum adsorption ability of the same was found to be 16.67 mg/g.

Besides the above aluminum hydroxide impregnated limestone adsorbent (Jain & Jayaram, 2009) and calcium impregnated activated charcoal (Roy, Das, Sengupta, & Manna, 2017) were also reported as an adsorbent for removal of fluoride.

### **2.3.3.2 NATURAL MATERIALS**

Several uncharged naturally available materials have also been studied for the exclusion of fluoride from drinking water. The efficiency of three different coal-based adsorbents: lignite, fine coke, and bituminous coal were also reported for defluoridation water by Sivasamy *et al.* (Sivasamy, Singh, Mohan, & Maruthamuthu, 2001). They showed that the adsorption process was varied with the above adsorbents and pH 6-12. They show that the fluoride ion efficiency was found to be between 77-85 per cent for 90 mg/L fluoride solution. They also show that the pH was a key factor for fine coke and bituminous for which acidic pH was favourable.

The other natural materials reported for the defluoridation of water are Assam coal (Borah & Dey, 2009), fire clay chips (Moges, Zewge, & Socher, 1996), and montmorillonite clay (Karthikeyan, Pius, & Alagumuthu, 2005). The adsorption capacities of the above natural materials were found to be pH-dependent.

### **2.3.3.3 AGRICULTURAL RESIDUES**

Agricultural residues are low cost and abundant resources which were used for adsorption of fluoride. Parmar *et al.* (Parmar, Patel, Sudhakar, & Koshy, 2006) show that the corn cob based agricultural residue can be modified with aluminium and calcium to form better adsorbent having more than 88% of adsorption capacity, as compared to an unmodified corn cob.

The other agricultural residues reported for removal of fluoride by various researchers are coconut shell, rice husk (Mohan, Singh, & Singh, 2008), and cashew nut sheath (Sivabalan, Rengaraj, Arabindoo, & Murugesan, 2003). The efficiencies were varied with their surface area and pH condition.

#### **2.3.3.4 INDUSTRIAL RESIDUES**

Solid waste industrial materials are major residue discharged by industries. Since they are in-expensive adsorbents, they can be used for the removal of fluoride from water. Among these materials fly ash (Chaturvedi, Yadava, Pathak, & Singh, 1990), aluminium industry waste (Nigussie, Zewge, & Chandravanshi, 2007) was reported to be better adsorbent for fluoride ion in between the pH range of 3-8.

#### **2.3.3.5 BUILDING MATERIALS**

According to Yadav *et al.* (Yadav, Kaushik, Haritash, Kansal, & Rani, 2006), the adsorption capacity of building material derived brick powder were found to superior over activated charcoal for removal of fluoride under below pH 6. The other building material for *e.g.*, gas concrete (Oguz, 2005) and hydrated cement (Kagne et al., 2008) were also studied for the chemisorption followed by precipitation of calcium and aluminium salt of fluoride by XRD.

Table 2.2 presents a summary of adsorption capacity, kinetics, isotherm and thermodynamics of various adsorbents used for the removal of fluoride from water. Mostly previous researchers used fluoride spiked water for their studies. In most of the studies, the pseudo-second-order kinetic model was found to be well fitted with the experimental data and followed Langmuir, Freundlich, and both isotherm models. Furthermore, the thermodynamics of the adsorption of the process was found to be mainly endothermic.

**Table 2.2** Adsorption capacity of various adsorbents under defined parameters for the removal of fluoride.

	<b>Adsorbent</b>	<b>Adsorption Capacity (mg/g)</b>	<b>Conc. Range (mg/L)</b>	<b>Contact Time (h)</b>	<b>pH range</b>	<b>Kinetics</b>	<b>Isotherm</b>	<b>Thermodynamics</b>	<b>Reference</b>
<b>Carbon nanotubes (CNTs)</b>	Nano Hydroxyapatite	17.80	3-50	3	7	Pseudo-second	Langmuir	Endothermic	(Ruan et al., 2017)
	Hydroxyapatite/multi-walled carbon nanotubes	30.22	3-50	3	7	Pseudo-second	Freundlich	Endothermic	(Ruan et al., 2017)
	CNT-HAP	11.05	10	24	3-11	Pseudo-second	Freundlich	Endothermic	(Tang et al., 2018)
	Nano alumina modified CNT	11	10	1	6.0-7.0		Freundlich	Exothermic	(Smitha & Thampi, 2017)
	Aligned CNT	4.5	15	1	7		Freundlich and Langmuir	-	(Y.-H. Li et al., 2003)
<b>Metal Based</b>	Iron oxide	60.8	50	.5	3.5-10.3	Pseudo-	Langmuir	-	(C. Zhang et

						second			al., 2017)
	Core shell Fe <sub>3</sub> O <sub>4</sub> @Alg inate-La	45.2	80	15	4	Pseudo- second	Freundlich	Exothermic	(Y. Zhang et al., 2016)
	Fe-Al-La trimetal hydroxides	74.07	10	4	3.0-9.0	Pseudo- second	Langmuir	-	(Li Li et al., 2017)
	Iron oxide- hydroxide	16.7	10-20	24	2-11		Freundlich	-	(Raul et al., 2012)
	Iron aluminium oxide- graphene oxide	64.73	2-50	20	3.0-9.0	Pseudo- second	Langmuir	-	(Liu et al., 2016)
	Iron aluminium oxide	46.54	2-50	20	3.0-9.0	Pseudo- second	Langmuir	-	(Liu et al., 2016)
	Al-Zr-La trimetal Hydroxide	90.5	200	10	3.0-10.0	Pseudo- second	Langmuir	Endothermic	(Jian Zhou et al., 2018)
	MnO <sub>2</sub> coated Na-	0.65	5	.5	2.0-12.0	Pseudo- second	Langmuir	-	(Mudzielwan a et al., 2017)



	bentonite								
	Li/Al-LDH	158.7	200	2	3.0-13.0	Pseudo-second	Freundlich	Endothermic	(Jiabin Zhou et al., 2011)
<b>Miscellaneous</b>	Quick Lime	16.7	10-50	1.5	-	First	Langmuir	Endothermic	(Islam & Patel, 2007)
	Lime stone	43.1	0-100	5	8.0	-		Endothermic	(Jain & Jayaram, 2009)
	Aluminium hydroxide impregnated lime stone	83.0	0-100	5	8.0	Pseudo-first	Freundlich	Endothermic	(Jain & Jayaram, 2009)
	Calcium impregnated activated charcoal	46.32	50	1	-	Pseudo-second	Langmuir	Exothermic	(Roy et al., 2017)
	Lignite	7.0	3.90	10	5.0-10.0	First	Langmuir and Freundlich	-	(Sivasamy et al., 2001)
	Fine coke	6.9	3.90	10	5.0-10.0	First	Langmuir and Freundlich	-	(Sivasamy et al., 2001)

Bituminous coal	7.4	3.90	10	5.0-10.0	First	Langmuir and Freundlich	-	(Sivasamy et al., 2001)
Fire Clay chips	72-90%	5-20	-	5.0-7.0	-	-	-	(Moges et al., 1996)
Montmorillonite clay	1.4	3.0	1	Neutral	First	Langmuir	Endothermic	(Karthikeyan et al., 2005)
Aluminium treated corn cobs	88.1%	10	2	6.5	-	Freundlich	Exothermic	(Parmar et al., 2006)
Calcium treated corn cobs	95.1%	10	2	6.5	-	Freundlich	Exothermic	(Parmar et al., 2006)
Cashew nut sheath	1.8	10	-	-	-	Freundlich	-	(Sivabalan et al., 2003)
Fly Ash	0.62	15	2	6.5	First	Langmuir	Endothermic	(Chaturvedi et al., 1990)
Granular red mud	0.851	5-150	9	2.5-7.3	Pseudo-second	Freundlich	-	(Tor, Danaoglu, Arslan, & Cengeloglu, 2009)

	Brick Powder	56.4%	1.21	1	6.0-8.0	First	Freundlich	-	(Yadav et al., 2006)
	Gas Concrete	86%	120	1	6.9-8.9		-	Endothermic	(Oguz, 2005)
	Hydrated Cement	2.7	5.9	24	6.7	Pseudo-first	Freundlich and Langmuir	-	(Kagne et al., 2008)
Conc.= Concentration									

## 2.4 3D PRINTING

Various techniques of 3D printing have their specific benefits and drawbacks which allow them more suitable for specific implementations than others. Fig 2.7 depicts the various 3D printing technologies presently applied for the fabrication of parts based on input material used. Table 2.3 defines the pros and cons along with the material used by the 3D printing technique (Low et al., 2017).

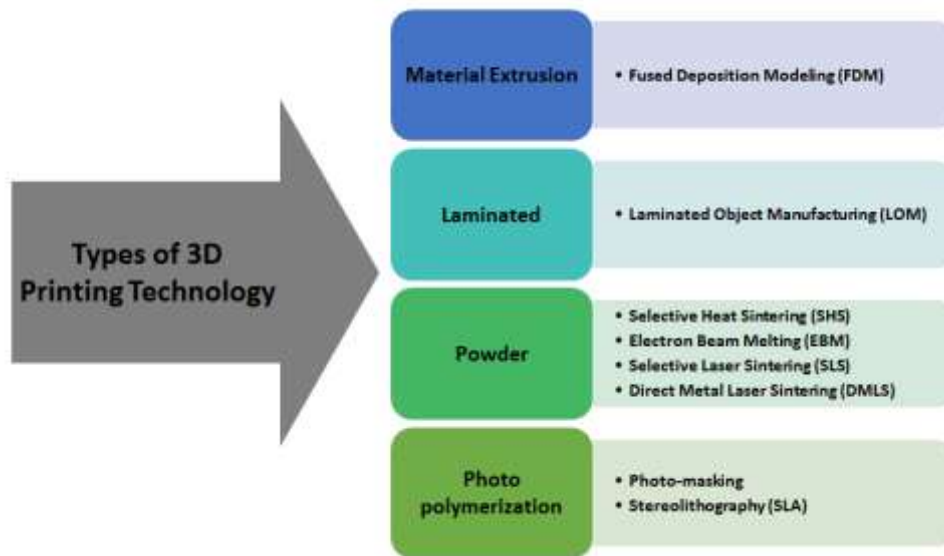


**Fig 2.7** Types of 3D printing technologies

In order to define the aptness of AM for device manufacturing, it is necessary to consider several key properties of the techniques (Fig 2.8).

The following characteristics are desired for part manufacturing:

- **Resolution:** wide dynamic range needed
- **Support:** smooth and massive support can be easily fixed or AM system where support is not needed
- **Speed:** usually as quick as probable to minimize production time
- **Cost:** efficient and preferable to fabricate
- **Material:** introduction of 3D printable materials that are compatible to comprise commonly used printing materials
- **Build size:** should be able to manufacture desired dimensions
- **Accuracy:** should be able to manufacture the portion as engineered, including the impact of pre-treatment and post-treatment moves

- **Mechanical property:** materials that can withstand high-pressure systems (1–40 bar) and a variety of solvents

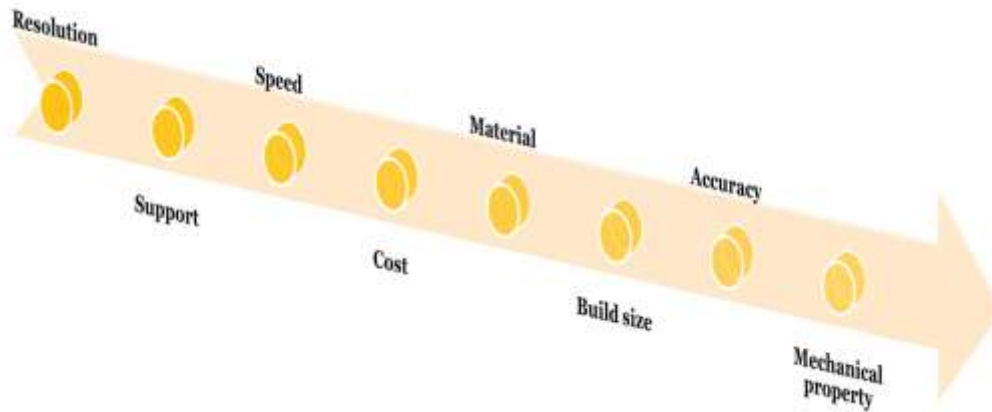


**Fig 2.8** 3D printing technology properties

**Table 2.3** Materials, pros, and cons of 3D printing techniques

Printing Technique	Material	Pros	Cons
<b>Material Extrusion</b>			
FDM/FFF	Thermoplastics, modeling clay, plasticine, metal clay, eutectic metals	<ul style="list-style-type: none"> <li>• Variety of materials</li> <li>• Desktop scale printer are available</li> <li>• Throughput are constant</li> </ul>	<ul style="list-style-type: none"> <li>• Support structures are required</li> <li>• In vertical direction the strength is reduced</li> <li>• Slower than laser printer</li> <li>• Appearance grainy type</li> </ul>
<b>Lamination</b>			
LOM	Paper, metal foil, plastic Film	<ul style="list-style-type: none"> <li>• Fast build</li> <li>• Relatively cheap</li> </ul>	<ul style="list-style-type: none"> <li>• Poor strength</li> <li>• Parts may absorb moisture</li> <li>• Post processing required for newly printed parts</li> </ul>
SDL	Paper	<ul style="list-style-type: none"> <li>• Full colour printing</li> <li>• Low cost print material</li> </ul>	<ul style="list-style-type: none"> <li>• Can print only standard paper</li> <li>• Parts may absorb moisture</li> </ul>

		<ul style="list-style-type: none"> <li>• Eco-friendly</li> </ul>	<ul style="list-style-type: none"> <li>• Noticeable stairsteeping on edges of parts</li> </ul>
<b>Powder</b>			
Binder jetting	Polymer, metals, alloys and ceramics	<ul style="list-style-type: none"> <li>• Short build time</li> <li>• Cheap</li> <li>• Does not employ heat</li> <li>• Parts can be printed in range of colors</li> </ul>	<ul style="list-style-type: none"> <li>• Limited mechanical properties</li> <li>• In overall processing a significant time is added due to postprocessing</li> <li>• Not always suitable for structural parts</li> </ul>
SLS/DMLS	Thermoplastic, metal powder, ceramic powder	<ul style="list-style-type: none"> <li>• Post curing not required (except for ceramics)</li> <li>• Support structures not required</li> </ul>	<ul style="list-style-type: none"> <li>• Surface are porous</li> <li>• Surface finishing is poor</li> <li>• Long time duration is required for heating and cooling</li> </ul>
<b>Photopolymerization</b>			
SLA	Photopolymers	<ul style="list-style-type: none"> <li>• Complex geometry printing</li> <li>• High accuracy</li> </ul>	<ul style="list-style-type: none"> <li>• Support structures are required</li> <li>• Resins are hazardous</li> <li>• Curable material limitation</li> <li>• Slower</li> </ul>

Experts have recently begun to look into 3D-printed material for applications in the membrane extraction and water treatment processes. This arises due to the world's water shortage problem, which requires a joint effort to achieve efficient solutions (Perrotta et al., 2017). Researchers have made various approaches which include membrane design products, materials for dye degradation and catalysis, solar absorbers/steam generation materials, sorbents for oil/water separation, etc. The design and production of module spacers using net-design spacer for membrane separation was the early

implementation of 3D printing (F. Li, Meindersma, De Haan, & Reith, 2005). There have also been reports of various membrane spacer design for implementations like reverse osmosis (RO), ultrafiltration (UF) (Sreedhar et al., 2018), membrane distillation (MD) (Thomas et al., 2019), forward osmosis (FO) (Yanar et al., 2018), and so on. Attempts have been made to directly manufacture 3D-printed polymeric membranes (Femmer, Kuehne, Torres-Rendon, Walther, & Wessling, 2015) and ceramic membranes (Hwa et al., 2018), or as membrane substrates (Al-Shimmery, Mazinani, Ji, Chew, & Mattia, 2019). However, direct 3D membrane printing is still a challenge due to resolution limitations.

Recent progress in more powerful 3D printers tackled a few of these drawbacks such as the ability to adapt to multi-materials. Several research groups documented increased performance in solar steam production using 3D-printed materials along with various other applications such as adsorption, water remediation, and wastewater treatment.

The main emphasis here is on the recent development and advancement of 3D printed materials. Discussions include layout, manufacturing techniques, and 3D-printed material performance in water-related implementations. It also included basic information on additive manufacturing, the components used, processes, and associated characteristics. Ultimately, it was found that for the fabrication of components based on the target applications, commonly used 3D printing technologies are FDM, SLS, and SLA.

## **2.5 3D PRINTED MATERIAL APPLICATIONS**

Below are several uses of 3D printed materials for improved water, desalination, potable water processing, water purification, and filtration, wastewater treatment.

### **2.5.1 SPACER**

Many applications of membrane separation, particularly using the SWM module (spiral wound membranes), spacers perform an important part in assuring fluid mixing, continuous flow, and recirculation (Da Costa, Fane, & Wiley, 1994). Spacers come in different designs which aim at maintaining

constant fluid space (mechanical support), increasing turbulence, fouling composition reduction, and avoiding damage to the active membrane layer (J.-Y. Lee et al., 2016). Fig 2.9 displays the schematic of how spacers are positioned in the structure and the relative spatial specifications for different parts of the membrane framework from membranes, spacers, and sizes of the module. Since the spacer has to be rolled up, it requires a balance of rigidity and durability, along with strong chemical tolerance, so traditionally industrial spacers are manufactured of polypropylene (PP) (Tan, Chua, Chong, Fane, & Jia, 2016). Better spacer layout is essential as dead zones generate particle deposition conditions which lead to fouling that also reduces the rate of mass transfer. Various spacer design with different characteristics was evaluated to restrict dead zones and to evaluate their impact on pressure drop, fouling and mass transfer (Da Costa, Fane, Fell, & Franken, 1991; Da Costa et al., 1994). However, with traditional methods such as moulding or vacuum foaming, heat extrusion, the intricate spacer architecture, and structure will pose manufacturing difficulties. Therefore, the promise of 3D printing in the manufacturing of complex-design spacers is recognized because of its capability to manufacture either basic or complex geometries.

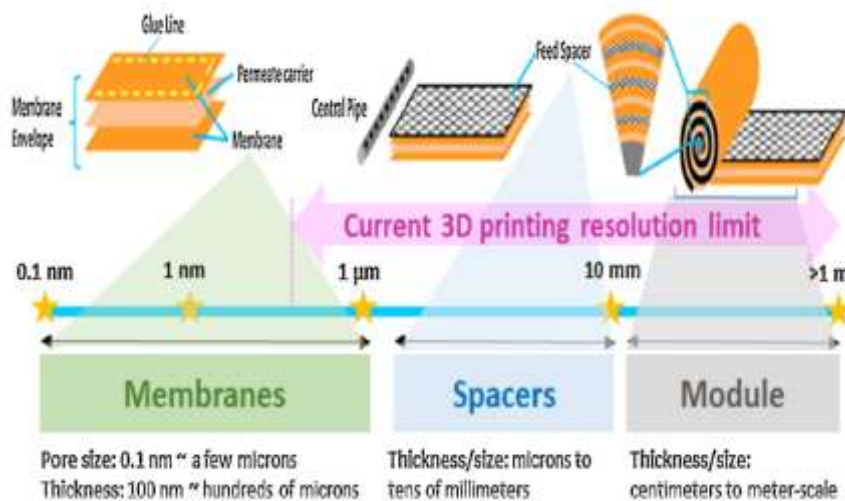


**Fig 2.9** Representation of spiral wound membrane module component with spacer and the dimensions for the parts of a membrane unit along with existing resolution restrictions of 3D printing (Tijing et al., 2020)



Li et al. (F. Li et al., 2005) carried out groundbreaking research on the manufacture of membrane spacers using 3D printing 14 years ago and the spacers were manufactured using SLS technology. The authors not only introduced novel spacers, but also the layout of the spacers that focused on enhancing mass transfer in the spacer-filled channels. Tan et al. (Tan et al., 2016), Thomas et al. (Thomas et al., 2018), and Sreedhar et al. (Sreedhar et al., 2018) studied the application of SLS technology for spacer manufacturing.

Tan et al. (Tan et al., 2016), using the SLS process, designed a net-type spacer that was made from polypropylene (PP). In 3D printing the PP spacer, they evaluated the temperature and process dimensions of the optimum build. The printing accuracy and the mechanical properties of the 3D printed part have been assessed. Findings showed that the energy density used (laser power, scanning distance, and scanning speed) were relative to Young's modulus and the overall tensile ability. In other terms, the higher the energy density then higher is Young's modulus and final tensile strength of the printed component. However, the precision of the measurements was found to correlate with Young's PP content module.

The outcome of triply periodic minimal surface (TPMS) topologies on the performance of spacers developed using SLS printing technology was studied by Thomas et al (Thomas et al., 2018). Owing to their interpenetrating arrangements these spacers were used for the membrane distillation and showed to improve the overall thermal transfer coefficient compared to existing spacers (Thomas et al., 2018). In research targeted at reducing the bio-fouling during brackish water reverse osmosis (BWRO) and ultrafiltration, Sreedhar et al. (Sreedhar et al., 2018) used the same spacers. Compared to existing spacers, the deposition of bio-foulants on the 3D printed spacers and membrane has been slashed (Sreedhar et al., 2018).

Kerdi et al. (Kerdi, Qamar, Vrouwenvelder, & Ghaffour, 2018) used the DLP 3D printer for the manufacturing of symmetric perforated spacer designs such as 1-hole, 2-hole, and 3-hole and also evaluated their hydrodynamic output and ultrafiltration test filtration capacity. For enhancing the interpretation of their efficiency and function a direct numerical simulation was conducted. They proposed that, by minimizing fouling, the perforations in the new design

would raise shear stress at the membrane surface there, while at the same time reducing net pressure in the module. Due to the presence of micro-jets as caused by the perforations by removing dead zones, the perforated 3D printed membranes showed better filtration efficiency compared to non-perforated ones under ultrafiltration tests. The 1-hole spacer achieved the best results among all prototypes, displaying 75 per cent (under consistent pressure) and 23 per cent (under consistent flow) increases in permeate flux, and also had the cleanest surface of the membrane (less fouling). The 3-hole spacer displayed a high-pressure drop decrease (54 per cent) but didn't translate into improved permeation flux. An increase in the number of perforations has also culminated in further fouling due to decreased water flow uncertainty. Ultimately, the three separate perforated structures culminated in such a thinner fouling formation relative to 0-hole spacers. It was concluded that the optimum spacer design was the 1-hole spacer based on this study's conditions. Similarly, Ali et al. (Ali et al., 2019) used DLP for printing column patterns on their spacer. In their architecture, they tried to improve the clearance between filament and membrane while retaining the same thickness of the flow channel. To serve as vortex shading devices, the column style nodes were introduced. The numerical analysis revealed a lesser drop in pressure using their 3D printed spacer, along with lesser dead zones as demonstrated by the results of their experiments. The 3D-printed spacer with column configuration received two orders of magnitude lower specific energy usage than the medium spacer in comparison to the standard existing spacer.

Fused deposition modeling printing was used by Shrivastava et al. (Shrivastava, Kumar, & Cussler, 2008) to print novel spacer designs, like helices, herringbones, and also ladder-like design. They built spacers for a non-net stream. Their primary concern was to measure the impact of spacer shapes on the polarization of concentration and to utilize this influence to enhance the RO cycle. This was achieved when the 3D printed spacers have shown a mass transfer improvement better than existing spacers. In the following order the mass transition was increased: laddered spacers, helical spacers, and herringbone spacers (Shrivastava et al., 2008).

The experiment performed on membrane fouling simulator (MFS) by Siddiqui et al. (Siddiqui et al., 2016) derived that 3D printed spacers can enhance hydrodynamics and minimize bio-fouling. A correlation was first produced between a 3D spacer designed by Polyjet and a traditional one with the same design. There was an equal deposition of biomass, hydrodynamic activity and a decrease in pressure. Numerical analysis was utilized to develop a revised spacer layout which resulted in low-pressure decrease with respect to time and less deposition of biomass. They stated that numerical modelling including experimental screening of printed spacers using 3D printing can be a successful technique for manufacturing improved spacers that can increase the efficiency of the membrane. They also made a very quick distinction of spacers produced using 3D printing techniques from FDM, Polyjet, and SLA. FDM and SLA both considered being inadequate for spacer printing since FDM created brittle spacers with thicker strands than the design expected, whereas SLA generated spacers with low material inflexibility and mechanical stability than necessary. On the other side, as the spacers designed by this process had higher resolution and low cost than spacers designed with other 3D printed methods, Polyjet printing of spacers was observed to be encouraging.

### **2.5.2 MEMBRANE**

Membrane technology is developing rapidly, and because of its better efficiency and cost-effectiveness, it has substituted several traditional water treatment processes (Werber, Osuji, & Elimelech, 2016; Ying et al., 2017). Most of the membranes utilized are made up of polymers but they also utilized ceramic membranes. Traditional methods for the manufacture of polymeric membranes involve phase inversion (Woo et al., 2018), hollow fiber spinning (Yao et al., 2019), stretching, and extrusion. A lot of research has been done on the method of electrospinning for multiple applications of desalination and water treatment (Tijing, Choi, Lee, Kim, & Shon, 2014) (Tijing et al., 2016; Yao et al., 2016). For membrane manufacturing the ability of 3D printing to specifically manufacture hierarchical structures and scale is encouraging. Nonetheless, 3D printing is not yet commonly explored

for specific polymeric membrane production due to the resolution and material limit (J.-Y. Lee et al., 2016). Many accessible 3D printers are still not capable of printing effectively below submicron size, while membrane pores are normally within that limit. Furthermore, some membrane systems require different types of material properties and wettability (hydrophilic or hydrophobic), making it a difficulty because existing 3D printers are restricted to their relevant / printable materials. Nonetheless, several research teams have begun to show the ability of 3D printing for membrane related processing, typically in the form of plastic material, i.e. 3D manufacturing utilized for the matrix, as well as other active layer manufacturing techniques.

3D printing is commonly utilized for spacer manufacturing than in membrane manufacturing according to Tan et al. (Tan et al., 2016). Because the resolution limitations of 3D printing technologies being utilized for direct membrane printing are not yet developed. Fig 2.10 Shows the resolution range whereby 3D printing techniques will reach.

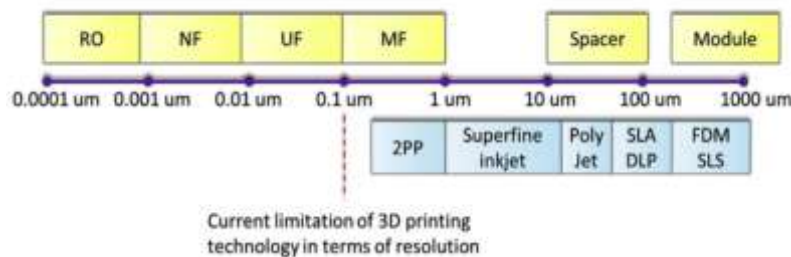


**Fig 2.10** Existing constraint in the resolution of 3D printing technology when applied for membrane research (Balogun, Sulaiman, Marzouk, Giwa, & Hasan, 2019)

Obviously, it only aligns with both the resolution spectrum of membrane processing at 0.1–10 micrometers, this suggests a limit on the use of 3D printing for the printing of large-porous membranes, such as MF membranes, mostly. Until reverse osmosis (RO), nanofiltration (NF), and ultrafiltration (UF) membranes can be easily 3D printed (J.-Y. Lee et al., 2016), there is indeed a lot ahead.

The reliability and anti-fouling nature of a composite membrane fabricated of an ABS material (with flat and wavy surface systems) using a multijet printer

and a thin polyethersulfone (PES) selective layer were studied by Shimerry et al. (Al-Shimerry et al., 2019). PES surface was cast through phase inversion over the support layer. Fig 2.11 displays the production schematics and the photographic and SEM pictures of their composite membranes.

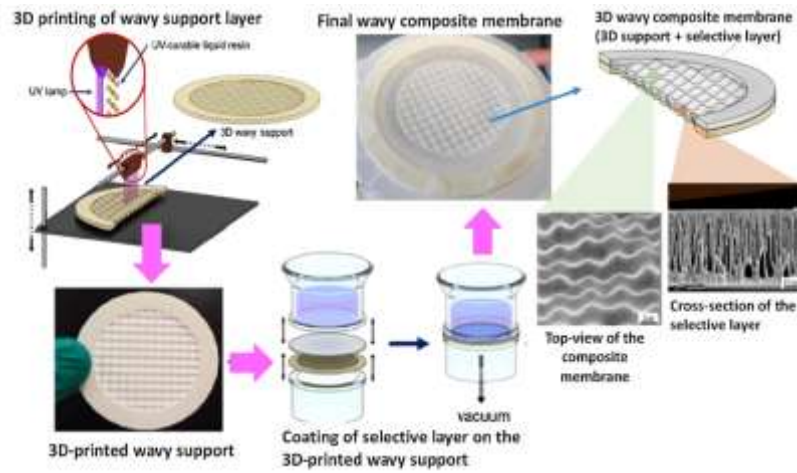


**Fig 2.11** Composite membrane schematics: 3D printing of wavy design support layer was performed while the selective layer at the top was the first cast by the non-solvent induced phase separation (NIPS) and then the casted membrane is attached by vacuum filtration to the 3D-printed support (Tijing et al., 2020)

Ultrafiltration tests were carried out by the authors to examine the efficiency of the manufactured membrane focused on its oil rejection, anti-fouling, and permeation actions. Fouling, since that is the accumulation of undesirable particles on/in the membranes and it is a serious challenge with all processes of membrane separation, as it limits a membrane's effectiveness, functionality, and life (Tijing et al., 2015).

Yuan et al. (Yuan et al., 2019) designed a 3D printed polyamide (PA) membrane substratum (SLS) painted ZIF-L including superhydrophobic as well as superoleophobic surfaces underwater. The composite membrane was prepared in two phases. One was the development of two forms of separate ZIF-L particles, while others were the formation of the ZIF-Ls on the PA substrate designed in 3D. This results in a splitting capacity of over 99 per cent and also an oil flux of 24,000 LMH (Liter per square meter per hour) after adding the 3D printed composite membrane in oil-water splitting.

Although the scope of 3D membrane printing techniques is probably limited, several investigators have begun to explore its use for multiple applications, including the manufacture of ion-exchange membranes used for the electro dialysis, biomedical and microfluidic usage (Seo, Kushner, & Hickner, 2016). Nano Sun, a university-based company, has commercialized a multi-use membrane produced by 3D printing technology which is used in industrial applications of desalination, wastewater treatment, food as well as beverage. Ion-selective membranes were identified in the desalination process for separation of dissolved ions from brackish water (El-Dessouky-HT, 2002; Liping Li, Wei, Wei, & Du, 2013). Patterned membranes attract future scientists because they are assumed to boost the transport of ions as well as mitigate fouling. The anion exchange membrane was developed using the photolithographic technique (Seo et al., 2016). The patterned 3D-printed membranes, used for the electro dialysis as anion exchange membrane, established lower resistance than unpatterned membranes. Among the most wanted characteristics of ion exchange membranes is low resistance.

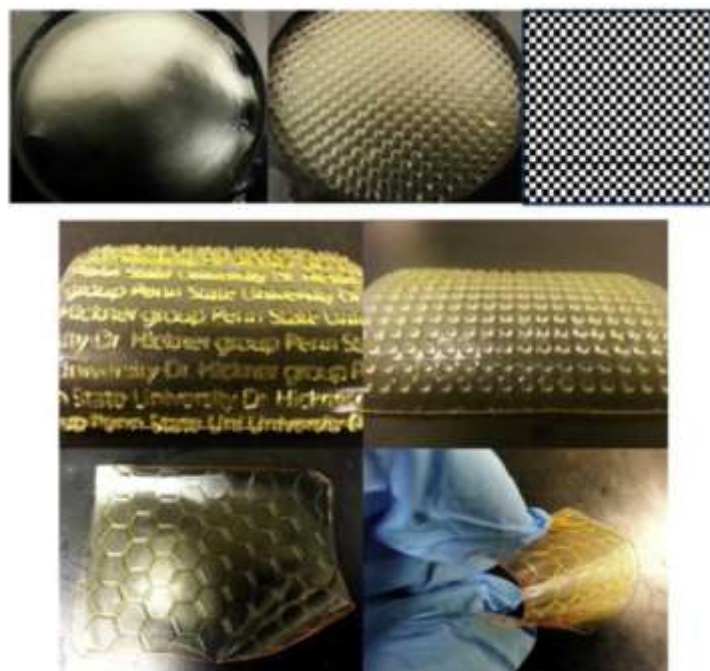


**Fig 2.12** Top shows flat and patterned membranes along with pattern schematic and Bottom shows an example of patterned membranes (Balogun et al., 2019)

One of the maximum desirable features of ion exchange membranes is reduced resistance. Furthermore, the patterns extended the life of the membrane transport and polarization of the concentration. Examples of the patterned membranes manufactured in 3D are shown in Fig 2.12.

Microbial desalination cell (MDC) is an evolving desalination technology that integrates ion exchange membranes which is hybrid of microbial fuel cell technology along with electrodialysis to remove the salt dissolved in seawater and brackish water (Sophia, Bhalambaal, Lima, & Thirunavoukkarasu, 2016) (Akther et al., 2015). The production of additive layers used by You et al. (You, Preen, Bull, Greenman, & Ieropoulos, 2017) may be applied for manufacturing MDC membranes as well as an anode in a cell for the desalination membranes. Therefore, in addition to being utilized in the manufacture of membranes, 3D printing is applicable for designing all MDC components such as ion exchange membranes and electrodes with enhanced anode energy generation in comparison to conventional materials.

In recent times the polymer membranes used for desalination processing are constructed by PA composites (Fridman-Bishop & Freger, 2017). 3D printing technology could be utilized for manufacturing a thin active film using a highly selective PA aromatic layer (Ren & McCutcheon, 2017). The introduction of 3D printing had already made it easier for the in-situ development of this active PA film onto the porous supportive membrane to have a controllable thickness, roughness, and independence. It is a major achievement in the reverse osmosis (RO) sector as it is possible to adjust the membrane permeability, the fouling tendency right from the membrane module configuration, thereby efficiency of the RO process (Ren & McCutcheon, 2017). Similar to others, the 3D printed aromatic PA has been considered superior since it can be processed with a very low thickness that has high performance in water flux and permeability. Spongy-like polymer often possesses high density and rigidity that promotes fast salt resistance more than traditional RO production films (Fridman-Bishop & Freger, 2017). Badalov et al. (Badalov, Oren, & Arnusch, 2015) used the Inkjet printing technique of composite film printing (Amine monomer) on the surfaces of the UF membranes. The membranes illustrated improved ion/compound isolation,

and the manufacturing process was concluded to be extra eco friendly because the pollution was significantly reduced through 3D printing (Giwa, Alabi, Yusuf, & Olukan, 2017).

Rapid and continuous developments in 3D printing technology in membrane systems would expand its ability. If the resolution, speed, and materials used during 3D printing are sufficiently advanced and optimized, membrane module design is intended as one of its influential desalination and water treatment applications (J.-Y. Lee et al., 2016). The use of renewable energy to produce 3D printed materials might also render the manufacturing process more environmentally friendly (Giwa et al., 2017) (Giwa, 2017; Giwa et al., 2018).

### **2.5.3. ADSORBENT**

Elimination of toxic heavy metals from water such as copper, arsenic, cadmium, and mercury acknowledged significant publicity. Such toxic metals have a significant adverse impact on human health via aggregation over living organisms (Y. Hu et al., 2013; D. Zhang, Xiao, Guo, & Yang, 2019). Consequently, a reliable and effective process of extracting such toxic metals is important for public safety. The removal of heavy metals has been attained using various adsorbents such as bio-inspired materials, activated carbon, CNTs, and other porous carbon materials. The advantages of using bio-inspired materials are low-cost, effectiveness, and biodegradability (Appuhamillage et al., 2019; D. Zhang et al., 2019). 3D printing addresses challenges by creating 3D objects with a transparent nature and a wide surface area, and possible reusability. For example, Zhang et al. designed bio-adsorbent filter composed of a monolithic 3D porous chitosan composite using a 3D printing technique based on stereolithography, and applied it to remove Cu (D. Zhang et al., 2019). Several structures such as closely organized hexagonal holes, square holes, hexagonal skewed holes, and round holes were designed. Fig 2.13 (a) shows the composite of skewed hexagonal holes that have emerged as the most efficient, high-adsorption design. An adsorption-desorption study with aqueous ethylenediaminetetraacetic acid (EDTA) solution as eluent was examined on reusability. Approximately 92 per cent



desorption efficiency was reached and throughout the cycle the value remained constant demonstrating its reusability. Investigators limited the elimination of Cu (II) in their applications. The implementation of 3D printing has been extended beyond to produce materials with such a distinctive shape. For example, hydrogel materials (Fig 2.13 (b)) were termed to be heavy metal adsorbents due to their benefits of having a large surface area having a porous structure. Extrusion, a 3D printing process was used to manufacture 3D hydrogel frameworks for the elimination of heavy metal ions ( $\text{Cu}^{2+}$ ,  $\text{Cd}^{2+}$ ,  $\text{Hg}^{2+}$ ,  $\text{Pb}^{2+}$ ) (Appuhamillage et al., 2019). The hydrogel was formulated by combining Pluronic F-127 (F127-DA) with chitosan and diacrylate at different proportions. Findings indicate that chitosan printability decreases as chitosan concentration higher.

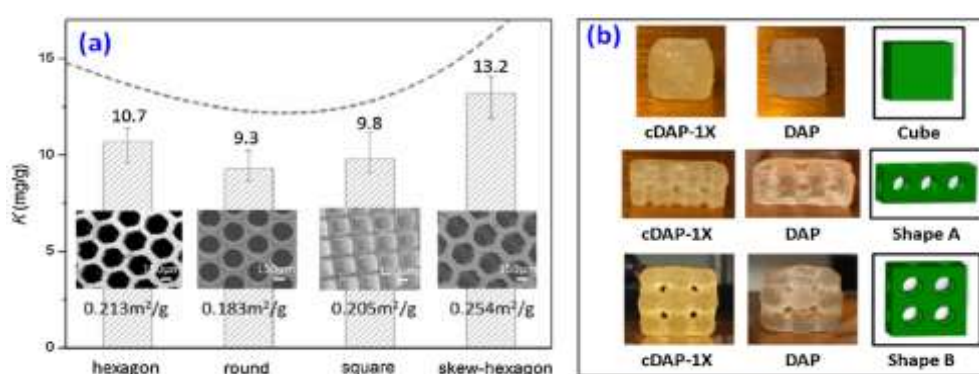


**Fig 2.13** (a) Adsorption capacity comparison of Cu (II) for 3D printed chitosan filters of various structures ( $T= 25^{\circ}\text{C}$  and  $\text{pH } 5.5$ ) (b) 3D printed hydrogels for heavy metal removal (Tijing et al., 2020)

3D printing creates an interesting avenue to develop materials in different shapes and forms with ease of preparation whether it is like hydrogels, filters, sorbents, etc. irrespective of the complexity of the design. The hydrogel is made from structural features that adsorb up to 95 per cent of metals in 30 minutes. The specific surface area of an adsorbent is an important parameter during the adsorption process, so it is definitely an advantage for such an application to allow specific design and fabrication of internal structure using 3D printing technique. 3D printing is indeed a "greener" solution for manufacturing chitosan-based adsorbent for heavy metal removal. It is easy to

print directly 3D chitosan (through the SLS) mixed with thermoplastic polyurethane (TPU) for a solvent-less membrane manufacturing technique (Sun, Zhang, & Tao, 2019), instead of utilizing huge amount of solvents as well as acids/bases for chitosan production. The membrane adsorbed Cu(II) and Pb(II) efficiently.

Owing to the capability of hydrogel to react rapidly with external stimuli through reversible volume adjustments (a 4D printing) chitosan hydrogels have been progressively tested utilizing 3D printing over the last years. 3D printing will either be utilized to print the adsorbent material directly, to print the substrate for which it is controlled with adsorptive effects, and to print the prototype for which the adsorbent material is formed. Most of this allows accurate 3D printing of several geometrical structures and systems through modern manufacturing methods which were difficult to manufacture the structures using traditional fabrication methods. It is also a good strategy to build composite 3D printed material with heavy metal bonding capabilities, but problems with nanofiller content are also a concern particularly when thermoplastic polymers are used (Valino et al., 2019). The nanofillers can cause invalid creation thus influencing actual mechanical stability of the 3D printed system.

## **2.6 CONCLUSION**

Here the extensive literature survey was performed to study the fluoride removal techniques and various nanoadsorbents used. The survey on adsorbents shown that the various forms of metal oxide and agricultural waste based adsorbents have better potential for the removal of fluoride from water. Due to which in this study three types of adsorbents have been studied such as hematite, titanium dioxide and activated carbon. Amongst various used processes, adsorption technology appears to be arguably one of the most versatile of all the defluoridation techniques due to a number of reasons such as cost, diverse end-uses, socio-cultural acceptance, regulatory compliance, environmental benignity, and simplicity. Further, the advances observed in the field of 3D printing and its application. The SLA technique seems to be the most effective and efficient manufacturing process for complex designs and

dimensions as per the applicability in the domain of water filtration. There are many techniques established and also research work is under process on how to remove fluoride from water or to maintain the level fluoride which won't affect human health. Technologies that are being used to remove fluoride are very much costly because of which cost of drinking water is gradually increasing. So in order to attain the all required requirement, there is a need for developing a system which can remove fluoride in respect to costing, durability, and robust. In this research various adsorbents such as magnetic, metal oxide, and carbon-based were explored, and additionally, the polymer-based resin was used for the fabrication of microchannels for the loading of synthesized adsorbents and further investigation was performed for analyzing the removal efficiency of fluoride from water.

## **2.7 REFERENCES**

- Akther, N., Sodiq, A., Giwa, A., Daer, S., Arafat, H., & Hasan, S. (2015). Recent advancements in forward osmosis desalination: a review. *Chemical Engineering Journal*, 281, 502-522.
- Al-Shimmery, A., Mazinani, S., Ji, J., Chew, Y. J., & Mattia, D. (2019). 3D printed composite membranes with enhanced anti-fouling behaviour. *Journal of membrane science*, 574, 76-85.
- Alarcón-Herrera, M. T., Bundschuh, J., Nath, B., Nicolli, H. B., Gutierrez, M., Reyes-Gomez, V. M., Sracek, O. (2013). Co-occurrence of arsenic and fluoride in groundwater of semi-arid regions in Latin America: Genesis, mobility and remediation. *Journal of Hazardous Materials*, 262, 960-969.
- Aldaco, R., Garea, A., & Irabien, A. (2007). Modeling of particle growth: Application to water treatment in a fluidized bed reactor. *Chemical Engineering Journal*, 134(1-3), 66-71.
- Ali, S. M., Qamar, A., Kerdi, S., Phuntsho, S., Vrouwenvelder, J. S., Ghaffour, N., & Shon, H. K. (2019). Energy efficient 3D printed column type feed spacer for membrane filtration. *Water research*, 164, 114961.

- Alvarez-Gallegos, A., & Pletcher, D. (1999). The removal of low level organics via hydrogen peroxide formed in a reticulated vitreous carbon cathode cell. Part 2: The removal of phenols and related compounds from aqueous effluents. *Electrochimica Acta*, 44(14), 2483-2492.
- Appuhamillage, G. A., Berry, D. R., Benjamin, C. E., Luzuriaga, M. A., Reagan, J. C., Gassensmith, J. J., & Smaldone, R. A. (2019). A biopolymer-based 3D printable hydrogel for toxic metal adsorption from water. *Polymer International*, 68(5), 964-971.
- Babaeiveli, K., & Khodadoust, A. P. (2013). Adsorption of fluoride onto crystalline titanium dioxide: Effect of pH, ionic strength, and co-existing ions. *Journal of colloid and interface science*, 394, 419-427.
- Badalov, S., Oren, Y., & Arnusch, C. J. (2015). Ink-jet printing assisted fabrication of patterned thin film composite membranes. *Journal of membrane science*, 493, 508-514.
- Balogun, H. A., Sulaiman, R., Marzouk, S. S., Giwa, A., & Hasan, S. W. (2019). 3D printing and surface imprinting technologies for water treatment: A review. *Journal of Water Process Engineering*, 31, 100786.
- Bansiwal, A., Pillewan, P., Biniwale, R. B., & Rayalu, S. S. (2010). Copper oxide incorporated mesoporous alumina for defluoridation of drinking water. *Microporous and Mesoporous Materials*, 129(1), 54-61.
- Behbahani, M., Moghaddam, M. A., & Arami, M. (2011). Techno-economical evaluation of fluoride removal by electrocoagulation process: Optimization through response surface methodology. *Desalination*, 271(1), 209-218.
- Bhatnagar, A., Kumar, E., & Sillanpää, M. (2011). Fluoride removal from water by adsorption—a review. *Chemical Engineering Journal*, 171(3), 811-840.
- Bi, S., Wang, C., Cao, Q., & Zhang, C. (2004). Studies on the mechanism of hydrolysis and polymerization of aluminum salts in aqueous solution: correlations between the “Core-links” model and “Cage-like” Keggin-Al13 model. *Coordination Chemistry Reviews*, 248(5-6), 441-455.

- Borah, L., & Dey, N. (2009). Removal of fluoride from low TDS water using low grade coal.
- Chaturvedi, A., Yadava, K., Pathak, K., & Singh, V. (1990). Defluoridation of water by adsorption on fly ash. *Water, Air, & Soil Pollution*, 49(1), 51-61.
- Chauhan, V. S., Dwivedi, P. K., & Iyengar, L. (2007). Investigations on activated alumina based domestic defluoridation units. *Journal of Hazardous Materials*, 139(1), 103-107.
- Chen, L., He, B.-Y., He, S., Wang, T.-J., Su, C.-L., & Jin, Y. (2012). Fe—Ti oxide nano-adsorbent synthesized by co-precipitation for fluoride removal from drinking water and its adsorption mechanism. *Powder technology*, 227, 3-8.
- Chen, L., He, S., He, B.-Y., Wang, T.-J., Su, C.-L., Zhang, C., & Jin, Y. (2012). Synthesis of iron-doped titanium oxide nanoadsorbent and its adsorption characteristics for fluoride in drinking water. *Industrial & Engineering Chemistry Research*, 51(40), 13150-13156.
- Da Costa, A., Fane, A., Fell, C., & Franken, A. (1991). Optimal channel spacer design for ultrafiltration. *Journal of membrane science*, 62(3), 275-291.
- Da Costa, A., Fane, A., & Wiley, D. (1994). Spacer characterization and pressure drop modelling in spacer-filled channels for ultrafiltration. *Journal of membrane science*, 87(1-2), 79-98.
- Dahi, E. (1996). *Contact precipitation for defluoridation of water [Discussion paper]*. Paper presented at the Reaching the unreached-Challenges for the 21st century: Proceedings of the 22nd WEDC International Conference, New Delhi, India.
- Dubey, S., Agarwal, M., & Gupta, A. (2018). Experimental investigation of Al-F species formation and transformation during coagulation for fluoride removal using alum and PACl. *Journal of Molecular Liquids*, 266, 349-360.
- El-Dessouky-HT, E.-H. (2002). Fundamentals of Salt Water. *Desalination*.

- Elazhar, F., Tahaikt, M., Achatei, A., Elmidaoui, F., Taky, M., El Hannouni, F., . . . Elmidaoui, A. (2009). Economical evaluation of the fluoride removal by nanofiltration. *Desalination*, 249(1), 154-157.
- Etzel, J. E., & Wachinski, A. M. (1997). Environmental Ion Exchange: Principles and Design. In: Boca Raton, Florida: CRC Press LLC.
- Fan, X., Parker, D., & Smith, M. (2003). Adsorption kinetics of fluoride on low cost materials. *Water Research*, 37(20), 4929-4937.
- Femmer, T., Kuehne, A. J., Torres-Rendon, J., Walther, A., & Wessling, M. (2015). Print your membrane: Rapid prototyping of complex 3D-PDMS membranes via a sacrificial resist. *Journal of membrane science*, 478, 12-18.
- Fridman-Bishop, N., & Freger, V. (2017). What makes aromatic polyamide membranes superior: New insights into ion transport and membrane structure. *Journal of membrane science*, 540, 120-128.
- Gan, Y., Wang, X., Zhang, L., Wu, B., Zhang, G., & Zhang, S. (2019). Coagulation removal of fluoride by zirconium tetrachloride: Performance evaluation and mechanism analysis. *Chemosphere*, 218, 860-868.
- George, S., Pandit, P., & Gupta, A. (2010). Residual aluminium in water defluoridated using activated alumina adsorption—Modeling and simulation studies. *Water research*, 44(10), 3055-3064.
- Ghorai, S., & Pant, K. (2005). Equilibrium, kinetics and breakthrough studies for adsorption of fluoride on activated alumina. *Separation and purification technology*, 42(3), 265-271.
- Ghosh, D., Medhi, C., & Purkait, M. (2008). Treatment of fluoride containing drinking water by electrocoagulation using monopolar and bipolar electrode connections. *Chemosphere*, 73(9), 1393-1400.
- Giwa, A. (2017). Comparative cradle-to-grave life cycle assessment of biogas production from marine algae and cattle manure biorefineries. *Bioresource technology*, 244, 1470-1479.
- Giwa, A., Adeyemi, I., Dindi, A., Lopez, C. G.-B., Lopresto, C. G., Curcio, S., & Chakraborty, S. (2018). Techno-economic assessment of the sustainability of an integrated biorefinery from microalgae and

- Jatropha: a review and case study. *Renewable and Sustainable Energy Reviews*, 88, 239-257.
- Giwa, A., Alabi, A., Yusuf, A., & Olukan, T. (2017). A comprehensive review on biomass and solar energy for sustainable energy generation in Nigeria. *Renewable and Sustainable Energy Reviews*, 69, 620-641.
- Golder, A., Hridaya, N., Samanta, A., & Ray, S. (2005). Electrocoagulation of methylene blue and eosin yellowish using mild steel electrodes. *Journal of hazardous materials*, 127(1-3), 134-140.
- Gong, W.-X., Qu, J.-H., Liu, R.-P., & Lan, H.-C. (2012). Effect of aluminum fluoride complexation on fluoride removal by coagulation. *Colloids and Surfaces A: Physicochemical and Engineering Aspects*, 395, 88-93.
- Hamamoto, S., & Kishimoto, N. (2017). Characteristics of fluoride adsorption onto aluminium (III) and iron (III) hydroxide flocs. *Separation Science and Technology*, 52(1), 42-50.
- Helfferich, F. G. (1995). *Ion exchange*: Courier Corporation.
- Hu, K., & Dickson, J. M. (2006). Nanofiltration membrane performance on fluoride removal from water. *Journal of membrane science*, 279(1-2), 529-538.
- Hu, Y., Liu, X., Bai, J., Shih, K., Zeng, E. Y., & Cheng, H. (2013). Assessing heavy metal pollution in the surface soils of a region that had undergone three decades of intense industrialization and urbanization. *Environmental Science and Pollution Research*, 20(9), 6150-6159.
- Hwa, L. C., Uday, M., Ahmad, N., Noor, A. M., Rajoo, S., & Zakaria, K. B. (2018). Integration and fabrication of the cheap ceramic membrane through 3D printing technology. *Materials Today Communications*, 15, 134-142.
- Ishihara, T., Shuto, Y., Ueshima, S., Ngee, H. L., Nishiguchi, H., & Takita, Y. (2002). Titanium hydroxide as a new inorganic fluoride ion exchanger. *Journal of the Ceramic Society of Japan*, 110(1285), 801-803.
- Islam, M., & Patel, R. (2007). Evaluation of removal efficiency of fluoride from aqueous solution using quick lime. *Journal of Hazardous Materials*, 143(1), 303-310.

- Jain, S., & Jayaram, R. V. (2009). Removal of fluoride from contaminated drinking water using unmodified and aluminium hydroxide impregnated blue lime stone waste. *Separation Science and Technology*, 44(6), 1436-1451.
- Jayarathna, L., Bandara, A., Ng, W., & Weerasooriya, R. (2015). Fluoride adsorption on  $\gamma$ -Fe<sub>2</sub>O<sub>3</sub> nanoparticles. *Journal of Environmental Health Science and Engineering*, 13(1), 54.
- Kagne, S., Jagtap, S., Dhawade, P., Kamble, S., Devotta, S., & Rayalu, S. (2008). Hydrated cement: a promising adsorbent for the removal of fluoride from aqueous solution. *Journal of Hazardous Materials*, 154(1), 88-95.
- Karthikeyan, G., Pius, A., & Alagumuthu, G. (2005). Fluoride adsorption studies of montmorillonite clay.
- Kerdi, S., Qamar, A., Vrouwenvelder, J. S., & Ghaffour, N. (2018). Fouling resilient perforated feed spacers for membrane filtration. *Water research*, 140, 211-219.
- Ku, Y., & Chiou, H.-M. (2002). The adsorption of fluoride ion from aqueous solution by activated alumina. *Water, Air, & Soil Pollution*, 133(1), 349-361.
- Kuang, L., Liu, Y., Fu, D., & Zhao, Y. (2017). FeOOH-graphene oxide nanocomposites for fluoride removal from water: Acetate mediated nano FeOOH growth and adsorption mechanism. *Journal of colloid and interface science*, 490, 259-269.
- Lata, S., & Samadder, S. (2016). Removal of arsenic from water using nano adsorbents and challenges: a review. *Journal of Environmental Management*, 166, 387-406.
- Lee, G., Chen, C., Yang, S.-T., & Ahn, W.-S. (2010). Enhanced adsorptive removal of fluoride using mesoporous alumina. *Microporous and Mesoporous Materials*, 127(1), 152-156.
- Lee, J.-Y., Tan, W. S., An, J., Chua, C. K., Tang, C. Y., Fane, A. G., & Chong, T. H. (2016). The potential to enhance membrane module design with 3D printing technology. *Journal of membrane science*, 499, 480-490.



- Li, F., Meindersma, W., De Haan, A., & Reith, T. (2005). Novel spacers for mass transfer enhancement in membrane separations. *Journal of membrane science*, 253(1-2), 1-12.
- Li, L., Wei, D., Wei, G., & Du, Y. (2013). Transformation of cefazolin during chlorination process: Products, mechanism and genotoxicity assessment. *Journal of hazardous materials*, 262, 48-54.
- Li, L., Zhu, Q., Man, K., & Xing, Z. (2017). Fluoride removal from liquid phase by Fe-Al-La trimetal hydroxides adsorbent prepared by iron and aluminum leaching from red mud. *Journal of Molecular Liquids*, 237, 164-172.
- Li, Y.-H., Wang, S., Cao, A., Zhao, D., Zhang, X., Xu, C., Wu, D. (2001). Adsorption of fluoride from water by amorphous alumina supported on carbon nanotubes. *Chemical Physics Letters*, 350(5-6), 412-416.
- Li, Y.-H., Wang, S., Zhang, X., Wei, J., Xu, C., Luan, Z., & Wu, D. (2003). Adsorption of fluoride from water by aligned carbon nanotubes. *Materials Research Bulletin*, 38(3), 469-476.
- Liang, S., Xue, Y., Gao, B., & Yang, K. (2017). Removal of fluoride from aqueous solution by TiO<sub>2</sub>-based composites. *Journal of the Taiwan Institute of Chemical Engineers*, 74, 205-210.
- Linares-Hernández, I., Barrera-Díaz, C., Roa-Morales, G., Bilyeu, B., & Ureña-Núñez, F. (2007). A combined electrocoagulation–sorption process applied to mixed industrial wastewater. *Journal of hazardous materials*, 144(1-2), 240-248.
- Liu, L., Cui, Z., Ma, Q., Cui, W., & Zhang, X. (2016). One-step synthesis of magnetic iron–aluminum oxide/graphene oxide nanoparticles as a selective adsorbent for fluoride removal from aqueous solution. *RSC Advances*, 6(13), 10783-10791.
- López-Guzmán, M., Alarcón-Herrera, M., Irigoyen-Campuzano, J., Torres-Castañón, L., & Reynoso-Cuevas, L. (2019). Simultaneous removal of fluoride and arsenic from well water by electrocoagulation. *Science of the Total Environment*, 678, 181-187.
- Low, Z.-X., Chua, Y. T., Ray, B. M., Mattia, D., Metcalfe, I. S., & Patterson, D. A. (2017). Perspective on 3D printing of separation membranes and

- comparison to related unconventional fabrication techniques. *Journal of membrane science*, 523, 596-613.
- Luo, F., & Inoue, K. (2004). The Removal of Fluoride Ion by Using Metal (III)-Loaded Amberlite Resins. *Solvent extraction and ion exchange*, 22(2), 305-322.
- Malaisamy, R., Talla-Nwafo, A., & Jones, K. L. (2011). Polyelectrolyte modification of nanofiltration membrane for selective removal of monovalent anions. *Separation and purification technology*, 77(3), 367-374.
- Maliyekkal, S. M., Shukla, S., Philip, L., & Nambi, I. M. (2008). Enhanced fluoride removal from drinking water by magnesia-amended activated alumina granules. *Chemical Engineering Journal*, 140(1), 183-192.
- Markovski, J., Garcia, J., Hristovski, K. D., & Westerhoff, P. (2017). Nano-enabling of strong-base ion-exchange media via a room-temperature aluminum (hydr) oxide synthesis method to simultaneously remove nitrate and fluoride. *Science of the Total Environment*, 599, 1848-1855.
- Meenakshi, S., & Viswanathan, N. (2007). Identification of selective ion-exchange resin for fluoride sorption. *Journal of colloid and interface science*, 308(2), 438-450.
- Mena, V., Betancor-Abreu, A., González, S., Delgado, S., Souto, R., & Santana, J. (2019). Fluoride removal from natural volcanic underground water by an electrocoagulation process: Parametric and cost evaluations. *Journal of environmental management*, 246, 472-483.
- Moges, G., Zewge, F., & Socher, M. (1996). Preliminary investigations on the defluoridation of water using fired clay chips. *Journal of African Earth Sciences*, 22(4), 479-482.
- Mohan, D., Singh, K. P., & Singh, V. K. (2008). Wastewater treatment using low cost activated carbons derived from agricultural byproducts—a case study. *Journal of Hazardous Materials*, 152(3), 1045-1053.
- Mondal, R., Pal, S., Bhalani, D. V., Bhadja, V., Chatterjee, U., & Jewrajka, S. K. (2018). Preparation of polyvinylidene fluoride blend anion exchange membranes via non-solvent induced phase inversion for desalination and fluoride removal. *Desalination*, 445, 85-94.

- Mudzielwana, R., Gitari, M. W., Akinyemi, S. A., & Msagati, T. A. M. (2017). Synthesis and physicochemical characterization of MnO<sub>2</sub> coated Na-bentonite for groundwater defluoridation: Adsorption modelling and mechanistic aspect. *Applied Surface Science*, 422, 745-753.
- Nawlakhe, W., WG, N., & KR, B. (1975). Defluoridation of water by Nalgonda technique.
- Nigussie, W., Zewge, F., & Chandravanshi, B. (2007). Removal of excess fluoride from water using waste residue from alum manufacturing process. *Journal of Hazardous Materials*, 147(3), 954-963.
- Nunes-Pereira, J., Lima, R., Choudhary, G., Sharma, P., Ferdov, S., Botelho, G., Lanceros-Méndez, S. (2018). Highly efficient removal of fluoride from aqueous media through polymer composite membranes. *Separation and Purification Technology*, 205, 1-10.
- Oguz, E. (2005). Adsorption of fluoride on gas concrete materials. *Journal of Hazardous Materials*, 117(2), 227-233.
- Onyango, M. S., Kojima, Y., Kuchar, D., Osembo, S. O., & Matsuda, H. (2005). Diffusion kinetic modeling of fluoride removal from aqueous solution by charge-reversed zeolite particles. *Journal of chemical engineering of Japan*, 38(9), 701-710.
- Onyango, M. S., Kojima, Y., Kumar, A., Kuchar, D., Kubota, M., & Matsuda, H. (2006). Uptake of fluoride by Al<sup>3+</sup> pretreated low-silica synthetic zeolites: adsorption equilibrium and rate studies. *Separation Science and Technology*, 41(4), 683-704.
- Parmar, H. S., Patel, J. B., Sudhakar, P., & Koshy, V. (2006). Removal of fluoride from water with powdered corn cobs. *Journal of environmental science & engineering*, 48(2), 135-138.
- Patel, R. K., Kumar, S., Chawla, A. K., Mondal, P., Teychene, B., & Pandey, J. K. (2019). Elimination of Fluoride, Arsenic, and Nitrate from water through adsorption onto nano-adsorbent: A Review. *Current Nanoscience*, 15(6), 557-575.
- Perrotta, M., Saielli, G., Casella, G., Macedonio, F., Giorno, L., Drioli, E., & Gugliuzza, A. (2017). An ultrathin suspended hydrophobic porous

- membrane for high-efficiency water desalination. *Applied Materials Today*, 9, 1-9.
- Qiao, J., Cui, Z., Sun, Y., Hu, Q., & Guan, X. (2014). Simultaneous removal of arsenate and fluoride from water by Al-Fe (hydr) oxides. *Frontiers of Environmental Science & Engineering*, 8(2), 169-179.
- Rao, S. M., & Mamatha, P. (2004). Water quality in sustainable water management. *Current Science*, 942-947.
- Raul, P. K., Devi, R. R., Umlong, I. M., Banerjee, S., Singh, L., & Purkait, M. (2012). Removal of fluoride from water using iron oxide-hydroxide nanoparticles. *Journal of nanoscience and nanotechnology*, 12(5), 3922-3930.
- Ren, J., & McCutcheon, J. R. (2017). Making thin film composite hollow fiber forward osmosis membranes at the module scale using commercial ultrafiltration membranes. *Industrial & Engineering Chemistry Research*, 56(14), 4074-4082.
- Richards, L. A., Vuachère, M., & Schäfer, A. I. (2010). Impact of pH on the removal of fluoride, nitrate and boron by nanofiltration/reverse osmosis. *Desalination*, 261(3), 331-337.
- Ritz, E., Hahn, K., Ketteler, M., Kuhlmann, M. K., & Mann, J. (2012). Phosphate additives in food—a health risk. *Deutsches Ärzteblatt International*, 109(4), 49.
- Roy, S., Das, P., Sengupta, S., & Manna, S. (2017). Calcium impregnated activated charcoal: Optimization and efficiency for the treatment of fluoride containing solution in batch and fixed bed reactor. *Process Safety and Environmental Protection*, 109, 18-29.
- Ruan, Z., Tian, Y., Ruan, J., Cui, G., Iqbal, K., Iqbal, A., Yan, S. (2017). Synthesis of hydroxyapatite/multi-walled carbon nanotubes for the removal of fluoride ions from solution. *Applied Surface Science*, 412, 578-590.
- Seo, J., Kushner, D. I., & Hickner, M. A. (2016). 3D printing of micropatterned anion exchange membranes. *ACS applied materials & interfaces*, 8(26), 16656-16663.

- Serbezyov, A., Moore, J. D., & Wu, Y. (2011). Adsorption equilibrium of water vapor on selexsorb-cdx commercial activated alumina adsorbent. *Journal of Chemical & Engineering Data*, 56(5), 1762-1769.
- Shrivastava, A., Kumar, S., & Cussler, E. (2008). Predicting the effect of membrane spacers on mass transfer. *Journal of membrane science*, 323(2), 247-256.
- Siddiqui, A., Farhat, N., Bucs, S. S., Linares, R. V., Picioreanu, C., Kruithof, J. C., Vrouwenvelder, J. S. (2016). Development and characterization of 3D-printed feed spacers for spiral wound membrane systems. *Water research*, 91, 55-67.
- Sivabalan, R., Rengaraj, S., Arabindoo, B., & Murugesan, V. (2003). Cashewnut sheath carbon: A new sorbent for defluoridation of water.
- Sivasamy, A., Singh, K. P., Mohan, D., & Maruthamuthu, M. (2001). Studies on defluoridation of water by coal-based sorbents. *Journal of Chemical Technology and Biotechnology*, 76(7), 717-722.
- Smitha, K., & Thampi, S. G. (2017). Experimental Investigations on Fluoride Removal from Water Using Nanoalumina-Carbon Nanotubes Blend. *Journal of Water Resource and Protection*, 9(07), 760.
- Sophia, A. C., Bhalambaal, V., Lima, E. C., & Thirunavoukkarasu, M. (2016). Microbial desalination cell technology: contribution to sustainable waste water treatment process, current status and future applications. *Journal of Environmental Chemical Engineering*, 4(3), 3468-3478.
- Sreedhar, N., Thomas, N., Al-Ketan, O., Rowshan, R., Hernandez, H., Al-Rub, R. K. A., & Arafat, H. A. (2018). 3D printed feed spacers based on triply periodic minimal surfaces for flux enhancement and biofouling mitigation in RO and UF. *Desalination*, 425, 12-21.
- Sun, P., Zhang, L., & Tao, S. (2019). Preparation of hybrid chitosan membranes by selective laser sintering for adsorption and catalysis. *Materials & Design*, 173, 107780.
- Suriyaraj, S., Bhattacharyya, A., & Selvakumar, R. (2015). Hybrid Al<sub>2</sub>O<sub>3</sub>/bio-TiO<sub>2</sub> nanocomposite impregnated thermoplastic polyurethane (TPU) nanofibrous membrane for fluoride removal from aqueous solutions. *RSC Advances*, 5(34), 26905-26912.

- Suriyaraj, S., Vijayaraghavan, T., Biji, P., & Selvakumar, R. (2014). Adsorption of fluoride from aqueous solution using different phases of microbially synthesized TiO<sub>2</sub> nanoparticles. *Journal of Environmental Chemical Engineering*, 2(1), 444-454.
- Tahaikt, M., El Habbani, R., Haddou, A. A., Achary, I., Amor, Z., Taky, M., . . . Elmidaoui, A. (2007). Fluoride removal from groundwater by nanofiltration. *Desalination*, 212(1), 46-53.
- Tan, W. S., Chua, C. K., Chong, T. H., Fane, A. G., & Jia, A. (2016). 3D printing by selective laser sintering of polypropylene feed channel spacers for spiral wound membrane modules for the water industry. *Virtual and Physical Prototyping*, 11(3), 151-158.
- Tang, Q., Duan, T., Li, P., Zhang, P., & Wu, D. (2018). Enhanced defluoridation capacity from aqueous media via hydroxyapatite decorated with carbon nanotube. *Frontiers in chemistry*, 6, 104.
- Thomas, N., Sreedhar, N., Al-Ketan, O., Rowshan, R., Al-Rub, R. K. A., & Arafat, H. (2018). 3D printed triply periodic minimal surfaces as spacers for enhanced heat and mass transfer in membrane distillation. *Desalination*, 443, 256-271.
- Thomas, N., Sreedhar, N., Al-Ketan, O., Rowshan, R., Al-Rub, R. K. A., & Arafat, H. (2019). 3D printed spacers based on TPMS architectures for scaling control in membrane distillation. *Journal of membrane science*, 581, 38-49.
- Tijing, L. D., Choi, J.-S., Lee, S., Kim, S.-H., & Shon, H. K. (2014). Recent progress of membrane distillation using electrospun nanofibrous membrane. *Journal of membrane science*, 453, 435-462.
- Tijing, L. D., Dizon, J. R. C., Ibrahim, I., Nisay, A. R. N., Shon, H. K., & Advincula, R. C. (2020). 3D printing for membrane separation, desalination and water treatment. *Applied Materials Today*, 18, 100486.
- Tijing, L. D., Woo, Y. C., Choi, J.-S., Lee, S., Kim, S.-H., & Shon, H. K. (2015). Fouling and its control in membrane distillation—A review. *Journal of membrane science*, 475, 215-244.

- Tijing, L. D., Woo, Y. C., Shim, W.-G., He, T., Choi, J.-S., Kim, S.-H., & Shon, H. K. (2016). Superhydrophobic nanofiber membrane containing carbon nanotubes for high-performance direct contact membrane distillation. *Journal of membrane science*, 502, 158-170.
- Tokunaga, S., Haron, M., Wasay, S., Wong, K., Laosangthum, K., & Uchiumi, A. (1995). Removal of fluoride ions from aqueous solutions by multivalent metal compounds. *International journal of environmental studies*, 48(1), 17-28.
- Tor, A., Danaoglu, N., Arslan, G., & Cengeloglu, Y. (2009). Removal of fluoride from water by using granular red mud: batch and column studies. *Journal of Hazardous Materials*, 164(1), 271-278.
- Tripathy, S. S., Bersillon, J.-L., & Gopal, K. (2006). Removal of fluoride from drinking water by adsorption onto alum-impregnated activated alumina. *Separation and purification technology*, 50(3), 310-317.
- Tsuji, M., & Abe, M. (1986). Possible radiochemical separations of anionic radionuclides by amorphous hydrous titanium dioxide. *Journal of radioanalytical and nuclear chemistry*, 102(2), 283-294.
- Tsuji, M., & Abe, M. (1991). Selective uptake of toxic elements by an amorphous titanium dioxide ion exchanger. *Journal of radioanalytical and nuclear chemistry*, 149(1), 109-118.
- Turner, B. D., Binning, P., & Stipp, S. (2005). Fluoride removal by calcite: evidence for fluorite precipitation and surface adsorption. *Environmental science & technology*, 39(24), 9561-9568.
- Valino, A. D., Dizon, J. R. C., Espera Jr, A. H., Chen, Q., Messman, J., & Advincula, R. C. (2019). Advances in 3D printing of thermoplastic polymer composites and nanocomposites. *Progress in Polymer Science*, 101162.
- Viswanathan, N., & Meenakshi, S. (2008). Effect of metal ion loaded in a resin towards fluoride retention. *Journal of Fluorine Chemistry*, 129(7), 645-653.
- Viswanathan, N., & Meenakshi, S. (2009). Role of metal ion incorporation in ion exchange resin on the selectivity of fluoride. *Journal of Hazardous Materials*, 162(2), 920-930.

- Wang, J., Wu, L., Li, J., Tang, D., & Zhang, G. (2018). Simultaneous and efficient removal of fluoride and phosphate by Fe-La composite: Adsorption kinetics and mechanism. *Journal of Alloys and Compounds*, 753, 422-432.
- Werber, J. R., Osuji, C. O., & Elimelech, M. (2016). Materials for next-generation desalination and water purification membranes. *Nature Reviews Materials*, 1(5), 1-15.
- Woo, Y. C., Kim, Y., Yao, M., Tijing, L. D., Choi, J.-S., Lee, S., . . . Shon, H. K. (2018). Hierarchical composite membranes with robust omniphobic surface using layer-by-layer assembly technique. *Environmental science & technology*, 52(4), 2186-2196.
- Wu, J., Zhou, L., Chen, L., & Zhao, J. (2012). Hydrothermal Synthesis, Physical Characterization and Fluoride Adsorption of TiO<sub>2</sub>/CeO<sub>2</sub>. *Asian Journal of Chemistry*, 24(6), 2661.
- Wu, K., Zhang, N., Liu, T., Ma, C., Jin, P., Zhang, F., Wang, X. (2017). Competitive adsorption behaviors of arsenite and fluoride onto manganese-aluminum binary adsorbents. *Colloids and Surfaces A: Physicochemical and Engineering Aspects*, 529, 185-194.
- Yadav, A. K., Kaushik, C., Haritash, A. K., Kansal, A., & Rani, N. (2006). Defluoridation of groundwater using brick powder as an adsorbent. *Journal of Hazardous Materials*, 128(2), 289-293.
- Yan, X., Song, K., Wang, J., Hu, L., & Yang, Z. (1998). Preparation of CeO<sub>2</sub>-TiO<sub>2</sub>/SiO<sub>2</sub> and its removal properties for fluoride ion. *Journal of Rare Earths*, 16(4), 275-280.
- Yanar, N., Son, M., Yang, E., Kim, Y., Park, H., Nam, S.-E., & Choi, H. (2018). Investigation of the performance behavior of a forward osmosis membrane system using various feed spacer materials fabricated by 3D printing technique. *Chemosphere*, 202, 708-715.
- Yao, M., Ren, J., Akther, N., Woo, Y. C., Tijing, L. D., Kim, S.-H., & Shon, H. K. (2019). Improving membrane distillation performance: Morphology optimization of hollow fiber membranes with selected non-solvent in dope solution. *Chemosphere*, 230, 117-126.



- Yao, M., Woo, Y. C., Tijing, L. D., Shim, W.-G., Choi, J.-S., Kim, S.-H., & Shon, H. K. (2016). Effect of heat-press conditions on electrospun membranes for desalination by direct contact membrane distillation. *Desalination*, 378, 80-91.
- Yildiz, Y. S., Koparal, A. S., İrdemez, S., & Keskinler, B. (2007). Electrocoagulation of synthetically prepared waters containing high concentration of NOM using iron cast electrodes. *Journal of hazardous materials*, 139(2), 373-380.
- Ying, Y., Ying, W., Li, Q., Meng, D., Ren, G., Yan, R., & Peng, X. (2017). Recent advances of nanomaterial-based membrane for water purification. *Applied Materials Today*, 7, 144-158.
- You, J., Preen, R. J., Bull, L., Greenman, J., & Ieropoulos, I. (2017). 3D printed components of microbial fuel cells: Towards monolithic microbial fuel cell fabrication using additive layer manufacturing. *Sustainable Energy Technologies and Assessments*, 19, 94-101.
- Yuan, S., Zhu, J., Li, Y., Zhao, Y., Li, J., Van Puyvelde, P., & Van der Bruggen, B. (2019). Structure architecture of micro/nanoscale ZIF-L on a 3D printed membrane for a superhydrophobic and underwater superoleophobic surface. *Journal of materials chemistry A*, 7(6), 2723-2729.
- Zhang, C., Li, Y., Wang, T.-J., Jiang, Y., & Fok, J. (2017). Synthesis and properties of a high-capacity iron oxide adsorbent for fluoride removal from drinking water. *Applied Surface Science*, 425, 272-281.
- Zhang, D., Xiao, J., Guo, Q., & Yang, J. (2019). 3D-printed highly porous and reusable chitosan monoliths for Cu (II) removal. *Journal of materials science*, 54(8), 6728-6741.
- Zhang, J., Chen, N., Su, P., Li, M., & Feng, C. (2017). Fluoride removal from aqueous solution by zirconium-chitosan/graphene oxide membrane. *Reactive and Functional Polymers*, 114, 127-135.
- Zhang, Y.-X., & Jia, Y. (2018). Fluoride adsorption on manganese carbonate: Ion-exchange based on the surface carbonate-like groups and hydroxyl groups. *Journal of colloid and interface science*, 510, 407-417.

- Zhang, Y., Lin, X., Zhou, Q., & Luo, X. (2016). Fluoride adsorption from aqueous solution by magnetic core-shell Fe<sub>3</sub>O<sub>4</sub>@ alginate-La particles fabricated via electro-coextrusion. *Applied Surface Science*, 389, 34-45.
- Zhou, J., Cheng, Y., Yu, J., & Liu, G. (2011). Hierarchically porous calcined lithium/aluminum layered double hydroxides: facile synthesis and enhanced adsorption towards fluoride in water. *Journal of Materials Chemistry*, 21(48), 19353-19361.
- Zhou, J., Zhu, W., Yu, J., Zhang, H., Zhang, Y., Lin, X., & Luo, X. (2018). Highly selective and efficient removal of fluoride from ground water by layered Al-Zr-La Tri-metal hydroxide. *Applied Surface Science*, 435, 920-927.
- Zuo, Q., Chen, X., Li, W., & Chen, G. (2008). Combined electrocoagulation and electroflotation for removal of fluoride from drinking water. *Journal of Hazardous Materials*, 159(2), 452-457.

## CHAPTER 3

### MATERIALS AND METHODS

*This chapter discusses the reagents used for the nanoadsorbent synthesis, fluoride stock solution preparation along with instruments used for quantification of prepared nanoadsorbent and fluoride solution. A brief overview of instruments such as X-ray Diffraction (XRD), Scanning Electron Microscope (SEM)/ Energy Dispersive X-Ray (EDX), Brunauer Emmett and Teller (BET), Fourier Transform Infrared Spectroscopy (FTIR), Ion-Selective Electrode (ISE) Meter and Inductively Coupled Plasma - Optical Emission Spectrometry (ICP-OES), 3D Printer and Thermal Mechanical Analyzer (TMA).*

#### 3.1 MATERIALS

The reagents used in this study for adsorbent synthesis are defined in Table 3.1 and Table 3.2 lists the reagents used during fluoride removal studies.

**Table 3.1** Reagents used for the adsorbent synthesis

Reagent	Particulars	Source
Iron (III) nitrate nonahydrate	Assay > 98%	Sisco Research Laboratories Pvt. Ltd., India
Sodium hydroxide pellets	Assay > 97%	
Titanium(IV) isopropoxide	Assay > 97%	Merck, India
Isopropanol	70% in H <sub>2</sub> O	
Acetic acid	Assay > 99.7%	

**Table 3.2** Reagents used during fluoride removal study

Reagents	Particulars	Source
Nitric acid	Assay > 70 %	Merck, India
Sodium fluoride	Assay > 99 %	
Acetone	Assay > 99 %	
Sodium chloride	Assay > 99%	
Glacial acetic acid	Assay > 99.7%	
1,2-Cyclohexylenedinitrilotetraacetic acid	Assay > 99%	
Sodium hydroxide pellets	Assay > 97 %	

### 3.2 INSTRUMENTS

#### 3.2.1 X-RAY DIFFRACTION

X-ray diffraction (XRD) is one of the most extensively used techniques for the characterization of nanoparticles. XRD provides information regarding the crystalline structure, nature of the phase, lattice parameters, and crystalline grain size. Here Bruker D8 Advance Eco X-ray diffractometer (Fig 3.1) was used to record the structural analysis of synthesized adsorbents.



**Fig 3.1** Bruker D8 Advance Eco X-ray diffractometer

The radiation (Cu  $K_{\alpha}$ ) emanating from the X-ray tube is diffracted at the specimen and recorded by a detector. Whenever the Bragg condition,  $2d \sin \theta = n\lambda$ , is satisfied, the incident X-ray beam is diffracted at the specimen and reaches the detector. The detector converts the X-ray quanta into electron pulses, which are recorded by recorder.

Here the crystallite size of the material is determined from the width of the Bragg reflection and is given by the Scherrer formula,  $l = \frac{0.9 \lambda}{B \cos \theta_b}$

where  $l$  is the length of the crystal in the direction perpendicular to the reflecting planes,  $B$  is the full width at half maximum (FWHM) of the Bragg reflection in the radians on the  $2\theta$  scale and  $\theta_b$  is the Bragg reflection angle.

### **3.2.2 SCANNING ELECTRON MICROSCOPE AND ENERGY DISPERSIVE X-RAY**

Scanning electron microscope (SEM) utilized electrons rather than using light for analysing the morphology of adsorbents. About 0.5 to 1 mg nanopowder was properly washed with ethanol and dried at 40 °C for 4 hrs in hot air oven to remove any water present in the specimen. The nanopowder was placed on a double sided carbon tape which is pasted on the sample holder. The non-conducting sample such as activated carbon was coated with a thin layer of gold (approx. 20 nm) in a sputtering apparatus whereas the conducting samples such as hematite and titanium dioxide is not coated with gold. The sample was further placed in SEM for analysis. The SEM creates high-resolution images, which ensures that closely spaced features can be analyzed at high magnification. Field Emission Electron Microscope (FEI Quanta 200F model) with a resolution of 2 nm and magnification 500000 x was used to study the surface morphology of the nanocrystalline thin films and nanopowder shown in Fig 3.2. FESEM uses field emission electron gun which provides improved special resolution down to 1.5 nm that is 3 to 6 times better than conventional SEM and minimized sample charging and damage. In conventional SEM instrument electrons are thermionically emitted from a tungsten or lanthanum hexaboride ( $LaB_6$ ) cathode and are

accelerated towards an anode. These electrons can also be emitted via field emission (FE).



**Fig 3.2 SEM (FEI Quanta 200F)**

The energy range from 100 eV to 50 keV of the electron beam is focused on one or two condenser lenses at a very fine focal spot size (1 to 5 nm). The field emission tip is generally made of a single crystal tungsten wire sharpened by electrolytic etching. A tip diameter of 100 to 1000 Å is used, with the apparent source size much less than that. Using the energy dispersive x-ray analysis (EDX) attachment with the SEM, elemental composition analysis can also be done. An EDX spectrum normally displays peaks corresponding to the energy levels for which the most X-rays had been received. Each of these peaks is unique to an atom and therefore corresponds to a single element. The higher a peak in a spectrum, the more concentrated the element is in the specimen.

### **3.2.3 BRUNAUER EMMETT AND TELLER**

The specific surface area of material and physical adsorption of gas molecules on a solid surface is performed using Brunauer-Emmett-Teller (BET). During the quantification of the surface area using BET, surface probing gas is used which does not react chemically with the surface of the material. Here nitrogen (N<sub>2</sub>) is the most commonly used gas. The BET analysis is performed

at a temperature of 77 K. The specific surface area observed using BET analysis might depend upon the adsorbate molecule used and its adsorption cross-section. The amount of gas adsorbed depends on the exposed surface not only but also on the temperature, gas pressure, and strength of an interaction between the gas and solid. The well-known amount of N<sub>2</sub> gas is released stepwise into the sample. The BET and Langmuir surface area, BJH adsorption and desorption cumulative surface area of pores, BJH adsorption and desorption cumulative volume of pores, t-plot micropore volume, total pore volume, average particle size, and many more data are obtained from BET analysis adsorption isotherm.

Accelerated Surface Area and Porosimetry System, Micromeritics (ASAP 2020) instrument shown in Fig 3.3, was used for the detection of specific surface area and porosity of synthesized adsorbents.



**Fig 3.3** Accelerated Surface Area and Porosimetry System, Micromeritics, (ASAP 2020)

### **3.2.4 FOURIER TRANSFORM INFRARED SPECTROSCOPY**

Fourier transform infrared spectroscopy (FTIR) is a technique used to obtain an infrared spectrum of absorption or emission of a solid, liquid, or gas. An FTIR spectrometer simultaneously collects high-spectral-resolution data over a wide spectral range. A 0.5 mm thick pellet of 15 mm diameter was prepared for the mixture of synthesized nanoadsorbents ( $1 \pm 0.2$  mg) and potassium

bromide ( $100 \pm 10$  mg). The prepared pellet was placed in a sample holder for analysis using PerkinElmer Frontier instrument (Fig 3.4).



**Fig 3.4** PerkinElmer Frontier FTIR

Operating the spectrophotometer at  $28 \pm 2$  °C, the infrared (IR) spectra were obtained between the ranges of  $4000 \text{ cm}^{-1}$  to  $400 \text{ cm}^{-1}$  wavenumbers while using 32 scans. Throughout the passage of IR radiation through the sample, energy absorption is modulated due to bending or stretching movements of the bonds within the sample. Therefore, by analyzing the FTIR spectrum the presence or absence of bonds can be inferred. The peaks detected at different wavenumbers were matched with data available in standard form for certain identified bond stretching.

### **3.2.5 ION SELECTIVE ELECTRODE METER**

The Thermo Scientific Orion Dual Star pH/ISE benchtop ion-selective electrode (ISE) meter (Fig 3.5) was used for the quantification of fluoride concentration, pH range, and temperature. For fluoride concentration, ISE displayed units as ppm (parts per million) and mg/L (milligrams per litre) whereas for temperature unit to degree Celsius (°C) or degree Fahrenheit (°F). The valence number for pH is +1 and fluoride is -1 whereas the theoretical slope values for pH and fluoride are +59.16 and -59.16 respectively.

The major specification of the meter in terms of range, resolution, relative accuracy, and calibration points (Table 3.3).





**Fig 3.5** Thermo Scientific Orion Dual Star pH/ISE

**Table 3.3** Major specification of ISE meter

Parameter Particular	pH	ISE (Ion Concentration)	Temperature
Range	-2.000 to 19.999	0.0001 to 19900	-5 to 105 °C
Resolution	0.1/0.01/0.0 01	0.0001	0.1 °C
Relative accuracy	±0.002	±0.2 mV	±0.1 °C
Calibration points	1 to 6	2 to 6	1

### 3.2.6 INDUCTIVELY COUPLED PLASMA - OPTICAL EMISSION SPECTROMETRY

Inductively coupled plasma - optical emission spectrometry (ICP-OES) (Fig 3.6) is a technique where the composition of elements present in water samples can be determined using plasma and a spectrometer. The sample for analysis was sent by a peristaltic pump through a nebulizer into a spray chamber. This produces aerosol which is lead into argon plasma. The temperature of the plasma is 6000-7000 K. In the quartz torch atomization and ionizations of the water samples occur. The light intensity on the wavelength is measured and with the calibration calculated into a concentration. The major application of ICP-OES here is to perform a leach test for the detection of metal ions in the range of high ppm to sub-ppb present in the treated water.



**Fig 3.6** PlasmaQuant PQ9000 ICP-OES

### 3.2.7 3D PRINTER

The MiiCraft 3D printer (PN#95.LF800G004) from Rays Optics, Taiwan was used for the purpose of this work and was based on the Stereolithography (SLA) technique. A minimum resolution of 56 microns on the XY-axis and 50 microns on the Z-axis is offered by this printer. It uses the method of printing from the bottom-up approach and UV resin.

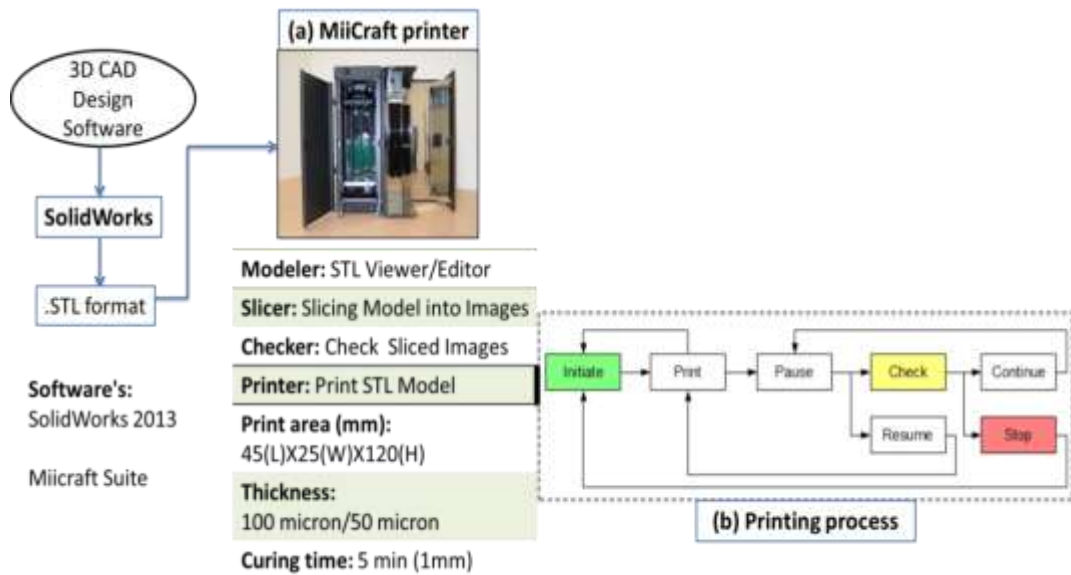


**Fig 3.7** (a) MiiCraft printer (b) Printing process

The output file obtained from the designing software must basically be saved in standard tessellation language (.stl) format. The file is used by the MiiCraft STL

Viewer for positioning the design on the printer platform. This process is further followed by slicing of entire design into 50 micron distinct slices using the Slicer program and generates the final index file applicable for printing in the ‘Print STL Model’ module. During the printing process, the height of the 1 mm model, which uses standard UV curable polymer as input material, takes less than 5 minutes during printing. A transparent resin (MA-Y G2005 T), obtained by the company, with 150 °C flash point and a specific gravity of 1 g/mL at 25 °C, is the material used here (Table 3.4). The printing processes flow performed for the fabrication of a device is shown in Fig 3.7 (b).

**Table 3.4** Composition/Information on ingredients for 3D printer

<b><i>Resin Property</i></b>	
Boiling Point	150 °C
<b><i>Composition of components</i></b>	<b><i>Weight %</i></b>
Acrylate Compounds	88~96
Photo Initiator	1~5
Additives	0.2~8

### 3.2.8 THERMAL MECHANICAL ANALYZER

Thermal Mechanical Analyzer (TMA) analyzes the deformation of a material under some controlled conditions like force, atmosphere, time, and temperature.



**Fig 3.8** Thermal Mechanical Analyzer

The Q400EM (Fig 3.8) module of TMA is used here to measure polymer viscoelastic properties using transient (e.g., stress relaxation) or dynamic tests. In stress relaxation, a fixed strain is applied, and stress decay is monitored.

### **3.3 EXPERIMENTAL PLAN**

In this study, first of all, the fabrication of a microchannel device was done using the MiiCraft 3D printer. The part of fabricated device was tested for stress-strain analysis. These fabricated devices were then loaded with the synthesized adsorbents. These loaded microchannel devices were investigated to study their fluoride removal efficiency at certain parameters such as neutral pH, fixed flow rate, and room temperature. Here the loading of adsorbent dosage varied depending upon both the design of the microchannel device and the adsorbent loaded. For the fluoride removal efficiency study, the stock solution of fluoride was prepared. A 1 L volume of stock solution of fluoride having a concentration of 1000 mg/L was prepared using sodium fluoride (2.210 g of NaF) (Merck, India) and double distilled water by 10-minute sonication and stored in a polypropylene bottle. Thin disposable nitrile gloves were used to handle fluoride solutions. The variable concentration of the fluoride solution was prepared by dilution of the stock solution. After the process of fluoride removal from water, the loaded adsorbent gets saturated, at this stage, the initial and final concentration is the same. The loaded adsorbents were taken out for the regeneration process by using both acidic and basic medium. And also the treated water obtained was tested for leach test for the detection of any traces of metal ions.

### **3.4 CONCLUSION**

The materials and reagents applicable for the preparation of adsorbent and fluoride stock solution are defined. After the completion of the preparation process, the characterization is another major part that has to be carried out to evaluate the reactions performed. So for the evaluation purpose and fabrication of the 3D model, instruments to be used are also discussed briefly.

## CHAPTER 4

### FABRICATION OF MICROCHANNEL BY 3D PRINTING

*This chapter discusses the 3D printing technology used for the fabrication of device. The various designs having a change in dimensions were designed using Solid works software. These designs were printed using a 3D printer and tested for their continuity and flexibility.*

#### 4.1 GENERAL

The additive manufacturing follows the following fabrication process of a required model (Fig 4.1). The authors investigated a method for particle filtration of sizes ranging from micro to nano using shear-modulated inertial migration in straight microchannels having a rectangular cross-section (Bhagat, Kuntaegowdanahalli, & Papautsky, 2008).

The FDM technique was used for the fabrication of microchannels. These microchannels of different structure and size (circular, straight, sinusoidal, 3D curved, and cross-linked curved microchannels) were fabricated by controllably extruding sacrificial molds (Tang et al., 2019).

ProJet 5500X inkjet printer was used by researchers which utilize a photopolymer composite material for the fabrication of robust and bendable microchannel based strain sensor (Agarwala et al., 2017).

The application of 3D printed microchannel has also been explored by various researchers in the detection of human breast cancer cells (Motaghi, Ziyadeh, Mehrgardi, Kajani, & Bordbar, 2018), boiling heat transfer enhancement (Zhang, Chai, Xu, Liu, & Sun, 2018), endochondral bone repair (Daly, Pitacco, Nulty, Cunniffe, & Kelly, 2018) and many more.

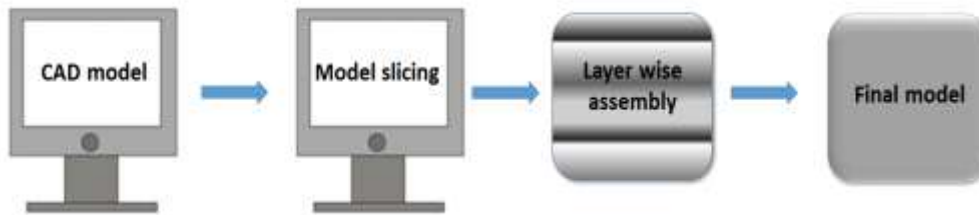


**Fig 4.1** Additive Manufacturing Process

The concept of printing microchannel using MiiCraft 3D was adopted from published research work where a microfluidic channel having a 1 mm diameter was printed for evaluating the milk adulteration property (Venkateswaran, Sharma, Dubey, Agarwal, & Goel, 2016).

#### **4.2 3D PRINTING OF MICROCHANNEL**

3D printing covers a broad variety of technologies, most of which are also used in industrial manufacturing. However, for micro-manufacturing, one specific method, called Stereolithography (SLA), is commonly used (Snyder et al., 2014). The MiiCraft 3D printer available is one of the SLA based printers that can go up to a minimum resolution of 56 microns on the XY axis and 50 microns on the Z axis. In order to fabricate a 3D structure with a SLA technique, the first step is to create the digital model of the structure using computer-aided design software (CAD). Preparing digital models is the first transformed into a standard tessellation language (.stl) file format. The surface geometry of the 3D model has to be fabricated in the form of interconnecting tessellated triangles, followed by utilizing the dedicated software into the sequential layer of desired thickness, resolution, and accuracy. The resulting data is then transferred to the printing apparatus, which fabricates the 3D structure layer by layer starting from the bottom to up. The resulting 3D model is then exposed to UV rays for 600 seconds for post-curing in a different chamber. The post-curing process enhances the mechanical properties of the printed 3D structure. Fig 4.2 depicts the procedure for the fabrication of the 3D model via stereolithography technique.

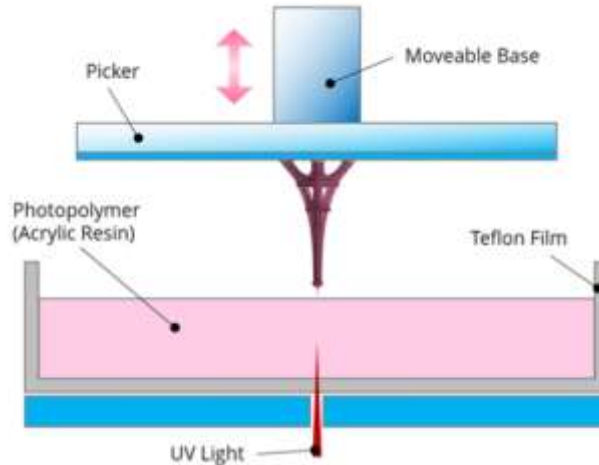


**Fig 4.2** Stereolithography printing process (Sharma et al., 2017)

This approach offers us the versatility of printing complex 3D structures utilizing polymeric materials (O'Neill et al., 2014).

#### **4.3 SOLID MODELLING**

Solid modelling (SM), deals with CAD for the creation of geometrical shapes, surfaces, bodies, using digital toolset available in a computer graphics environment. The feature of computer graphics is to create a graphical representation of a desired physical object or part. The most known SM methods are Constructive Solid Geometry (CSG) and Boundary Representation (Brep). Many CAD applications are available out of which Solidworks 2013 published by Dassault Systèmes is used for SM.

#### **4.4 DEVICE DESIGN**

The model of the device was designed in two categories cuboid and cylindrical structure. In cylindrical structure two models were designed plain microchannel and spiraled microchannel. The selection of pore size (1.5 and 2 mm) was done based on the minimum pore size that can be obtained using the available 3D printer and also the purpose of proper adsorbent loading should be fulfilled.

#### 4.4.1 CUBOID STRUCTURE

The first cuboid structure comprises the length, breadth, and height of 25 mm X 25 mm X 5 mm depending upon the available printing area. The device consists of 7 numbers of circular microchannels each having a pore size of 2 mm. The drawing and CAD model of the device is shown in Fig 4.3 (a) and 3D printed output of the design is shown in Fig 4.3 (b). The designing of this model was done to test the proper fabrication of the channel and complete the device using a 3D printer. The reason to keep 7 numbers of channels was to keep a sidewall of 3 mm thickness on both corners and 1 mm gap between each channel. The 3D printed device was tested for the channel's uniformity. This test was performed using a 5 mL syringe.

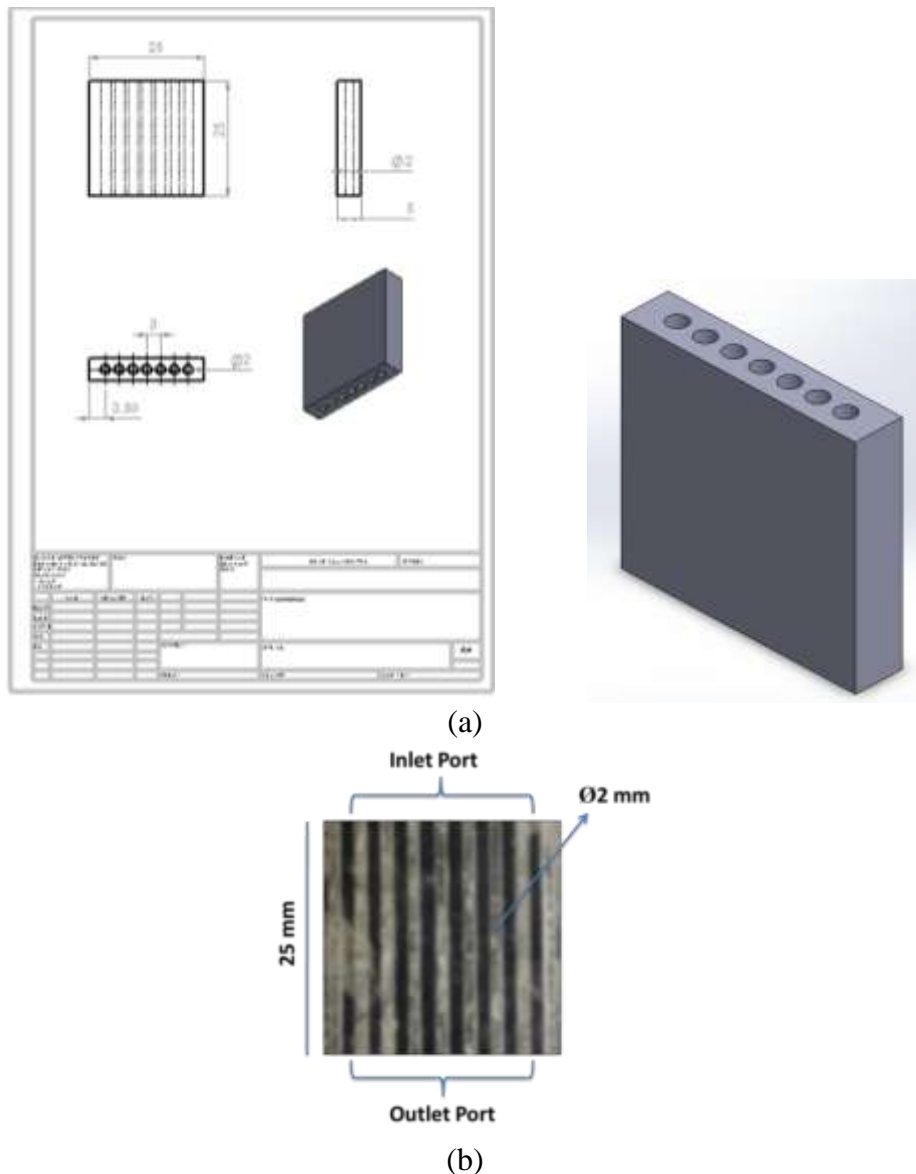


**Fig 4.3** (a) Drawing and CAD model (isometric view) (b) 3D printed device



The syringe was filled with water and then from each channel, a water flow test was performed. It was found that each channel was accurately fabricated and there was no blockage. In reference to this tested model the design was further modified where the number channels were increased along with the change in device dimension. Fig 4.4 shows the drawing of the modified design.

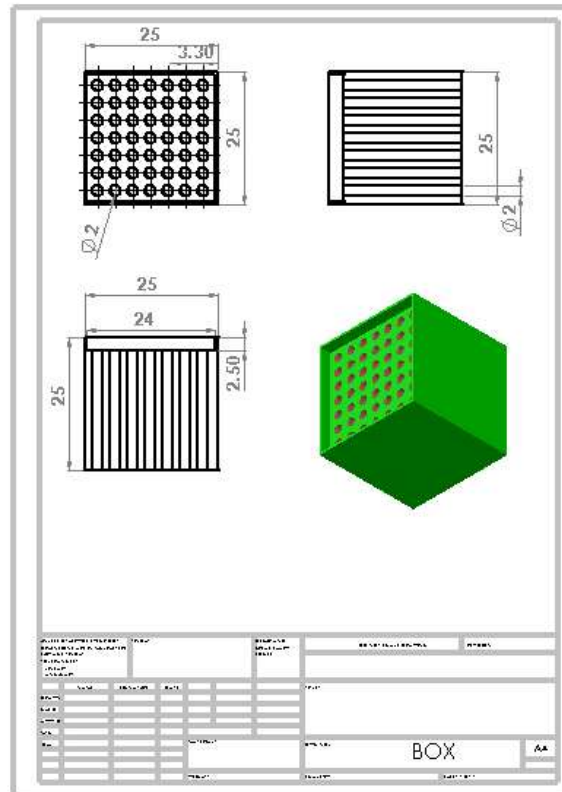


**Fig 4.4** Drawing of the cube structure

In this modified design two separate devices were designed having a pore size of 2 and 1.5 mm with the same cuboid pattern having dimension 25 mm X 25 mm X 25 mm. The CAD models of devices are shown in Fig 4.5 (a) the top view of 2 mm pore size design and (b) the cross-sectional view of 1.5 mm pore size design.

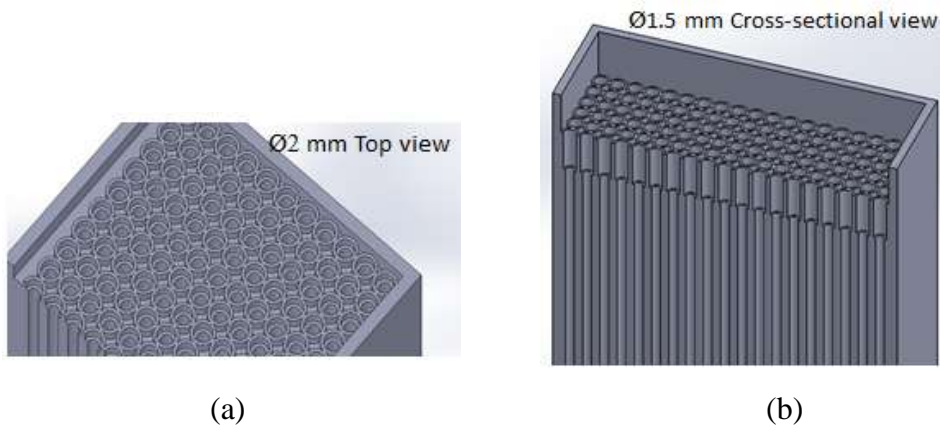


**Fig 4.5** CAD models of the cuboid design (a) 2 mm and (b) 1.5 mm pore size

The 3D printed output of these designs having a 2 mm pore size and 1.5 mm pore size are shown in Fig 4.6 (a) and (b) respectively.

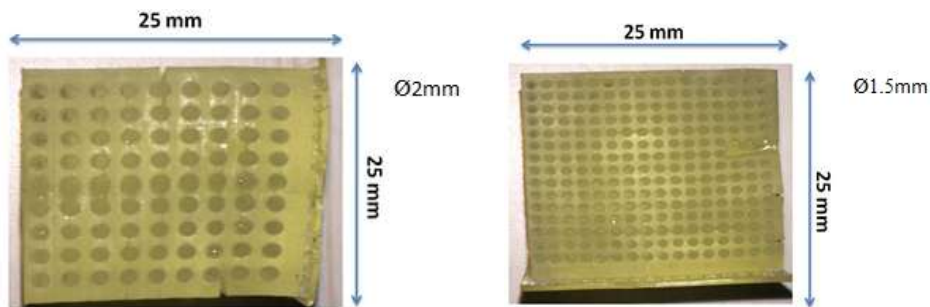


**Fig 4.6** 3D printed (a) 2 mm and (b) 1.5 mm pore size model

These printed devices were tested for their channel uniformity by water flow test using a syringe. During the testing process for 2 mm pore size design the maximum number of channels shown uniformity in fabrication but few channels were blocked. In the same pattern the 1.5 mm pore size design was tested and it was observed that the maximum number of channels was showing blockage. The reason for this challenge was due to an increase (congestion) in the number of channels in comparison to the previous design and also the improper resin curing during the formation of each slice.

Overall the 2 mm pore size design showed better fabrication of the device. But this device also has shown major problems in fitting to the available set up of column in our lab, as it is found that the traditional shape of the column is

generally cylindrical in shape. Due to the cylindrical pattern of the column, airtight fitting of the printed device was improper. Both the reasons such as channel blockage and improper fitting of the device led to a further modification in the design.

#### 4.4.2 CYLINDRICAL STRUCTURE

The cuboid design and 3D printed model of cuboid has shown that the channel having a pore size of 2 mm and 1.5 mm can be fabricated. But there is a need for a decrease in the number of channels and the outer structure of the device. The modified design was further designed in reference to the available traditional column prototype (García-Sánchez et al., 2017; Mohan, Singh, Kumar, & Hasan, 2017) (Fig 4.7).

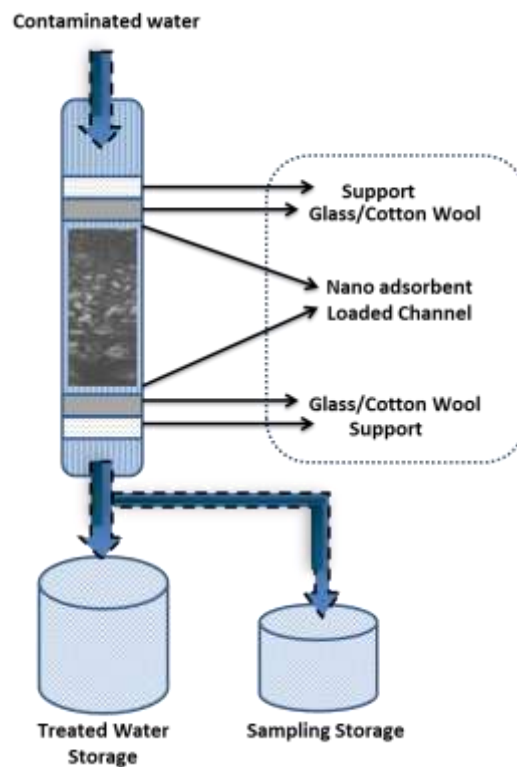


**Fig 4.7** Tradition column prototype

The design was divided into three parts inlet section, the cylindrical structure of the device, and the outlet section. The inlet and outlet section is designed in a truncated cone shape (Fig 4.8), the dimension shown in the figure are in mm. Here the total length of the cone is 20 mm where the top surface is of 15 mm

diameter which is having a pore size of 1 mm and the bottom end is kept open having a diameter of 25 mm.



**Fig 4.8** Inlet and outlet section

The cylindrical structure of the device as shown in Fig 4.9 was designed. The length of the device is 25 mm. Here the channels were designed with two separate models having different pore sizes of 2 mm and 1.5 mm.

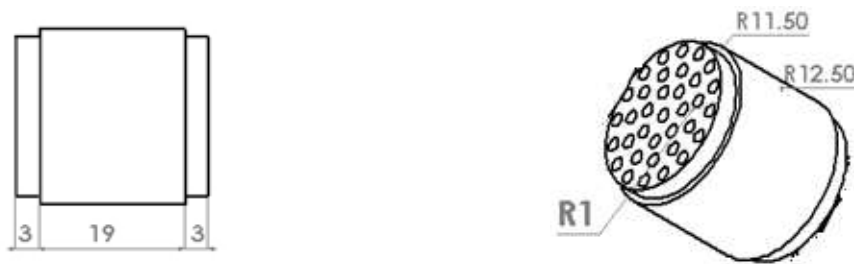


**Fig 4.9** Cylindrical structure of the device

The structure consists of a groove that was appropriate to assemble the truncated cone of both sides of the cylinder (Fig 4.10).



**Fig 4.10** Final assembled CAD model

The complete drawing and CAD model of the new design having a pore size of 2 mm are shown in Fig 4.11 (a) and (b) respectively.

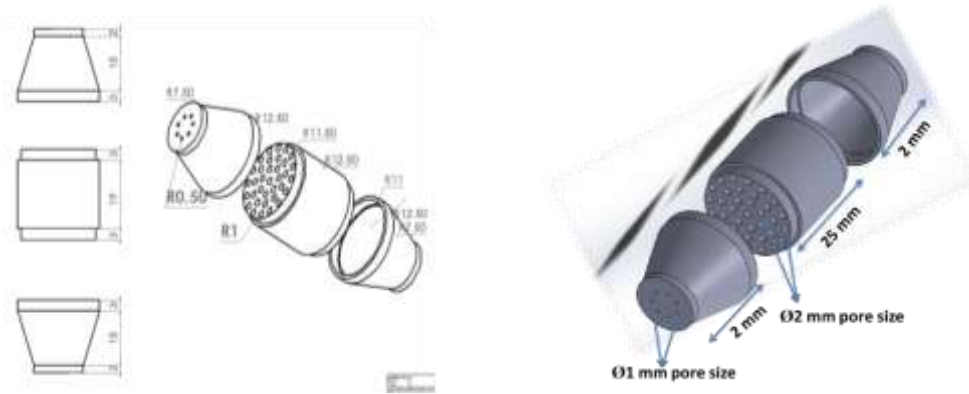


**Fig 4.11** (a) Drawing and (b) CAD model of cylindrical design (Patel, Chawla, Loulergue, Teychene, & Pandey, 2019)

The drawing and a CAD model of design having a pore size of 1.5 mm is shown in Fig 4.12 (a) and (b) respectively.

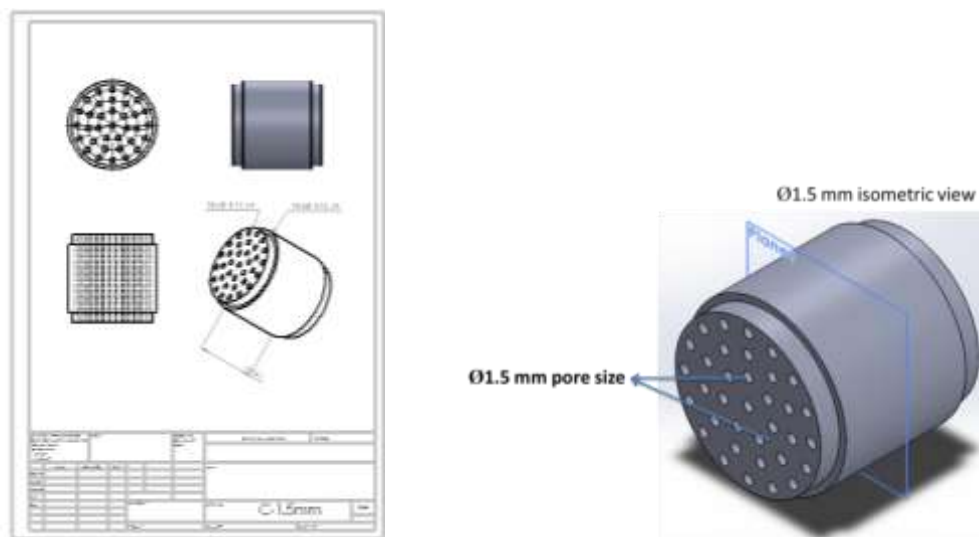


**Fig 4.12** (a) Drawing and (b) CAD model of a channel having a 1.5 mm pore size

Such above prototypes were further implemented for fabrication using the MiiCraft 3D printer. For printing of cuboid structure the major concern was to check the proper fabrication of channels as the outer frame was previously fabricated and it was successfully printed (Patel & Awasthi, 2017).

During the fabrication process of the truncated cone and cylindrical structure model, it was observed that some errors got occurred during the printing (Fig 4.13).

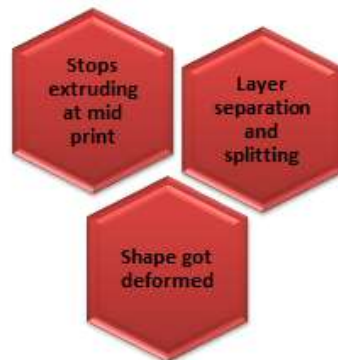
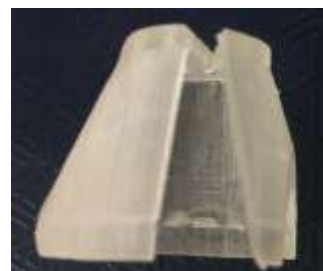


**Fig 4.13** Printing errors

Fig 4.14 shows the error observed for the printing of truncated cone where the shape of the cone got deformed due to the elongation of the corner edges (Fig 4.14 (a)) and the incomplete printing of the cone (Fig 4.14 (b)).



(a)



(b)

**Fig 4.14** Truncated cone (a) Elongation of cone (b) Splitting edge

But for the printing of cylindrical structure (Fig 4.15) it was found that the last layer of the device was not formed properly.



**Fig 4.15** Cylindrical structure deformation

The above observed printing errors occurred due to the printing operation setting, resin tank, and the printer nozzle maintenance (Fig 4.16). The printing operation here was varied in accordance with the printing of the cuboid structure as this design was attempted for the first time with this printer in our R&D lab.



**Fig 4.16** Printing error parameters

All the errors were considered that occurred during the initial printing process of the designed model. The printer setting was done as per requirement for the proper fabrication of the truncated cone and cylindrical structure. The perfectly 3D printed models of the designed device parts are shown in Fig 4.17.

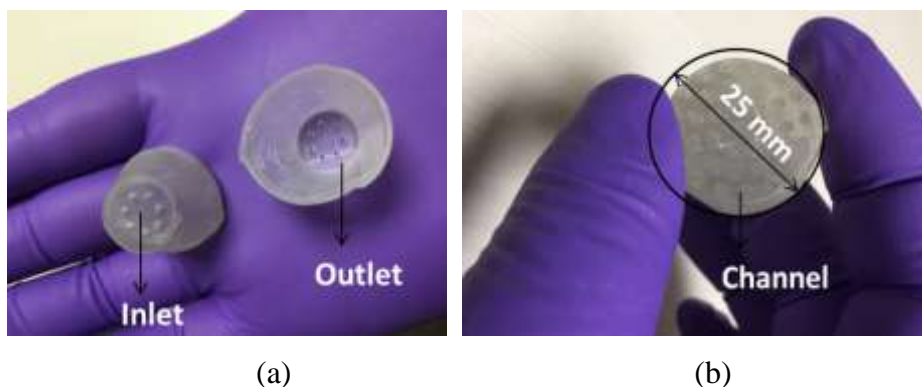


**Fig 4.17** (a) Inlet and outlet section (b) Cylindrical structure

The two different cylindrical structures having 2 mm pore size channels and 1.5 mm pore size channels were printed accordingly using the MiiCraft 3D

printer as shown in Fig 4.18. Both the structures 2 mm pore size and 1.5 mm pore size have a total number of 35 channels and the pattern the channels were circular and plain in design.



**Fig 4.18** 3D printed parts of the filter

These fabricated channels were performed for uniformity checks by performing a water flow test where again a syringe was used. The syringe was filled with water and from each channel water was passed to check the continuity. In comparison to the cuboid structure the number of channels was reduced to a large extent and there was proper symmetry between each channel. This change in design support positively during the fabrication of the device and the test results also supported it. In the process of water flow test from the channels it was found that the channels were uniformly fabricated and there was no occurrence of blockage.

### **SPIRALED MICROCHANNEL**

In accordance with the successful fabrication of cylindrical structure having plain microchannel, the design was further modified. The design was modified to increase the resistance in flow of water in comparison with plain microchannels. In modified design the structural design used was cylindrical having a channel of 2 mm pore size. The modification in the design is shown in the drawing sheet (Fig 4.19) where the internal surface of the channels is now designed in the spiral form.



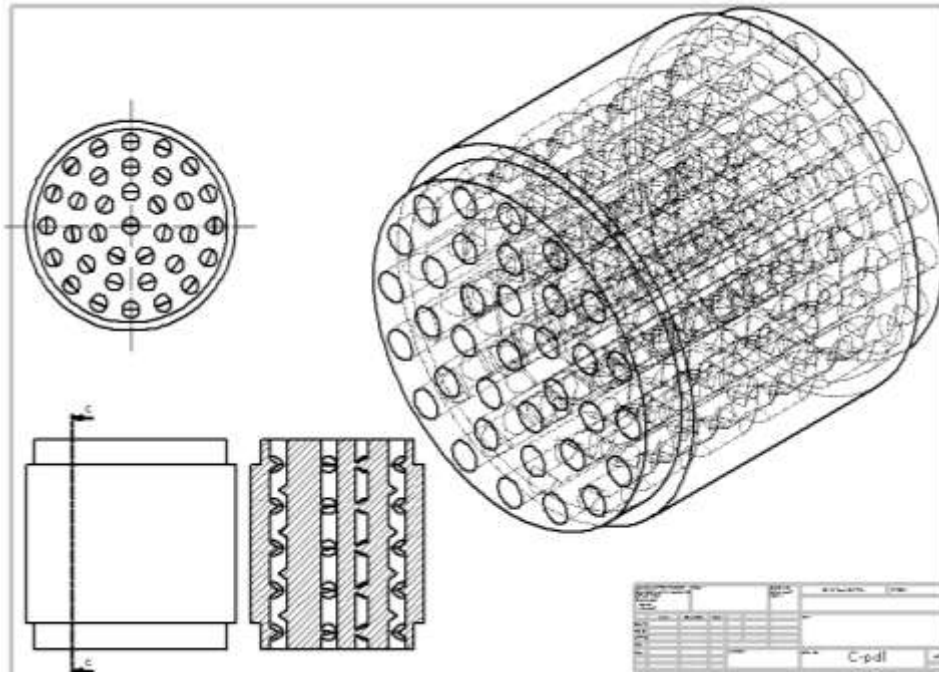


**Fig 4.19** Drawing of spiraled microchannels

Fig 4.20 shows the cross-section view CAD model of the modified design for the cylindrical structure.

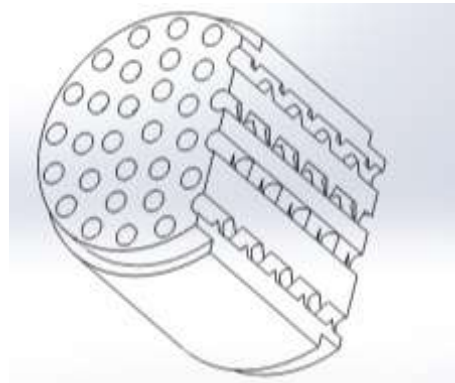


**Fig 4.20** Cross-sectional CAD view showing the internal pattern of channel

This new design was further fabricated using a 3D printer and tested for the proper formation of channels. The steps involved for testing were followed the same as it was done for the plain circular channel. In this new model the outlet section and the inlet section are the same as per previous designs. After the testing procedure of printed it was observed that the spiraled design was successfully fabricated.

#### 4.5 TMA ANALYZER

The performed TA Q-400EM is helpful to acquire the  $T_g$  (glass-transition temperature) from their temperature modified dimension changes of the truncated cone layer. In TA-Q400EM, a three-point bending test was performed to address the storage modulus, loss modulus, stress relaxation, and stress-strain behaviour of the rectangular specimens. All dimensional change, storage modulus, and loss modulus experiments were performed for the temperature range of 40 °C using heating rates of 10 °C/min with 50 mL/min nitrogen purge gas flow and 0.02 N force. In the stress relaxation study,  $1 \times 10^{-3}$  N preloaded force was applied to straighten the specimen. During testing, the required temperature and 1% strain were applied, then relaxation modulus was evaluated with respect to time. Stress-strain experiments were performed in strain ramp mode with 0.02 N force and evaluated strain at 40 °C isothermal temperature.

The stress-strain analysis performed shown that the fabricated truncated cone is having a flexible property at a temperature of 40 °C (Fig 4.21).

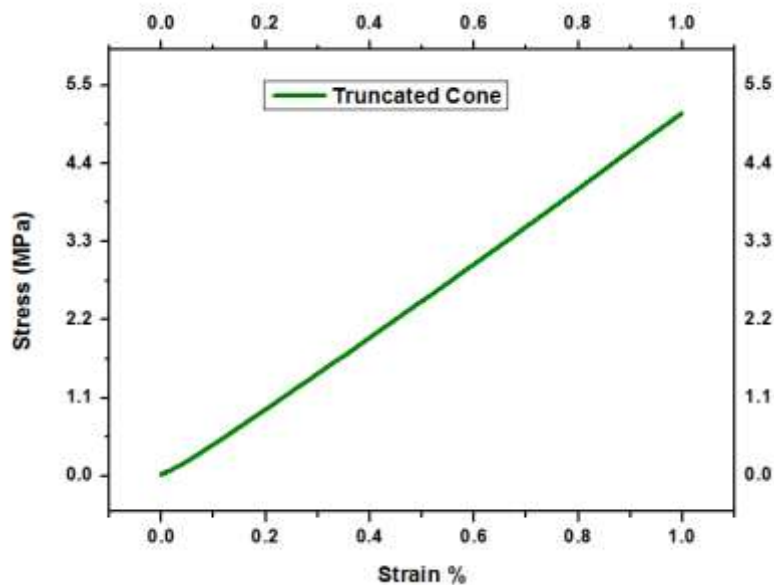


**Fig 4.21** Stress and strain analysis response

This flexibility shows that the part is durable and can be used for the required purpose.

## 4.6 CONCLUSION

The development of the device with reference to the available traditional column setup was a major concern. The purpose of designing a device was to use and implement 3D printing technology for water treatment applications. Here various design layouts were prepared using Solidworks software and then fabricated using the MiiCraft 3D printer. These printed devices were tested for their channels continuity formation and their adaptability. After all testing and finalization procedure, cylindrical structure and truncated cone was observed to better fit with the available filtration set up. The TMA analysis was also performed on the layer of the truncated cone to test its stress and strain bearing capacity and its response were appreciable. These final designs were further investigated for the removal of fluoride from water and discussed separately in Chapter 6 and Chapter 7.

## 4.7 REFERENCES

- Agarwala, S., Goh, G. L., Yap, Y. L., Goh, G. D., Yu, H., Yeong, W. Y., & Tran, T. (2017). Development of bendable strain sensor with embedded microchannels using 3D printing. *Sensors and Actuators A: Physical*, 263, 593-599.
- Bhagat, A. A. S., Kuntaegowdanahalli, S. S., & Papautsky, I. (2008). Enhanced particle filtration in straight microchannels using shear-modulated inertial migration. *Physics of Fluids*, 20(10), 101702.
- Daly, A. C., Pitacco, P., Nulty, J., Cunniffe, G. M., & Kelly, D. J. (2018). 3D printed microchannel networks to direct vascularisation during endochondral bone repair. *Biomaterials*, 162, 34-46.
- García-Sánchez, J., Solache-Ríos, M., Martínez-Miranda, V., Enciso-Perez, R., Arteaga-Larios, N., Ojeda-Escamilla, M., & Rodríguez-Torres, I. (2017). Experimental study of the adsorption of fluoride by modified magnetite using a continuous flow system and numerical simulation. *Process Safety and Environmental Protection*, 109, 130-139.
- Mohan, S., Singh, D. K., Kumar, V., & Hasan, S. H. (2017). Effective removal of Fluoride ions by rGO/ZrO<sub>2</sub> nanocomposite from aqueous solution:

- fixed bed column adsorption modelling and its adsorption mechanism. *Journal of Fluorine Chemistry*, 194, 40-50.
- Motaghi, H., Ziyadee, S., Mehrgardi, M. A., Kajani, A. A., & Bordbar, A.-K. (2018). Electrochemiluminescence detection of human breast cancer cells using aptamer modified bipolar electrode mounted into 3D printed microchannel. *Biosensors and Bioelectronics*, 118, 217-223.
- O'Neill, P. F., Ben Azouz, A., Vazquez, M., Liu, J., Marczak, S., Slouka, Z., Brabazon, D. (2014). Advances in three-dimensional rapid prototyping of microfluidic devices for biological applications. *Biomicrofluidics*, 8(5), 052112.
- Patel, R. K., & Awasthi, M. K. (2017). *Experimental Analysis of 3D Printed Microfluidic Device for Detection of Adulteration in Fluids*. Paper presented at the International Conference on Nano for Energy and Water.
- Patel, R. K., Chawla, A. K., Loulergue, P., Teychene, B., & Pandey, J. K. (2019). 3D printed microchannel loaded with hematite nanoadsorbent for fluoride removal from water. *Materials Letters*, 254, 190-193.
- Sharma, A., Mondal, S., Mondal, A. K., Baksi, S., Patel, R. K., Chu, W.-S., & Pandey, J. K. (2017). 3D printing: It's microfluidic functions and environmental impacts. *International Journal of Precision Engineering and Manufacturing-Green Technology*, 4(3), 323-334.
- Snyder, T. J., Andrews, M., Weislogel, M., Moeck, P., Stone-Sundberg, J., Birkes, D., Fercak, O. (2014). 3D systems' technology overview and new applications in manufacturing, engineering, science, and education. *3D Printing and Additive Manufacturing*, 1(3), 169-176.
- Tang, W., Liu, H., Zhu, L., Shi, J., Li, Z., Xiang, N., & Yang, J. (2019). Fabrication of Different Microchannels by Adjusting the Extrusion Parameters for Sacrificial Molds. *Micromachines*, 10(8), 544.
- Venkateswaran, P. S., Sharma, A., Dubey, S., Agarwal, A., & Goel, S. (2016). Rapid and automated measurement of milk adulteration using a 3D printed optofluidic microviscometer (OMV). *IEEE Sensors Journal*, 16(9), 3000-3007.

Zhang, W., Chai, Y., Xu, J., Liu, G., & Sun, Y. (2018). 3D heterogeneous wetting microchannel surfaces for boiling heat transfer enhancement. *Applied Surface Science*, 457, 891-901.

## CHAPTER 5

### SYNTHESIS AND CHARACTERIZATION OF ADSORBENT

*This chapter comprises a thorough summary of the procedures involved during adsorbent synthesis, and also addresses the characterization findings of adsorbents here.*

#### 5.1 DEFLUORIDATION ADSORBENTS

The chemical behaviour of a chemical species is determined by electronic chemical potential ( $\mu$ ) and chemical hardness ( $\eta$ ). Here  $\mu$  and  $\eta$  for chemical species are defined respectively as the first and second derivatives of the electronic energy of the ground state ( $E$ ) with respect to the number of electrons ( $N$ ) at constant external potential, represented by equations (5.1) and (5.2):

$$\mu = \left( \frac{\delta E}{\delta N} \right)_V \quad (5.1)$$

$$\eta = \left( \frac{\delta^2 E}{\delta N^2} \right) = \frac{1}{2} \left( \frac{\delta \mu}{\delta N} \right)_V \quad (5.2)$$

where  $V$ , the potential owing attraction of nuclei and other external forces.

The approximations for  $\mu$  and  $\eta$  can be determined by using the method of finite difference, where these parameters are related with ionization energy ( $I$ ) and electron affinity ( $A$ ) of the chemical species, equations (5.3) and (5.4):

$$-\mu \approx \frac{(1+A)}{2} = \chi \quad (5.3)$$

$$\eta \approx \frac{(1-A)}{2} \quad (5.4)$$

where  $\chi$ , absolute electronegativity which is the negative value chemical potential ( $-\mu$ ) (Alfarra, Frackowiak, & Béguin, 2004; Makov, 1995; Pearson, 1988, 1993; J.-L. Vigneresse, 2012; J. Vigneresse, Duley, & Chattaraj, 2011). The electron transfer enables the reaction occurrence of chemical species. Considering two reactant types, an acid (A) and a base (B) where the flow of electrons will be from the species of lower absolute  $\chi$  (the base) to that of higher  $\chi$  (the acid) until the electronic chemical potential ( $\mu$ ) becomes equal at equilibrium. For reactants A and B, their chemical potentials  $\mu_A$  and  $\mu_B$  after electron transfer between them, equations (5.5) and (5.6):

$$\mu_A = \mu_A^{\circ} + \eta_A \Delta N \quad (5.5)$$

$$\mu_B = \mu_B^{\circ} + \eta_B \Delta N \quad (5.6)$$

where,  $\mu_A^{\circ}$  and  $\mu_B^{\circ}$  are their neutral state chemical potentials and  $\Delta N$  is the number of electrons transferred. At equilibrium for the acid and base system equation (5.7);

$$\mu_A = \mu_B \quad (5.7)$$

therefore;

$$\Delta N = \frac{(\mu_B^{\circ} - \mu_A^{\circ})}{(\eta_A + \eta_B)} = \frac{(\chi_A^{\circ} - \chi_B^{\circ})}{(\eta_A + \eta_B)} \quad (5.8)$$

Equation (5.8) shows,

- Electron transfer process occurred due to difference in  $\chi$
- Resistance to the process defined by the sum of hardness

Therefore the chemical hardness of a system can be used for measuring the resistance to change in electronic configuration and together with the electronegativity it can be an indicator of chemical reactivity and stability (Alfarra et al., 2004; Makov, 1995; Pearson, 1988, 1993; J.-L. Vigneresse, 2012; J. Vigneresse et al., 2011).

Equation (5.8), gives the perception of hard-soft acid-basis (HSAB) concept. HSAB is one of the fundamental constructs in chemistry. The characteristic of hard acids and soft acids are defined through the HSAB concept. Hard acids

prefer to bind with hard bases forming ionic complexes, whereas soft acids prefer to bind with soft bases forming covalent complexes. From equation (5.8), a large number of electron transfer ( $\Delta N$ ) is present with soft acid and soft base that tends to form a covalent bond between them whereas hard acid and hard base have a small number of  $\Delta N$  that tend to form ionic bonding. These interactions result in the most stable interaction as well as these reactions are highly preferred (Makov, 1995; J. Vignerresse et al., 2011).

Fluoride is a hard base that shows that it would prefer to coordinate with hard acid. In this study, magnetic (hematite), metal oxide (titanium dioxide), and carbon-based (activated carbon) were synthesized in order to create hard surface sites for fluoride removal through the adsorption process from water in reference to HSAB model. A brief description of each adsorbent synthesis such as hematite, titanium dioxide, and activated carbon are discussed below along with their characterization analysis.

### 5.1.1 HEMATITE

Hematite is an iron oxide with a chemical composition of  $\text{Fe}_2\text{O}_3$ . A crystal structure of hematite is shown in Fig 5.1 where black and grey dots signify iron and oxygen respectively. Hematite is the most important ore of iron.

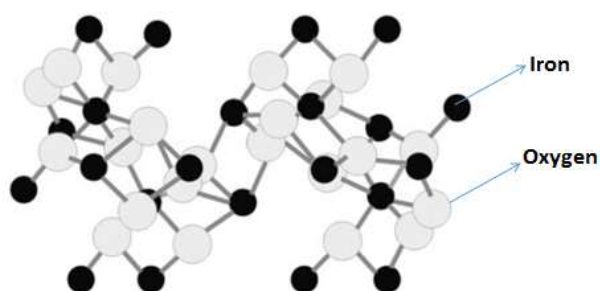


**Fig 5.1** Crystal structure of hematite (Teja & Koh, 2009)

Physically hematite has an extremely variable appearance. Its lustre can range from earthy to submetallic to metallic. Its colour ranges include red to brown and black to grey to silver. It occurs in many forms that include micaceous, massive, crystalline, botryoidal, fibrous, and others. In this study, hematite adsorbent was synthesized and tested for fluoride removal.



### 5.1.2 TITANIUM DIOXIDE

Titanium dioxide, also known as titanium (IV) oxide or titania, is the naturally occurring oxide of titanium, chemical formula  $\text{TiO}_2$ . Fig 5.2 shows lattice of anatase form of titanium dioxide,  $\text{TiO}_2$ . Oxygen atoms are coloured grey and titanium are black.  $\text{TiO}_2$  occurs in the form of minerals such as rutile and anatase (El Goresy et al., 2001). Rutile is the most abundant form of titanium dioxide which contains around 98% of titanium dioxide in the ore. The metastable anatase and brookite phases convert irreversibly to the equilibrium rutile phase upon heating above temperatures in the range 600–800 °C (1,110–1,470 °F) (Greenwood & Earnshaw, 2012).

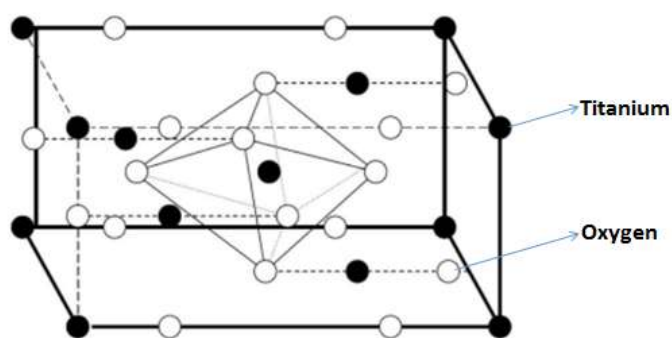


**Fig 5.2** Lattice of anatase form of titanium dioxide (Sørensen, 2014)

In this study, titanium dioxide adsorbent was synthesized and tested for fluoride removal.

### 5.1.3 ACTIVATED CARBON

Activated carbon is usually a form of carbonaceous material with an amorphous structure, the large specific surface area available for adsorption, and a high degree of porosity (Yahya et al., 2018). Activated carbon is generally formed from charcoal.

The major raw material utilized for activated carbon is any organic material with higher carbon content (coal, wood, jute fiber, coconut shells). The production of granular activated carbon media is performed by grinding the raw material, adding an appropriate binder to give it re-compacting, hardness, and then crushing into the correct size. The transformation of carbon-based

material into activated carbon is done by thermal decomposition inside the furnace by maintaining the required heat and atmosphere. In this study activated carbon was synthesized and investigated for fluoride removal efficiency.

These above adsorbents were selected depending upon their ease availability, better fluoride removal efficacy, regeneration capacity and reduction of possible environmental contamination.

## 5.2. SYNTHESIS OF ADSORBENTS

### 5.2.1 HEMATITE ADSORBENT

Hematite adsorbent was prepared using a chemical method as shown in Fig 5.3 where iron (III) nitrate nonahydrate and sodium hydroxide purchased from Sisco Research Laboratories Pvt. Ltd., India.

During the synthesis process 0.1 M solution of  $\text{Fe}(\text{NO}_3)_3 \cdot 9\text{H}_2\text{O}$  in distilled water was sonicated to form a clear solution (a). 1M solution of NaOH was separately prepared after 10 min of sonication (b). After neutralization of (a) through dropwise addition of (b), till it reached pH 7.5, the supernatant solution was separated and the precipitate was washed repetitively with distilled water in REMI centrifuge at 13,000 – 14,000 rpm.

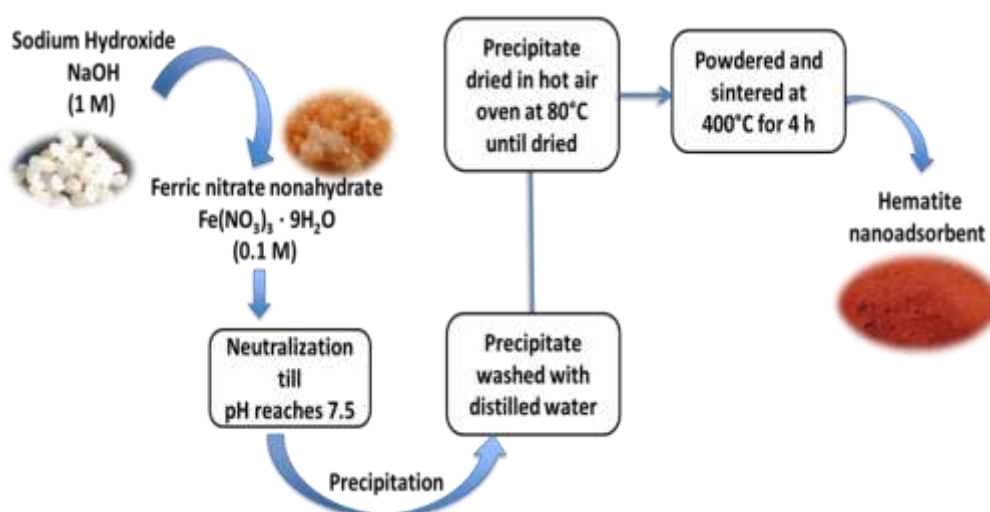


Fig 5.3 Hematite synthesis procedure

The prepared precipitate was dried in a hot air oven at 80°C until it gets completely dried. The material formed was then powdered and sintered at 400°C in a muffle furnace (Nabertherm B 180) for 4 hours.

### 5.2.2 TITANIUM DIOXIDE ADSORBENT

The sol-gel method is perhaps the most widely applied approach to prepare TiO<sub>2</sub> nanoparticles (Bagheri, Shameli, & Abd Hamid, 2012). The sol-gel method is based on hydrolysis of an alkoxide or halide precursor with subsequent condensation to the inorganic framework. The formation of TiO<sub>2</sub> from titanium (IV) alkoxide proceeds via an acid-catalyzed hydrolysis step followed by condensation.

Here TiO<sub>2</sub> adsorbent was synthesized through the sol-gel method (Fig 5.4) (Swapna & Haridas, 2016). The reagents used for the synthesis process were titanium tetra isopropoxide, isopropanol, and acetic acid purchased from Merck, India.

During the synthesis process 0.01M titanium tetra isopropoxide compound was dissolved in 0.26M isopropanol. This solution was kept at sonication for 10 minutes to form a clear solution. 0.035M of acetic acid was added to this clear solution and the process of sonication was further continued for 30 minutes. After proper mixing of mixture the mixture was converted to sol.

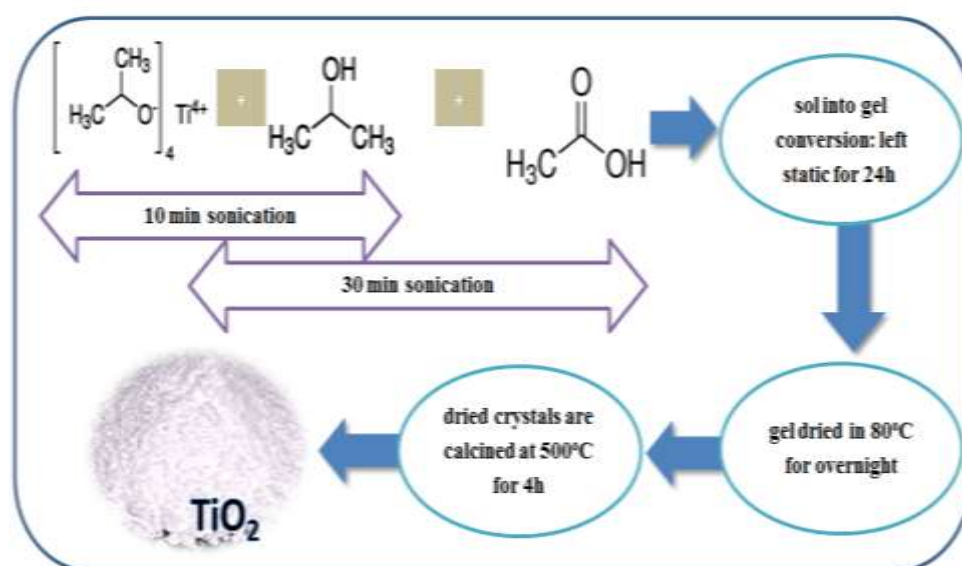


Fig 5.4 Titanium dioxide synthesis process

For sol to gel formation sol was kept static for 24 hours. The organic material present in the formed gel was evaporated through drying at 80 °C overnight. And finally the dried crystals were kept for calcination at 500 °C for 4 hours.

### 5.2.3 ACTIVATED CARBON ADSORBENT

For the synthesis of activated carbon (Fig 5.5), the organic material used here was jute fiber which was arranged from local sources Dehradun, India. The collected jute fiber was washed with double distilled water and dried at 60 °C. An amount of 100 g washed and dried jute fiber was chopped mechanically using a mixer grinder. The grinded jute fiber was then sieved using a mesh size range of 1 – 5 mm. The sieved jute fiber was further submerged in the 0.5 per cent solution of sodium hydroxide for around 12 h at room temperature. The process was then followed by proper washing ( 2- 3 times) of the jute fiber with double distilled water until the pH reached to a neutral state and then kept for drying at 110 °C. For thermal activation, dried jute fiber was further kept in a tubular furnace for 30 minutes heating at a temperature of 800 °C under the presence of high purity nitrogen (N<sub>2</sub>) environment.



**Fig 5.5** Activated carbon synthesis process using jute fiber

## 5.3 CHARACTERIZATION OF ADSORBENTS

### 5.3.1 HEMATITE

The detailed analysis of characterization results is summarized below for the synthesized adsorbent.

#### ✓ X-RAY DIFFRACTION ANALYSIS

The X-ray diffraction analysis of synthesized iron oxide adsorbent (Fig 5.6) contains eleven discrete peaks, these peaks obtained from diffraction corresponds to  $\alpha$ -Fe<sub>2</sub>O<sub>3</sub>. The major peaks of diffraction were detected at 25.03; 33.94; 36.50; 41.71; 50.25; 54.83; 58.33; 63.11; 64.63; 72.53 and 75.68° which resemble individually to the diffraction planes (112), (114), (210), (213), (224), (216), (118), (314), (300), (219) and (420). The data observed concords well with standard data of COD 9015065. The crystalline nature of the synthesized sample was shown by the formation of sharp peaks and the intensity of the peaks. The sample was completely decomposed to  $\alpha$ -Fe<sub>2</sub>O<sub>3</sub> as no peaks of Fe(OH)<sub>2</sub> were detected from XRD analysis.

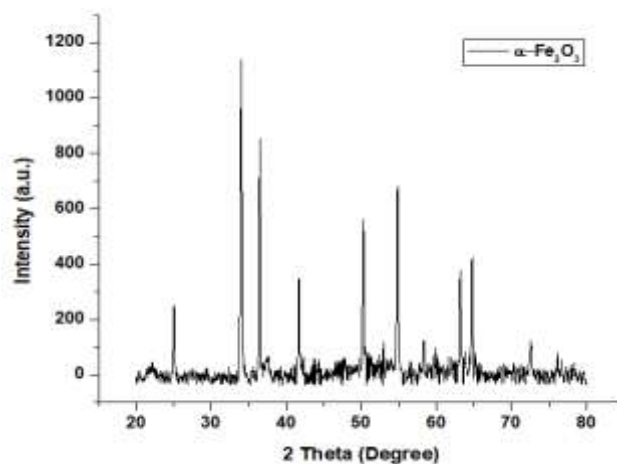


**Fig 5.6** X-ray diffraction of hematite

#### ✓ SCANNING ELECTRON MICROSCOPE ANALYSIS

The morphology of the  $\alpha$ -Fe<sub>2</sub>O<sub>3</sub> surface was observed by scanning electron microscope (Fig 5.7 (a), (b), (c), (d)). The SEM images obtained show the agglomerated shape morphology of the nanoparticles. The nanoparticles tend to agglomerate and develop larger assemblies due to their high surface energy.

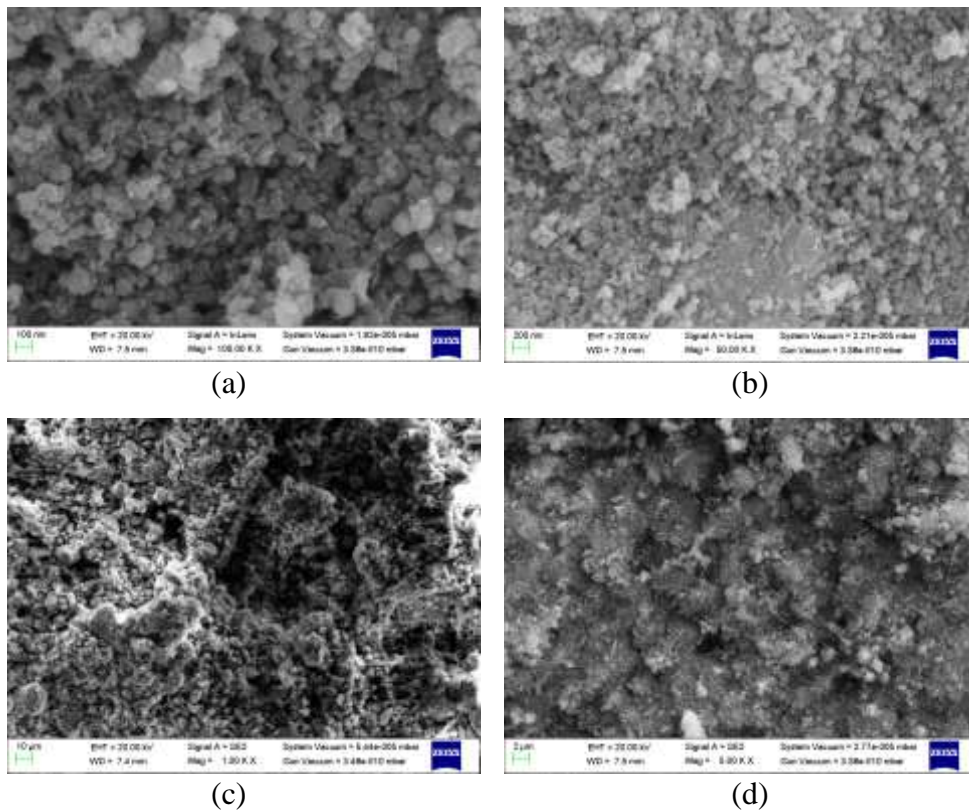


**Fig 5.7** (a), (b), (c) and (d) Scanning electron microscope images of  $\alpha$ -Fe<sub>2</sub>O<sub>3</sub> nanoparticles

Further, to analyze the composition of  $\alpha$ -Fe<sub>2</sub>O<sub>3</sub> nanoparticles, EDS spectra was recorded and is shown in Fig 5.8, the chemical composition in terms of atomic percentage (At %) and weight percentage (Wt %) for different elements are given in Table 5.1.

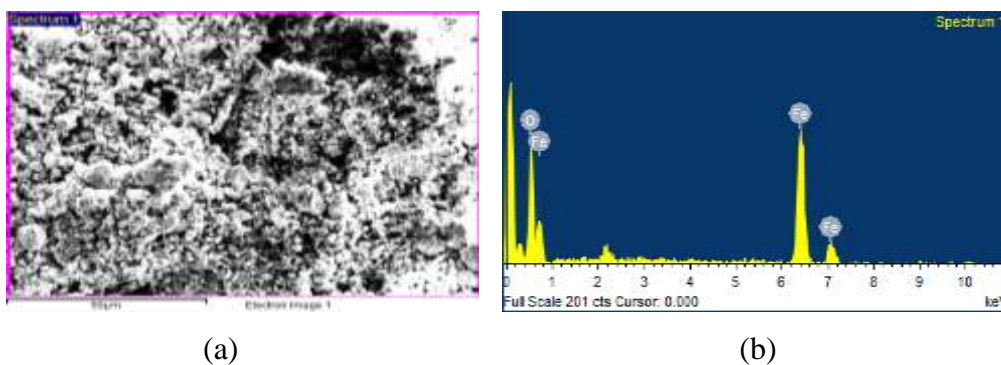


**Fig 5.8** EDS spectrum of  $\alpha$ -Fe<sub>2</sub>O<sub>3</sub> nanoparticles (a) showing the area considered for EDS while (b) showing the EDS pattern

EDS confirms the presence of iron and oxygen signals of iron oxide nanoparticles. This analysis showed the peaks that corresponded to the optical absorption of the produced nanoparticle.

**Table 5.1** Chemical composition of Fe<sub>2</sub>O<sub>3</sub> nanoparticles in terms of atomic percentage (At %) and weight percentage (Wt %) from energy dispersive spectra (EDS) measurement

Element	Weight percentage (Wt %)	Atomic percentage (At %)
O	33.73	63.98
Fe	66.27	36.02
Totals	100.00	100

#### ✓ BET ANALYSIS

The geometrical shape and porosity determine the specific surface area of the synthesized material. The surface area of the material was investigated with the nitrogen (N<sub>2</sub>) adsorption-desorption analysis. The N<sub>2</sub> adsorption-desorption isotherm is shown in Fig 5.9.

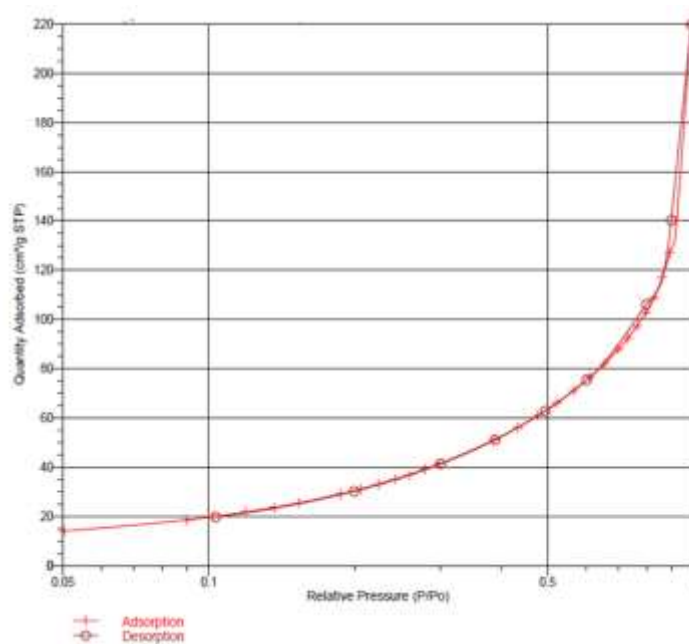


**Fig 5.9** N<sub>2</sub> adsorption/desorption isotherm on  $\alpha$ -Fe<sub>2</sub>O<sub>3</sub> nanoparticles

The isotherms obtained can be defined as type IV with an H3 hysteresis loop in accordance with the internal union of pure and applied chemistry (IUPAC) classification. The hysteresis loop was detected at relatively high pressure that is between 0.8 and 1. This shows that there is a presence of dilated pores on the prepared samples. The presence of a hysteresis loop in the isotherms is related with the secondary process of capillary condensation that results in the complete filling of  $P / P_0$  measures  $< 1$  (Kulkarni & Wachs, 2002). The hematite specific surface area determined from the BET surface area analyser was  $155.67 \text{ m}^2/\text{g}$  and the average particle size was found to be  $38.5409 \text{ nm}$ .

#### ✓ FOURIER TRANSFORM INFRARED SPECTROSCOPY

Fourier transform infrared (FTIR) spectra were used to analyse the bonds present in hematite. The FTIR spectra of hematite were shown in Fig 5.10. The peaks at  $3425$  and  $3429 \text{ cm}^{-1}$  are clearly showing the stretching vibration of lattice water and hydroxyl groups and those at  $1632$  and  $1633 \text{ cm}^{-1}$  are for  $\text{OH}^-$  bending vibration mode of adsorbed water molecules. The characteristic absorption bands (Fe-O bonds) occur at  $474$  and  $472 \text{ cm}^{-1}$ .

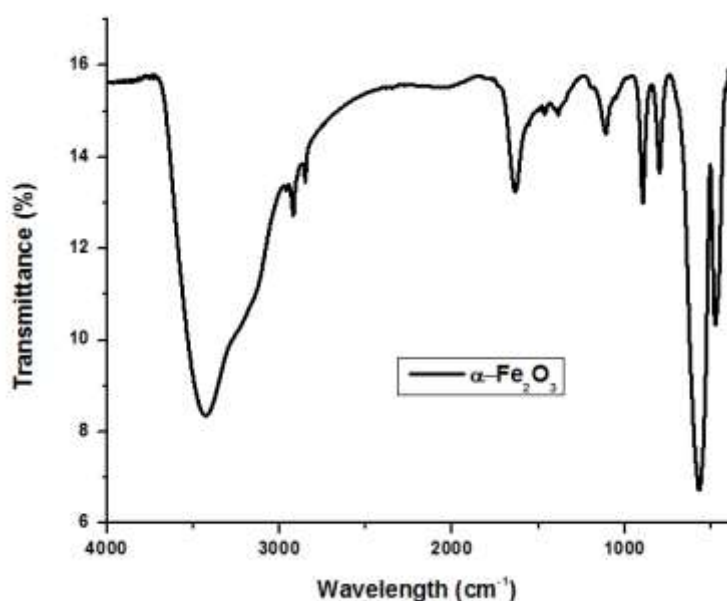


**Fig 5.10** FTIR of hematite adsorbent



### 5.3.2 TITANIUM DIOXIDE

The detailed analysis of characterization results is summarized below for the synthesized adsorbent.

#### ✓ X-RAY DIFFRACTION ANALYSIS

Fig 5.11 shows the X-ray diffraction analysis (XRD) patterns of calcined TiO<sub>2</sub> particles. Depending upon the XRD analysis result, the crystallite size and phase percentage of anatase and rutile can be determined (Chen, Yao, & Wang, 2008; Klug & Alexander, 1974). The XRD of the prepared titanium dioxide sample contains nine discrete peaks, these peaks obtained from diffraction corresponds to TiO<sub>2</sub>. The major peaks of diffraction were detected at 26.37; 38.90; 49.07; 54.88; 56.29; 63.62; 69.78; 71.31 and 76.05° which resemble respectively to the diffraction planes (101), (004), (200), (105), (211), (204), (116), (220), and (215). The data observed concords well with standard data of COD 1010942 which confirms the formation of the anatase phase of TiO<sub>2</sub>. The crystalline nature of the synthesized sample was shown by the formation of sharp peaks and the intensity of the peaks.

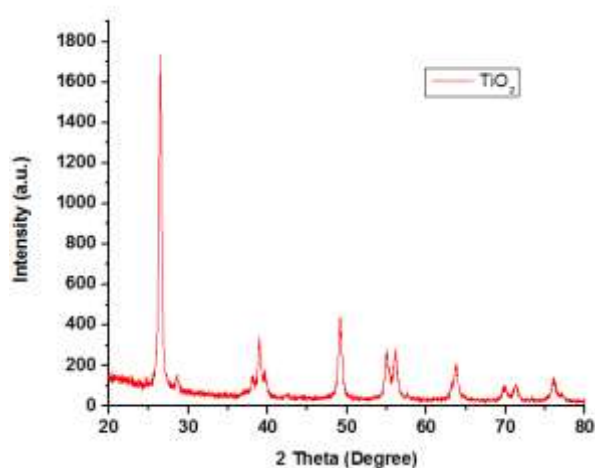


**Fig 5.11** XRD pattern of synthesized anatase TiO<sub>2</sub> nanopowder

#### ✓ SCANNING ELECTRON MICROSCOPE ANALYSIS

The scanning electron microscope (SEM) analysis was carried out for nanoporous TiO<sub>2</sub> to estimate its surface morphology. Fig 5.12 (a), (b), (c), (d) shows different SEM images of synthesized TiO<sub>2</sub> under varying

magnification. The SEM analysis shows the spherical morphology of TiO<sub>2</sub> nanoparticles along with clumped distribution.

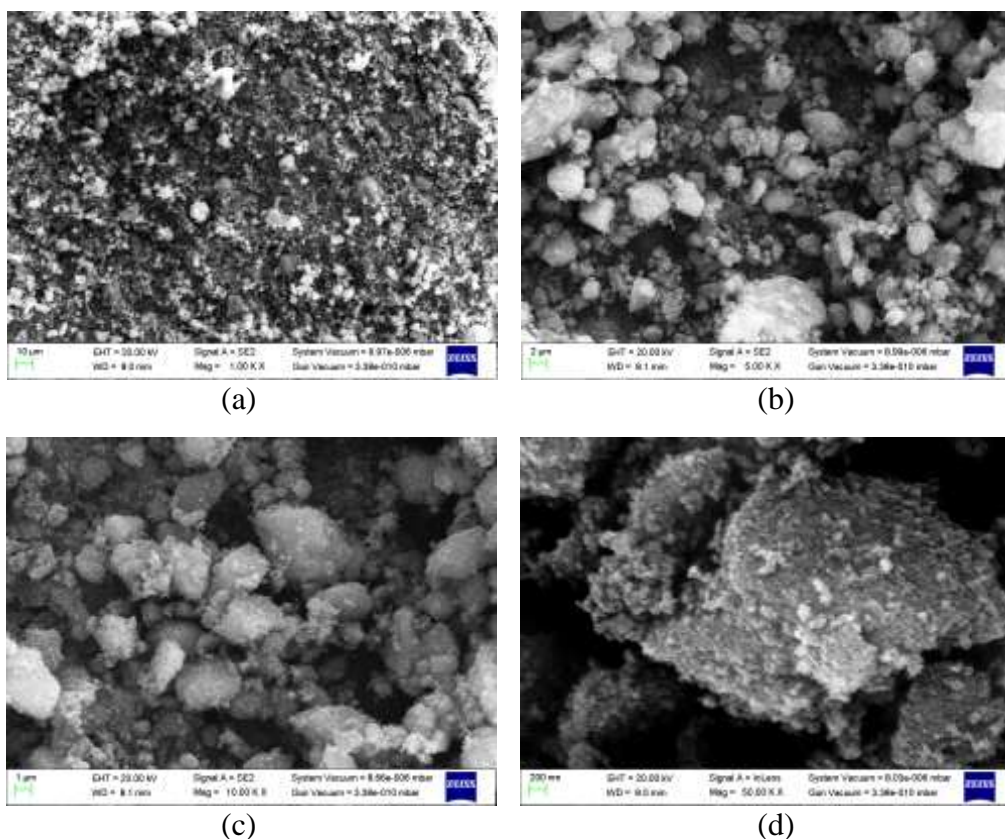


**Fig 5.12** (a), (b), (c) and (d) Scanning electron microscope images

Further, to analyse the composition of TiO<sub>2</sub> nanoparticles, EDS spectra was recorded and is shown in Fig 5.13, the chemical composition in terms of atomic percentage (At %) and weight percentage (Wt %) for different elements are given in Table 5.2.

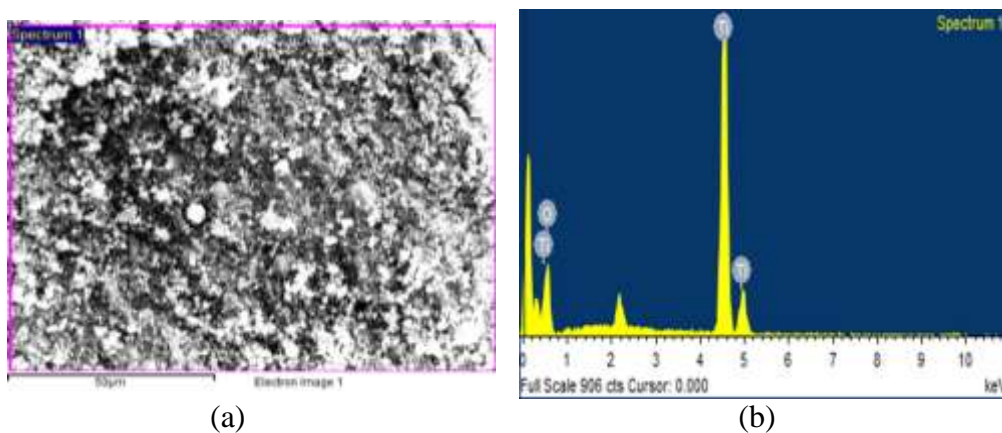


**Fig 5.13** EDS spectrum of TiO<sub>2</sub> nanoparticles (a) showing the area considered for EDS while (b) showing the EDS pattern

EDS confirms the presence of titanium and oxygen signals of titanium dioxide nanoparticle. This analysis showed the peaks that corresponded to the optical absorption of the produced nanoparticle.

**Table 5.2** Chemical composition of TiO<sub>2</sub> nanoparticles in terms of atomic percentage (At %) and weight percentage (Wt %) from energy dispersive spectra (EDS) measurement

Element	Weight percentage (Wt %)	Atomic percentage (At %)
O	49.97	74.94
Ti	50.03	25.06
Totals	100.00	100

#### ✓ BET ANALYSIS

The geometrical shape and porosity determine the specific surface area of the synthesized material. The surface area of the material was investigated with the nitrogen (N<sub>2</sub>) adsorption-desorption analysis.

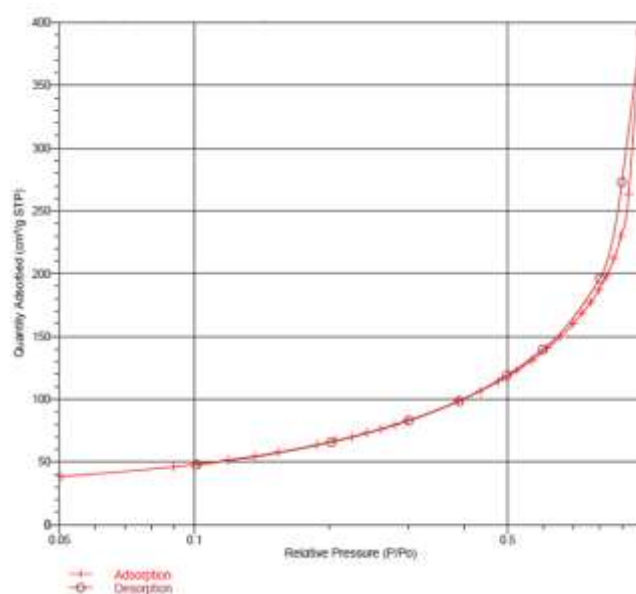


**Fig 5.14** N<sub>2</sub> adsorption-desorption isotherm of synthesized TiO<sub>2</sub> nanopowder

The N<sub>2</sub> adsorption-desorption isotherm is shown in Fig 5.14. It exhibits a type IV isotherm typical for the synthesized material (Kresge, Leonowicz, Roth,

Vartuli, & Beck, 1992). The specific surface area of the titanium dioxide determined from the BET surface area analyser was 281.36 m<sup>2</sup>/g and the average particle size was found to be 21.3248 nm.

#### ✓ **FOURIER TRANSFORM INFRARED SPECTROSCOPY**

Fig 5.15 shows the Fourier transform infrared (FTIR) spectrum of TiO<sub>2</sub> nanoparticles. From the FTIR spectrum of TiO<sub>2</sub> nanoparticles, Ti-O bending mode and de-formative vibration of Ti-OH stretching mode may be observed at 486.09 cm<sup>-1</sup> and 1622.59 cm<sup>-1</sup> respectively.

Asymmetrical and symmetrical stretching vibrations of the hydroxyl group (OH<sup>-</sup>) may be observed at 3256.49 cm<sup>-1</sup>. The band at 1622.59 cm<sup>-1</sup> may be attributed to water adsorbed on the TiO<sub>2</sub> surface (Chougala, Yatnatti, Linganagoudar, Kamble, & Kadadevarmath, 2017).

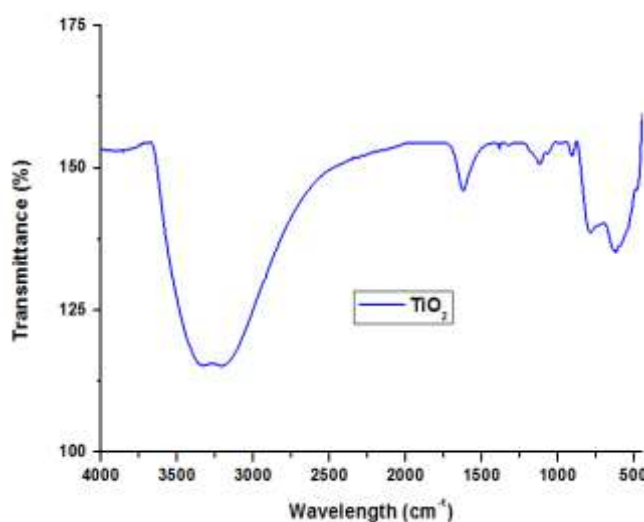


**Fig 5.15** FTIR spectrum of TiO<sub>2</sub> nanoparticle

#### **5.3.3 ACTIVATED CARBON**

The detailed analysis of characterization results is summarized below for the synthesized adsorbent.

#### ✓ **X-RAY DIFFRACTION ANALYSIS**

Fig 5.16 illustrates the XRD profile of the activated carbons. This activated carbon exhibit very broad diffraction peaks and the absence of a sharp peak reveals a predominantly amorphous structure.

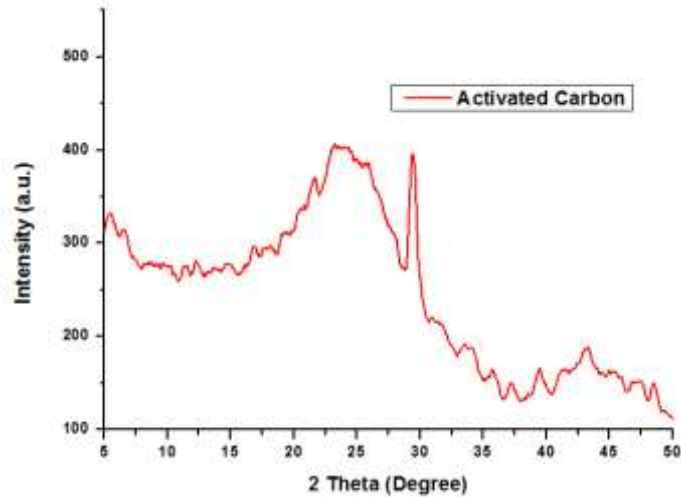


**Fig 5.16** XRD profile of activated carbon

The two major broad diffraction peaks were detected at 24 and 43° which resemble respectively to the diffraction planes (0 0 2) and (1 0 0). The appearance of the peak at around 24° at activation temperature (800 °C) signifies an increasing regularity of crystalline structure, which will result in a better layer alignment.

✓ **SCANNING ELECTRON MICROSCOPE ANALYSIS**

Fig. 5.17 (a) and (b) show the SEM morphology and images at a different magnification of the activated carbons prepared from jute fiber raw material through chemical activation using NaOH. The carbonization temperature of 800 °C was kept for the preparation of shown activated carbon in the figure.

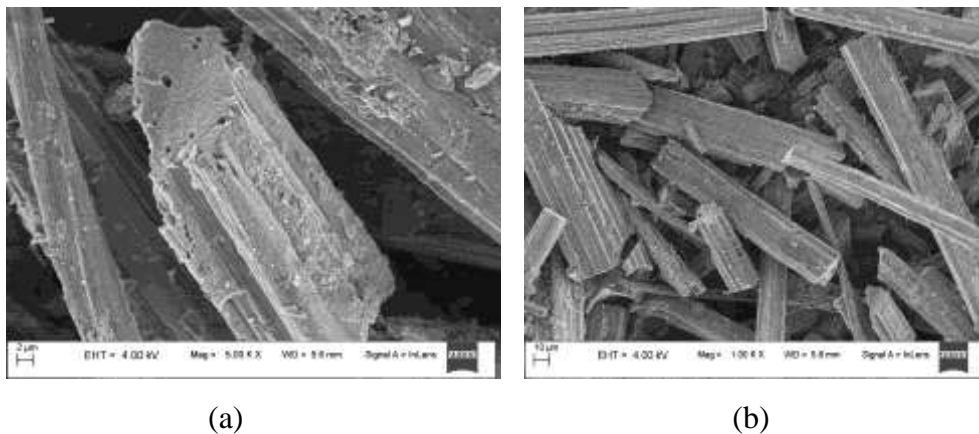


**Fig 5.17** (a) and (b) SEM photographs of activated carbons

### ✓ BET ANALYSIS

In BET analysis the information regarding the porous structure of the adsorbent is defined through adsorption isotherm. The N<sub>2</sub> adsorption/desorption isotherms curve for activated carbon is shown in Fig 5.18. The Type I isotherm is obtained for activated carbons. The Type I isotherm is associated with microporous structures according to the classification of IUPAC. When the relative pressure was less than 0.1 the major uptake occurred. The micropore filling is represented by the initial part of isotherm whereas the multilayer adsorption on the external surface was indicated by the lower slope of the plateau. Due to the limited uptake of N<sub>2</sub> signifying capillary condensation in the mesopores, the activated carbon shows a steep and discrete increase in adsorption at about P/P<sub>0</sub> ≈ 1.

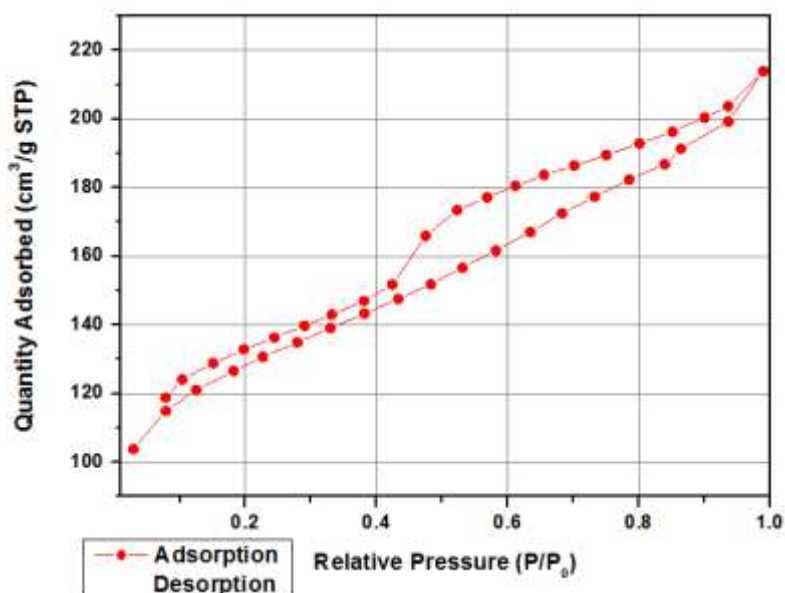


**Fig 5.18** N<sub>2</sub> Adsorption/desorption isotherms of activated carbon

The specific surface area of the activated carbon determined from the BET surface area analyser was 453 m<sup>2</sup>/g.

### ✓ FOURIER TRANSFORM INFRARED SPECTROSCOPY

Fig 5.19 shows the FTIR spectrum of activated carbon. The bands around 2892 – 2992 cm<sup>-1</sup> were observed and assigned for aliphatic groups stretching vibration.

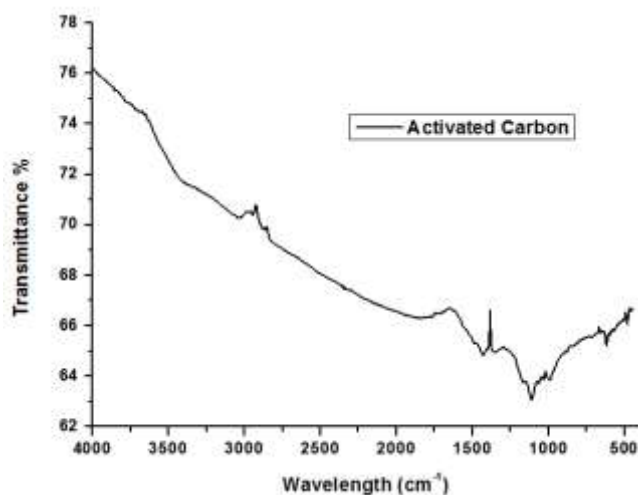


**Fig 5.19** FTIR spectrum of activated carbon

Small weak band appeared at  $2320\text{ cm}^{-1}$  is generally ascribed to symmetric or asymmetric stretching of aliphatic band in  $-\text{CH}$ ,  $-\text{CH}_2$  or  $-\text{CH}_3$ . The small band appearing around  $1700\text{ cm}^{-1}$  was attributed to carbonyl ( $\text{C}=\text{O}$ ) groups. The peaks at  $1434\text{ cm}^{-1}$  may be attributed to aromatic ring or  $\text{C}=\text{C}$  stretching vibration. The band around  $1111\text{ cm}^{-1}$  is typically attributed to  $\text{C}-\text{O}$  band. The last bands at  $990\text{ cm}^{-1}$  could be ascribed to  $\text{C}-\text{H}$  stretching vibrations.

#### 5.4 CONCLUSION

Considering the fluoride removal mechanism, three adsorbents magnetic (hematite), metal oxide (titanium dioxide) and carbon based (activated carbon) were synthesized successfully. These adsorbents were further characterized by XRD, SEM/EDS, BET, and FTIR. From the above study, it may be concluded that the synthesized hematite and titanium dioxide adsorbents were crystalline in nature whereas activated carbon showed amorphous nature. The average particle size of hematite and titanium dioxide adsorbents was observed to be  $38.5409\text{ nm}$  and  $21.3248\text{ nm}$  respectively. The BET surface area analysed for hematite was  $155.67\text{ m}^2/\text{g}$ , titanium dioxide was  $281.36\text{ m}^2/\text{g}$  and activated carbon was  $453.21\text{ m}^2/\text{g}$ . These adsorbents were used to remove fluoride from water and discussed separately in Chapter 6 and Chapter 7.

## 5.5 REFERENCES

- Alfarra, A., Frackowiak, E., & Béguin, F. (2004). The HSAB concept as a means to interpret the adsorption of metal ions onto activated carbons. *Applied Surface Science*, 228(1-4), 84-92.
- Bagheri, S., Shameli, K., & Abd Hamid, S. B. (2012). Synthesis and characterization of anatase titanium dioxide nanoparticles using egg white solution via Sol-Gel method. *Journal of Chemistry*, 2013.
- Chen, J., Yao, M., & Wang, X. (2008). Investigation of transition metal ion doping behaviors on TiO<sub>2</sub> nanoparticles. *Journal of Nanoparticle Research*, 10(1), 163-171.
- Chougala, L., Yatnatti, M., Linganagoudar, R., Kamble, R., & Kadadevarmath, J. (2017). A simple approach on synthesis of TiO<sub>2</sub> nanoparticles and its application in dye sensitized solar cells.
- El Goresy, A., Chen, M., Gillet, P., Dubrovinsky, L., Graup, G., & Ahuja, R. (2001). A natural shock-induced dense polymorph of rutile with  $\alpha$ -PbO<sub>2</sub> structure in the suevite from the Ries crater in Germany. *Earth and Planetary Science Letters*, 192(4), 485-495.
- Greenwood, N. N., & Earnshaw, A. (2012). *Chemistry of the Elements*: Elsevier.
- Klug, H., & Alexander, L. (1974). Qualitative and quantitative analysis of crystalline powders. In *X-Ray Diffraction Procedure for Polycrystalline and Amorphous Materials*: John Wiley and Sons New York, USA.
- Kresge, C., Leonowicz, M., Roth, W. J., Vartuli, J., & Beck, J. (1992). Ordered mesoporous molecular sieves synthesized by a liquid-crystal template mechanism. *nature*, 359(6397), 710-712.
- Kulkarni, D., & Wachs, I. E. (2002). Isopropanol oxidation by pure metal oxide catalysts: number of active surface sites and turnover frequencies. *Applied Catalysis A: General*, 237(1-2), 121-137.
- Makov, G. (1995). Chemical hardness in density functional theory. *The Journal of Physical Chemistry*, 99(23), 9337-9339.
- Pearson, R. G. (1988). Absolute electronegativity and hardness: application to inorganic chemistry. *Inorganic chemistry*, 27(4), 734-740.



- Pearson, R. G. (1993). The principle of maximum hardness. *Accounts of Chemical Research*, 26(5), 250-255.
- Sørensen, G. (2014). *Occurrence and effects of nanosized anatase titanium dioxide in consumer products*: Danish Environmental Protection Agency.
- Swapna, M. V., & Haridas, K. R. (2016). An easier method of preparation of mesoporous anatase TiO<sub>2</sub> nanoparticles via ultrasonic irradiation. *Journal of Experimental Nanoscience*, 11(7), 540-549.
- Teja, A. S., & Koh, P.-Y. (2009). Synthesis, properties, and applications of magnetic iron oxide nanoparticles. *Progress in crystal growth and characterization of materials*, 55(1-2), 22-45.
- Vignerese, J.-L. (2012). Chemical reactivity parameters (HSAB) applied to magma evolution and ore formation. *Lithos*, 153, 154-164.
- Vignerese, J., Duley, S., & Chattaraj, P. (2011). Describing the chemical character of a magma. *Chemical Geology*, 287(1-2), 102-113.
- Yahya, M. A., Mansor, M. H., Zolkarnaini, W. A. A. W., Rusli, N. S., Aminuddin, A., Mohamad, K., Ozair, L. N. (2018). *A brief review on activated carbon derived from agriculture by-product*. Paper presented at the AIP Conference Proceedings.

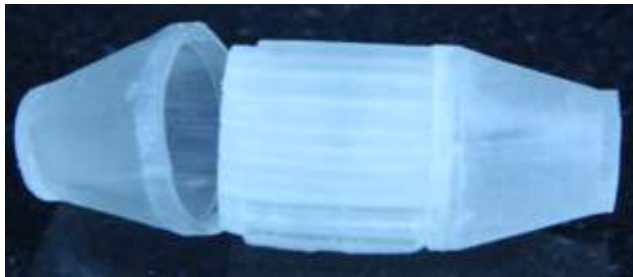
## CHAPTER 6

### DEFLUORIDATION MODEL EFFICIENCY

*This chapter describes the experimental procedure performed to study the defluoridation efficiency of the designed model. Here the designed model comprises a combination of both 3D printed model and synthesized fluoride removal adsorbent. It discusses the effect of the 3D printed device along with the loaded adsorbent and fluoride concentration.*

#### 6.1 DEFLUORIDATION MODEL

The 3D printed device as shown in Fig 6.1 was the final model printed as discussed in Chapter 4. The two separate models were printed having channel diameters of 1.5 mm and 2 mm respectively. These models have 35 numbers of microchannels in a circular pattern and the internal surface of the channel was kept plain.



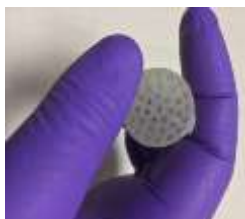
Pattern: Circular  
Channels: 35 Nos.  
Inside channel: Plain

Fig 6.1 Final 3D printed device

These microchannels were tested for their continuity after printing using a syringe where water was passed from every channel. Further to this continuity test these channels were loaded with synthesized adsorbent like hematite, titanium dioxide and activated carbon as discussed in Chapter 5.

The design was mainly divided into three parts:

Cylindrical structure



Inlet and outlet section



The other two sections inlet and outlet section were filled glass/cotton wool (Fig 6.2).



**Fig 6.2** Glass wool for packing

## 6.2 ADSORPTION STUDY

The subsequent concentration of 3, 6, and 10 ppm was prepared by the dilution of stock solution, using double distilled water. The pH and fluoride concentration of the solution before and after adsorption was monitored using an ion-selective meter (Thermo Scientific Orion Dual Star, pH/ISE meter). The solution was pipetted out in HDPE beakers for analysing fluoride. The ionic strength was adjusted using TISAB II (total ionic strength adjustment buffer) solutions (pH 5.0-5.5) before measuring the fluoride concentration. TISAB II solution was prepared by adding 4 g CDTA (trans-1, 2-diaminocyclohexane tetra acetic acid) together with 57 mL glacial acetic acid and 58 g sodium chloride (NaCl) and 37.5 g sodium hydroxide (NaOH) in 1000 mL in distilled water. Using a pH meter, pH was adjusted between 5 and 5.5 pH by adding 5M NaOH drop wise. Fluoride ion-selective electrode was calibrated using 1-100 mg/L of standard fluoride solutions to get a maximum slope. The electrode was calibrated with standard solutions of fluoride. The total ionic strength was adjusted using TISAB II solutions to get an optimum pH (5.0–5.5) for the measurement of fluoride concentration. The standard fluoride solution of 1.0, 2.0, 5.0, and 10 mg/L was used to calibrate the electrode. Before analysing fluoride concentrations in aqueous solution, the

fluoride ion-selective electrode was calibrated to ensure that the slope is obtained between 55-65 mV.

The quantity of adsorbed fluoride at service time in the exhausted channel

$$q_{t_e} \text{ in } \frac{\text{mg}}{\text{g}} = \frac{Q_v t_e C_o}{m}$$

where  $t_e$  is the service time in the exhausted channel (min),  $C_o$  is the inlet ion's initial concentration (mg/L),  $Q_v$  is the effluent volumetric flow rate (L/min), and  $m$  is the amount of adsorbent (g). Here the service time states the duration when the proposed system reaches to its threshold value.

The percentage of the fluoride adsorption onto the prepared adsorbent was estimated by the following expression as,

$$(\%) \text{ of fluoride removal} = \frac{C_o - C_e}{C_o} * 100$$

where  $C_o$  = Initial  $F^-$  ion concentration (ppm),  $C_e$  = Equilibrium  $F^-$  ion concentration (ppm).

The test temperature and pH range of the solution were 25°C and 7 respectively. The bends were resolved for test factors that included adsorbent dosage, flow rate, and fluoride concentration.

### 6.3 LEACH TEST

Leach tests were performed on treated water samples for the detection of heavy metals ions such as iron and titanium using ICP-OES (PlasmaQuant PQ9000, Analytik Jena) as the hematite and titanium dioxide adsorbent was used for the adsorption process. The operating conditions for the instrument to be maintained for performing analysis procedures are stated in Table 6.1.

**Table 6.1** Typical ICP-OES operating conditions

Particulars	Data
RF Power (W)	1200
Nebulizer gas (L/min)	1.50
Auxiliary gas (L/min)	0.50
Plasma gas (L/min)	12.0

Torch view	Axial
Torch material	Quartz

Fig 6.3 shows the sampling process to be performed for analysing heavy metals present in the treated water.

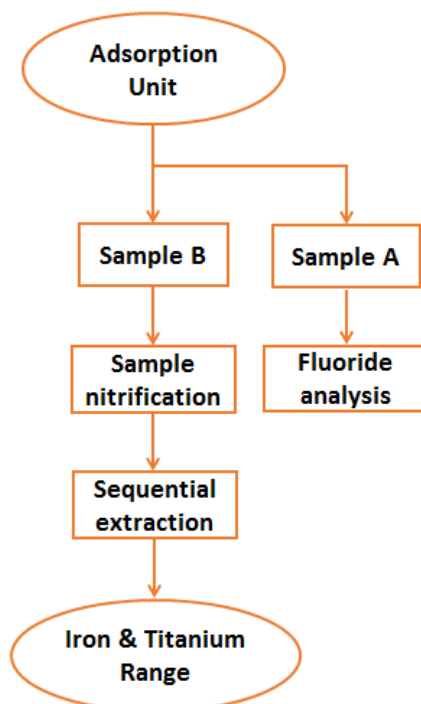


**Fig 6.3** Sampling process

#### **6.4 REGENERATION OF ADSORBENT**

The regeneration of the adsorbent used is an essential part of the removal of fluoride from water. The efficiency and cost of removal of fluoride depend on the regenerated adsorbent. Here, both acidic and basic medium has been used for the desorption study. For regeneration, all of the adsorbents considered for fluoride removal were performed.

#### **6.5 HEMATITE LOADED MODEL**

The synthesized hematite adsorbents were suspended in the double distilled water to form a thick paste solution that was poured in microchannels followed by drying in the oven at 40°C for 2 hrs and this process was repeated 5-7 times as shown in Fig 6.4.

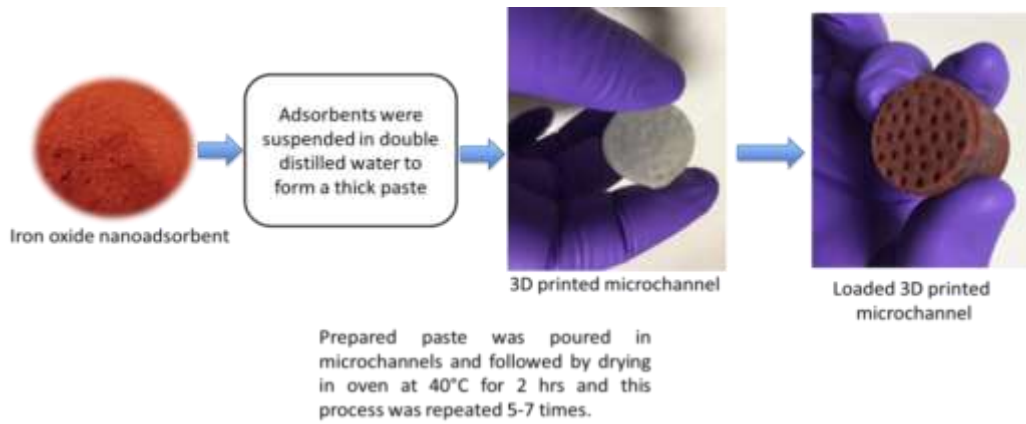


**Fig 6.4** Process for hematite adsorbent loading of 3D printed channel

Hereafter loading of a microchannel with adsorbent and glass wool packing of the inlet-outlet section is done as shown in Fig 6.5.



**Fig 6.5** Hematite loaded parts of the model

The different parts of the 3D printed device were assembled to form a defluoridation model (Fig 6.6 (a) and (b)).



(a)



(b)

**Fig 6.6** (a) Assembled parts of the device (b) Final assembly of the device with Hematite adsorbent

Each part of the device plays its own role during the fluoride removal process. Here the microchannel loaded with hematite adsorbent was acting for the adsorption of fluoride present in water. Inlet section and outlet section filled with glass wool act as a support to prevent the leaching of loaded adsorbent in the microchannel during the treatment process.

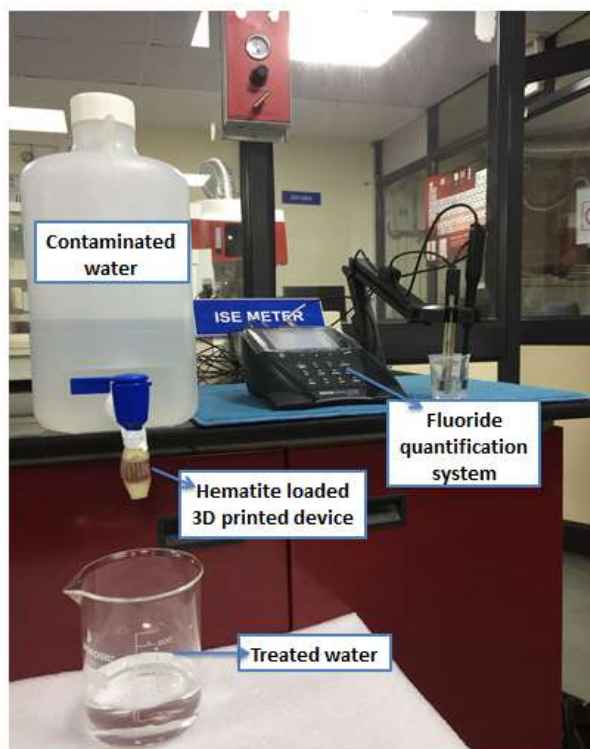


**Fig 6.7** Experimental set up for hematite loaded device

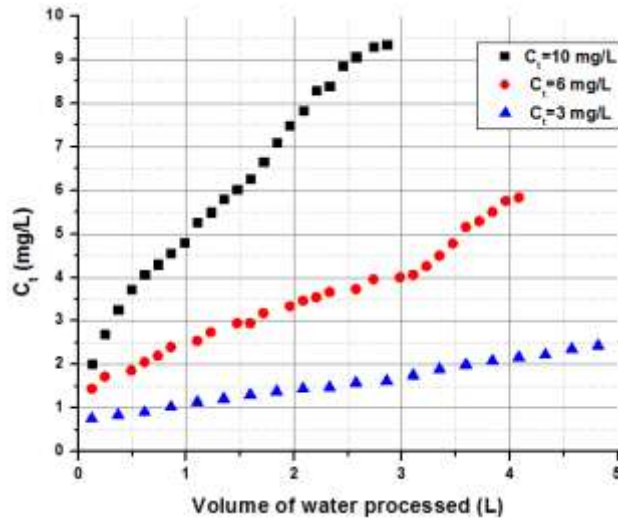
Fig 6.7 shows the hematite loaded 3D printed device was fitted to a 10 L aspirator bottle containing spiked water. The microchannels having 2 mm and 1.5 mm diameter are loaded with 4.0 g and 3.0 g of nano adsorbents respectively. The amount of dosage loaded in the microchannel was calculated as

Amount of loaded dosage

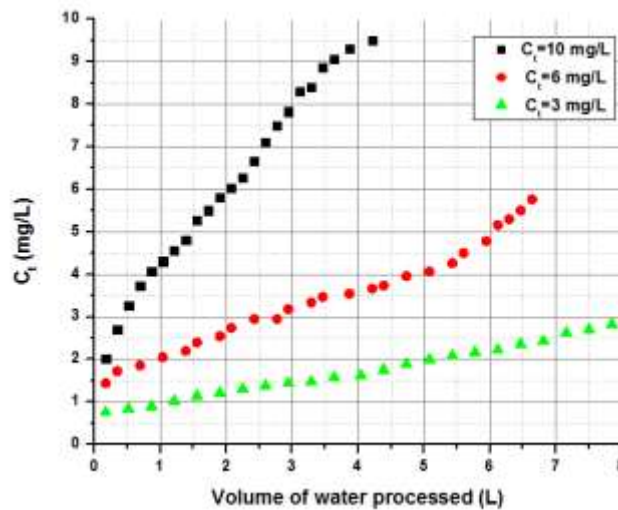
$$= \text{Loaded microchannel} - \text{unloaded microchannel}$$

These loaded microchannels were tested to study its efficiency in removing fluoride of different concentrations (3, 6, and 10 mg/L). The flow rate for the complete experimental process was obtained using

gravitational flow and overhead pressure due to which the flow was slow and continuous. The effect of varying fluoride concentration on the fluoride adsorption by iron oxide was studied. The bends attained at an adsorbent dosage of 3.0 g and 4.0 g along with a constant flow are presented in Fig 6.8 (a) and Fig 6.8 (b) respectively, where  $C_t$ , is the concentration of fluoride observed at different interval of time.



(a)



(b)

**Fig 6.8** Removal efficiency results of the process flow setup for Hematite adsorbent (a) 3g of adsorbent dosage loaded in 1.5 mm pore size channels (b) 4g of adsorbent dosage loaded in 2 mm pore size channels was tested for the 3, 6 and 10 mg/L of fluoride concentration



As the influent concentration increases from 3 to 10 mg/L, the bends become gradually sharper which indicates the decrease in exhaustion period with the increase in influent concentration. Similarly, the volume of water treated decreases as the inlet fluoride concentration increases from 3 to 10 mg/L. The greater influent concentration may have caused in the faster mass transfer of fluoride to iron oxide because of the greater concentration among the solution and iron oxide outward. Accordingly, at the high influent concentrations, iron oxide required less time to become saturated, resulting smaller exhaustion time (García-Sánchez, Solache-Ríos, Martínez-Miranda, & Morelos, 2013; Sarma & G. Bhattacharyya, 2016).

It should be mentioned that the developed prototype deals with the manual loading of adsorbents where the actual packing density could not be fixed. This condition of varying packing density shows the major effect in the output graph obtained for the removal of fluoride. Due to this variation the graph was plotted for the best result obtained.

Quantity of adsorbed fluoride at service time in the exhausted 2 mm pore size channel

$$q_{t_e} \text{ in } \frac{\text{mg}}{\text{g}} = \frac{Q_v t_e C_o}{m} = 2.47 \frac{\text{mg}}{\text{g}}$$

where  $t_e$  is the service time in the exhausted channel (min) = 3298 min,  $C_o$  is the inlet ion's initial concentration (mg/L) = 3 mg/L,  $Q_v$  is the effluent volumetric flow rate (L/min) = 0.001 L/min, and  $m$  is the amount of adsorbent (g) = 4 g.

The characterization of an adsorbent obtained after fluoride removal was performed. Fig 6.9 shows the comparison of XRD data for the adsorbent obtained before and after the removal of fluoride.

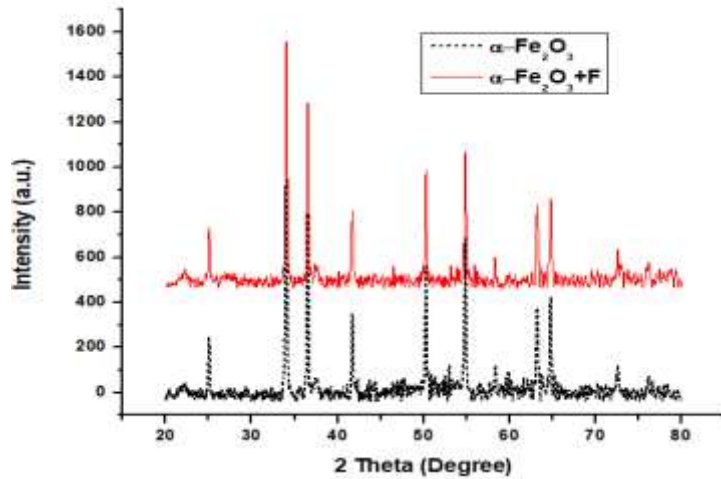


**Fig 6.9** XRD analysis before and after fluoride removal

The XRD data shows that there was no change in the spectrum. Fig 6.10 shows the FTIR of residues after filtration and shows the presence of fluoride bonding thanks to the appearance of bands around 1458 to 1467  $\text{cm}^{-1}$ .

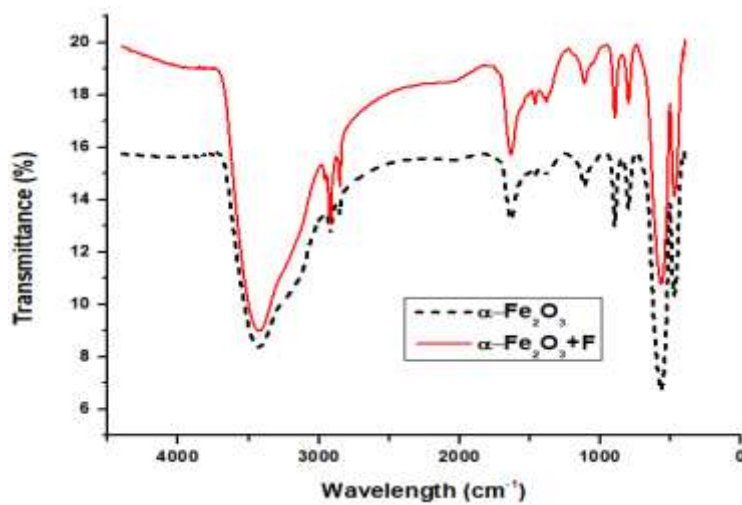


**Fig 6.10** FTIR analysis before and after fluoride removal

Table 6.2 shows the adsorption capacity comparison of diverse materials reported in the literature, along with the used hematite nanoadsorbent.

**Table 6.2** Comparison of adsorption capacity with Hematite adsorbent

<b>Adsorbent</b>	<b>Adsorption Capacity (mg/g)</b>
Hydrous Ferric Oxide (Nur et al., 2014)	6.71
Iron Oxide (Zhang, Li, Wang, Jiang, & Fok, 2017)	60.8
Modified magnetite (García-Sánchez et al., 2017)	1.86
Aluminum Modified Iron Oxides (García-Sánchez et al., 2013)	0.354
Magnesia-Pullulan Composite (Ye et al., 2018)	16.6
Hematite (This study)	2.47

### 6.5.1 LEACH TEST OF HEMATITE

The ICP – OES instrument was calibrated for iron metal ion from the range 0.001 ppm to 10 ppm using standard purchased from TCI Chemicals, India. The first run on the instruments for the blank data was done during the testing procedure, and it was done using double distilled water. Around 20 samples were tested to check the iron concentration range present in the treated water at regular intervals of time. As the presence of iron metal ions was not observed, the data obtained for the leach test showed that the glass wool packing was working efficiently.

### 6.5.2 REGENERATION OF HEMATITE

When the adsorption reaches equilibrium in a fluoride solution the loaded hematite adsorbent was collected in a beaker. This adsorbent was further dispersed in 0.1 M sodium hydroxide (NaOH) solution. The mixture was kept for 5 minute shaking process for fluoride desorption from the surface of the hematite adsorbent. After 5 minute shaking concentration range of fluoride in the solution was quantified using ion meter alongwith the regeneration efficiency. The calculated regeneration efficiency observed was around 91.65 per cent. The regenerated hematite adsorbent was collected after the desorption process performed in NaOH solution and followed by washing with 0.1 M HCl solution. Finally the washed hematite adsorbents were collected

and loaded in the microchannel for the fluoride removal process from water (Zhang et al., 2017).

## 6.6 TITANIUM DIOXIDE LOADED MODEL

For titanium dioxide ( $\text{TiO}_2$ ) loaded model the functioning of different parts of the model was the same as discussed for the hematite adsorbent loaded model. Here 4.0 g titanium dioxide adsorbent was loaded to the microchannel having 2 mm diameter. For loading of synthesized titanium dioxide adsorbent in the microchannel, the adsorbent was also suspended in the double distilled water to form a thick paste solution that was poured in microchannels followed by drying in the oven at  $40^\circ\text{C}$  for 2 hrs and this process was repeated 5-7 times as shown in Fig 6.11. The 2 mm pore size microchannel was selected here to study the fluoride removal efficiency, this preference was made due to the result obtained for the removal efficiency study for the hematite loaded adsorbent device having 2 mm pore size microchannel.

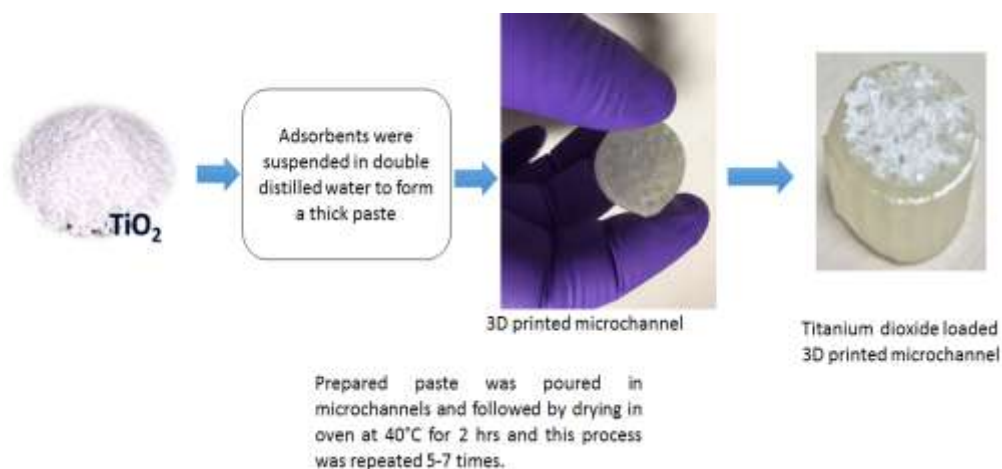


**Fig 6.11** Titanium adsorbent loading procedure for 3D printed channel

The adsorption capacity result for 2 mm pore size microchannel having 4 g adsorbent dosage was much better in comparison to 1.5 mm pore size microchannel having 3 g adsorbent dosage.

Hereafter loading of a microchannel with  $\text{TiO}_2$  adsorbent and proper glass wool packing in the inlet and outlet section was done as shown in Fig 6.12.



**Fig 6.12** Titanium dioxide loaded parts of the model

The filtration parts of the device were assembled to form a defluoridation setup (Fig 6.13 (a) and (b)). Here also the  $\text{TiO}_2$  loaded microchannels were tested to study the adsorption capacity of fluoride at different concentrations (3, 6, and 10 mg/L) and also the flow rate for the complete experimental process was obtained using gravitational flow and overhead pressure due to which the flow was slow and continuous. The effect of varying fluoride concentration on the fluoride adsorption by titanium dioxide was studied.



(a)



(b)

**Fig 6.13** (a) Assembled parts of the device (b) Final assembly of the device with Titanium dioxide adsorbent

The bends attained at an adsorbent dosage of 4.0 g along with a constant flow is shown in Fig 6.14. The effect observed was as the influent concentration increases from 3 to 10 mg/L, the bends become gradually sharper which indicates a decrease in exhaustion period with an increase in the influent concentration.

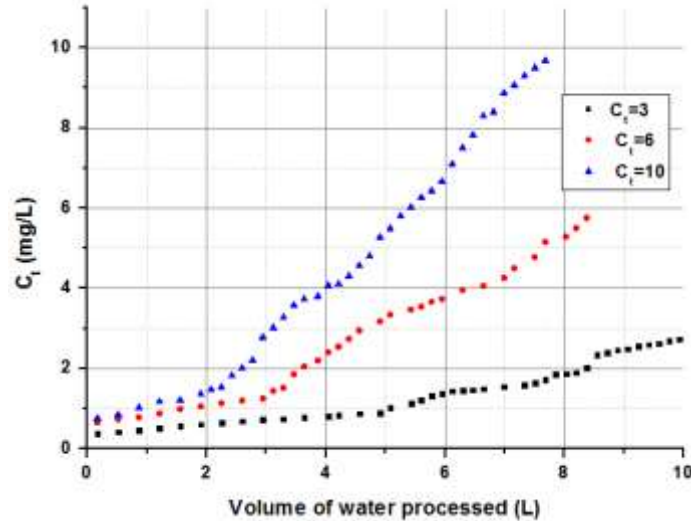


**Fig 6.14** Removal efficiency results for 4 g adsorbent loaded on 2 mm diameter channel for Titanium dioxide adsorbent

Similarly, the volume of treated water decreases as the inlet fluoride concentration increases from 3 to 10 mg/L. Due to the higher concentration between the solution and outward titanium dioxide, the greater influential concentration caused a faster mass transfer of fluoride to titanium dioxide. Accordingly, titanium dioxide required less duration to become saturated at high influential concentrations, resulting in a lower duration of exhaustion.

Quantity of adsorbed fluoride at service time in the exhausted channel

$$q_{t_e} \text{ in } \frac{\text{mg}}{\text{g}} = \frac{Q_v t_e C_o}{m} = 4.59 \frac{\text{mg}}{\text{g}}$$

where  $t_e$  is the service time in the exhausted channel (min) = 6121 min,  $C_o$  is the inlet ion's initial concentration (mg/L) = 3 mg/L,  $Q_v$  is the effluent volumetric flow rate (L/min) = 0.001 L/min, and  $m$  is the amount of adsorbent (g) = 4 g.

Table 6.3 shows the adsorption capacity comparison of diverse materials reported in the literature, along with the used titanium dioxide adsorbent.

**Table 6.3** Comparison of adsorption capacity with Titanium dioxide nanopowder

<b>Adsorbent</b>	<b>Adsorption Capacity (mg/g)</b>
TiO <sub>2</sub> -based composites (Liang, Xue, Gao, & Yang, 2017)	
SiO <sub>2</sub> -TiO <sub>2</sub>	152.2
Fe <sub>3</sub> O <sub>4</sub> -TiO <sub>2</sub>	22.9
Fe <sub>3</sub> O <sub>4</sub> -SiO <sub>2</sub> -TiO <sub>2</sub>	22.4
SiO <sub>2</sub> -TiO <sub>2</sub> (Zeng, Xue, Liang, & Zhang, 2017)	94.3
Titanium dioxide (This study)	4.59

### 6.6.1 LEACH TEST OF TITANIUM DIOXIDE

For the range of 0.001 ppm to 10 ppm of titanium metal ions using standard purchased from TCI chemicals, India, the ICP-OES instrument was calibrated to perform leach test. During the test procedure, the blank data was first to run on the instrument using double distilled water. Approximately 20 samples were tested regularly to check the concentration of titanium ions in the treated water. For a leach test, the data showed that the packaging was working with glass wool as a result of the inability to observe the presence of titanium metal ions in the treated water.

### 6.6.2 REGENERATION OF TITANIUM DIOXIDE

In a beaker, the TiO<sub>2</sub> adsorbent was collected after the adsorption in a fluoride solution reached equilibrium. In NaOH solution the adsorbent was re-dispersed at a fixed concentration (0.1 M) under proper shaking to desorb the fluoride from the surface of TiO<sub>2</sub> adsorbent. The efficiency of the regeneration and the concentration of fluoride in the solution were measured after 5 minutes. It was observed that the regeneration efficiency for 0.1 M NaOH was around 82.65 per cent for the next cycle of fluoride removal from water. These adsorbents were further re-collected and loaded into the microchannel for filtration purposes (Babaeiveli & Khodadoust, 2013).

## 6.7 ACTIVATED CARBON LOADED MODEL

In accordance to the loading of hematite and titanium dioxide adsorbent in the microchannel, the activated carbon was also suspended in the double distilled water to form a thick paste solution that was poured in microchannels followed by drying in the oven at 40°C for 2 hrs and this process was repeated 5-7 times. The functioning of printed parts for the filtration setup was the same as discussed for hematite and titanium dioxide adsorbent loaded model. The adsorption study performed for both hematite and TiO<sub>2</sub> shown better fluoride removal efficiency with a microchannel having a 2 mm pore size. Due to which the activated carbon adsorbent was also loaded to the microchannel having a 2 mm pore size. The volume of activated carbon was much higher in comparison with hematite and TiO<sub>2</sub> owing to which 1 g of activated carbon dosage was loaded in the microchannel.

Thus the loaded microchannels were evaluated to investigate their efficiency in removing fluoride from different concentrations (3, 6, and 10 mg/L), and the flow rate for the complete research procedure was acquired using gravitational flow and overhead pressure, resulting in a slow and continuous flow. The impact on fluoride adsorption by activated carbon adsorbent of varying concentrations of fluoride was analyzed. Figure 6.15 shows the bends achieved at an adsorbent dose of 1 g together through a constant flow.

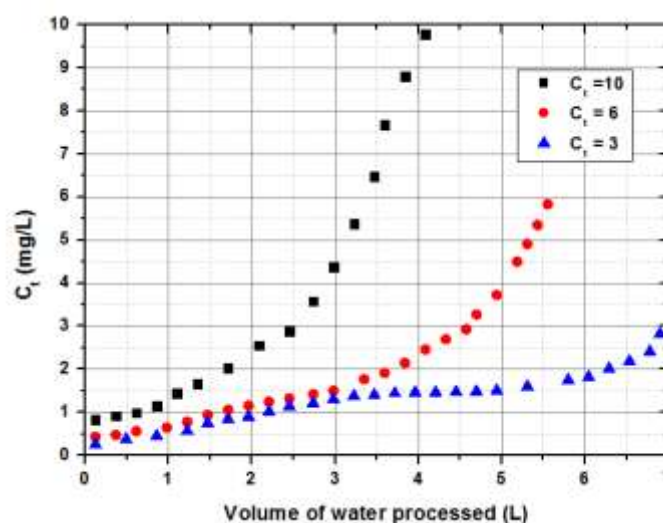


**Fig 6.15** Removal efficiency results for 1 g adsorbent loaded on 2 mm diameter channel for activated carbon adsorbent



As the influential concentration increases from 3 to 10 mg/L, the effect observed was that the bends gradually become sharper, which indicates a decrease in the exhaustion period with an increase in the influential concentration. Likewise the quantity of treated water decreases as the concentration of inlet fluoride rises from 3 to 10 mg/L. The higher influent concentration may have led to a faster transfer of fluoride to activated carbon due to the higher concentration between the solution and the activated carbon outward. As a result, at high influent concentrations, activated carbon required less time to become saturated, resulting in less exhaustion.

Quantity of adsorbed fluoride at service time in the exhausted channel

$$q_{t_e} \text{ in } \frac{\text{mg}}{\text{g}} = \frac{Q_v t_e C_o}{m} = 14.45 \frac{\text{mg}}{\text{g}}$$

where  $t_e$  is the service time in the exhausted channel (min) = 4818 min,  $C_o$  is the inlet ion's initial concentration (mg/L) = 3 mg/L,  $Q_v$  is the effluent volumetric flow rate (L/min) = 0.001 L/min, and  $m$  is the amount of adsorbent (g) = 1 g.

Table 6.4 shows the adsorption capacity comparison of diverse materials reported in the literature, along with the used activated carbon adsorbent.

**Table 6.4** Comparison of adsorption capacity with activated carbon adsorbent

<b>Adsorbent</b>	<b>Adsorption Capacity (mg/g)</b>
Palm shell activated carbon powder(PSAC)	117.3
Magnesium silicate (MgSiO <sub>3</sub> ) modified PSAC (Choong et al., 2020)	134.4
Coconut husk activated carbon (Talat et al., 2018)	6.5
Activated carbon (This study)	14.45

### **6.7.1 REGENERATION OF ACTIVATED CARBON**

After the adsorption attained equilibrium in a fluoride solution, the activated carbon adsorbent has been collected in a conical flask. To desorb fluoride from the adsorbent surface, the adsorbent was dispersed in a 10 mM hydrochloric (HCl) solution for a set time of continuous shaking. The concentration of fluoride in the solution was measured after the set time of shaking, and the efficiency of regeneration. The regeneration efficiency measured for 10 mM HCl solution treatment was about 94.56 per cent. To perform fluoride removal from water, the regenerated activated carbon adsorbents were further collected and loaded into the microchannel.

### **6.8 CONCLUSION**

The efficiency of fluoride removal was examined in 3D printed microchannel loaded with iron oxide, titanium dioxide, and activated carbon adsorbents. The experimental analysis clearly showed that the adsorption capacity of 2.47 mg/g for hematite adsorbent, 4.59 mg/g for titanium dioxide, and 14.45 mg/g for activated carbon adsorbent using the proposed system at lower concentration (3 mg/L). The device used to obtain these adsorption capacities was having a 2 mm diameter channel and adsorbent dosage of 4 g for hematite and titanium dioxide whereas 1 g for activated carbon. The leach test was also performed for the detection of heavy metals ions of iron and titanium in the treated water. The result attained shows that there was no occurrence of leaching during the treatment process.

### **6.9 REFERENCES**

- Babaeiveli, K., & Khodadoust, A. P. (2013). Adsorption of fluoride onto crystalline titanium dioxide: Effect of pH, ionic strength, and co-existing ions. *Journal of colloid and interface science*, 394, 419-427.
- Choong, C. E., Wong, K. T., Jang, S. B., Nah, I. W., Choi, J., Ibrahim, S., Jang, M. (2020). Fluoride removal by palm shell waste based powdered activated carbon vs. functionalized carbon with magnesium

- silicate: Implications for their application in water treatment. *Chemosphere*, 239, 124765.
- García-Sánchez, J., Solache-Ríos, M., Martínez-Miranda, V., Enciso-Perez, R., Arteaga-Larios, N., Ojeda-Escamilla, M., & Rodríguez-Torres, I. (2017). Experimental study of the adsorption of fluoride by modified magnetite using a continuous flow system and numerical simulation. *Process Safety and Environmental Protection*, 109, 130-139.
- García-Sánchez, J., Solache-Ríos, M., Martínez-Miranda, V., & Morelos, C. S. (2013). Removal of fluoride ions from drinking water and fluoride solutions by aluminum modified iron oxides in a column system. *Journal of colloid and interface science*, 407, 410-415.
- Liang, S., Xue, Y., Gao, B., & Yang, K. (2017). Removal of fluoride from aqueous solution by TiO<sub>2</sub>-based composites. *Journal of the Taiwan Institute of Chemical Engineers*, 74, 205-210.
- Nur, T., Loganathan, P., Nguyen, T., Vigneswaran, S., Singh, G., & Kandasamy, J. (2014). Batch and column adsorption and desorption of fluoride using hydrous ferric oxide: Solution chemistry and modeling. *Chemical Engineering Journal*, 247, 93-102.
- Sarma, A., & G. Bhattacharyya, K. (2016). Removal of fluoride from spiked water in the batch or static mode and also in the column or dynamic mode. *Desalination and Water Treatment*, 57(40), 19010-19024.
- Talat, M., Mohan, S., Dixit, V., Singh, D. K., Hasan, S. H., & Srivastava, O. N. (2018). Effective removal of fluoride from water by coconut husk activated carbon in fixed bed column: Experimental and breakthrough curves analysis. *Groundwater for Sustainable Development*, 7, 48-55.
- Ye, Y., Yang, J., Jiang, W., Kang, J., Hu, Y., Ngo, H. H., Liu, Y. (2018). Fluoride removal from water using a magnesia-pullulan composite in a continuous fixed-bed column. *Journal of Environmental Management*, 206, 929-937.
- Zeng, Y., Xue, Y., Liang, S., & Zhang, J. (2017). Removal of fluoride from aqueous solution by TiO<sub>2</sub> and TiO<sub>2</sub>-SiO<sub>2</sub> nanocomposite. *Chemical Speciation & Bioavailability*, 29(1), 25-32.

Zhang, C., Li, Y., Wang, T.-J., Jiang, Y., & Fok, J. (2017). Synthesis and properties of a high-capacity iron oxide adsorbent for fluoride removal from drinking water. *Applied Surface Science*, 425, 272-281.



Fluoride analysis reveals that there is no specific trend observed for the distribution of Fluoride. The maximum fluoride concentration has been observed at Barela (5.30 mg/L) Jabalpur district. In M.P, 91.59 per cent wells have been recorded fluoride concentration within the desirable limit of 1.0 mg/L whereas 2.42 per cent wells show fluoride concentration more than the maximum permissible limit of 1.5 mg/L. Fig 7.2 shows the highest level of fluoride concentration present in a particular district.

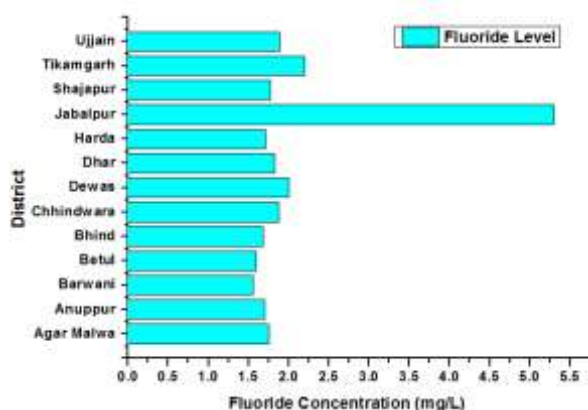


**Fig 7.2** Highest range of fluoride in each district of M.P

In this investigation, a real time application setup was installed for the removal of fluoride for groundwater. The location having high fluoride concentration was selected as per the CGWB report.

## 7.2 SYSTEM DEVELOPMENT

Fig 7.3 shows the developed setup to maintain the WHO permissible limit of fluoride in drinking water. The Jabalpur district, block Barela has been detected with a fluoride concentration of 5.3 mg/L and finalized for the investigation process.

The detailed description of the developed setup is as follows:

### A: GROUNDWATER

The primary (1.0 to 1000 mg/L) and secondary (0.01 to 10.0 mg/L) elements (cations/anions) that are present in groundwater are shown in Fig 7.4 (Project, September 1999). The major contaminants include heavy metals (Iron, Arsenic, Lead, Mercury, Chromium, Cadmium etc.), inorganic ions (Fluoride,

Nitrate, Chloride, Sulphate etc.) and colouring effluents (discharging from paper, textile and dye industry). These primary and secondary elements present in groundwater affects the efficiency of fluoride treatment process (Nabizadeh, Jahangiri-rad, & Sadjadi, 2015).

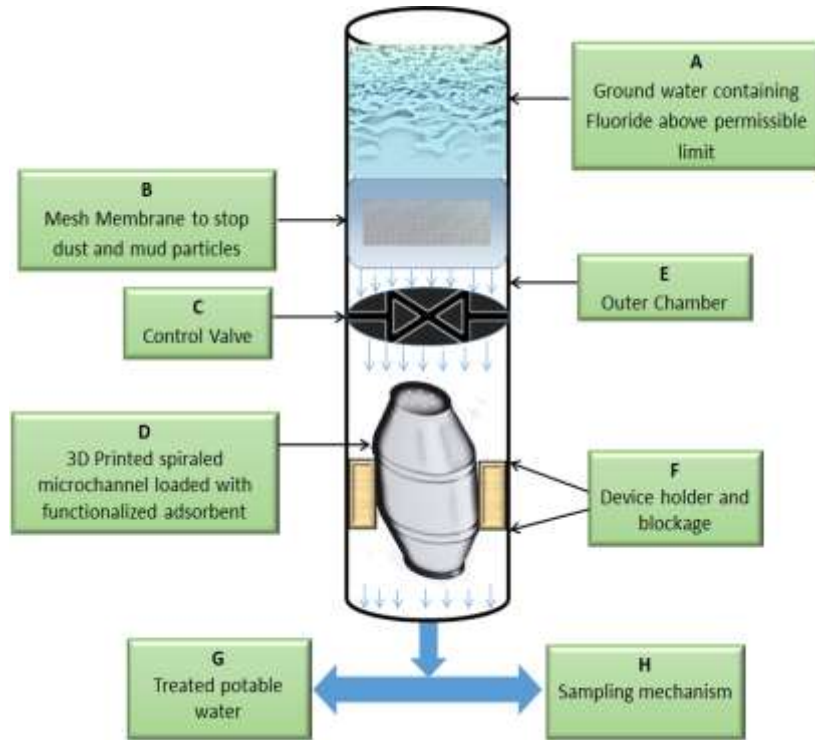


**Fig 7.3** Developed system for groundwater analysis

Groundwater consumption is, on average, the largest daily source of fluoride exposure for people who live in areas that add fluoride to the water. The consumption of fluorinated water should be avoided as it causes various health effects depending upon its concentration presence.

**B: MESH MEMBRANE**

Groundwater contains various impurities in the form of both large and small scales (Wiercik, Matras, Burszta-Adamiak, & Kuśnierz, 2016). To remove those impurities like dust and mud, mesh membrane is being used so that these impurities present can be separated before passing on towards a microchannel device. This separation of impurities would lead to a better filtration process.

### **C: CONTROL VALVE**

The flow of water after the separation of impurities is controlled using a control valve. Using this control valve a consistent flow is maintained to fall on the 3D printed device so that the treatment of fluoride present in water is properly done so as to reach its permissible limit.

### **D: 3D PRINTED SPIRALED MICROCHANNEL**

3D printed spiraled microchannel (Indian Patent Act, Application Number: 201911010347) having a 2 mm pore size is loaded with functionalized activated carbon adsorbent that has shown the capability to remove fluoride from water.

### **E: OUTER CHAMBER**

The outer chamber holds these subsections together and helps in performing the water treatment process.

### **F: DEVICE HOLDER**

The device holder fixes the fabricated 3D model at its point and also blocks the untreated water flow.

### **G: TREATED WATER**

After treatment procedure there are two outlets one is for treated water and another for sampling mechanism. The treated water gets collected in the collection chamber for drinking purposes.

### **H: SAMPLING MECHANISM**

In the sampling mechanisms the water quality is monitored to keep the record of fluoride concentration presence in drinking water after treatment.



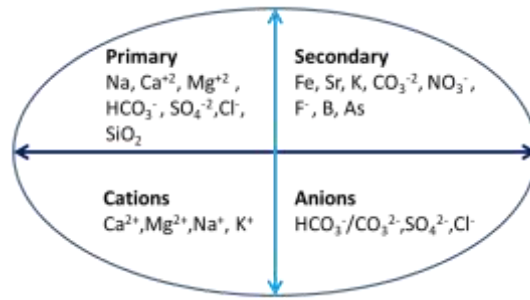


**Fig 7.4** Primary elements, secondary elements, major cations and anions in groundwater

### 7.3 FLUORIDE REMOVAL EFFICIENCY

The spiraled microchannel was fabricated and the activated carbon was synthesized as described in Chapter 4 and Chapter 5 respectively. The activated carbon was initially suspended for the loading process into double-distilled water, and then the paste was poured into the spiraled microchannels (Fig. 7.5). The process was followed by drying in the oven at 40 °C for 2 hours, which was repeated 5 to 7 times. A load of adsorbent was approximately 1 g, flow rate of 1mL/min and fluoride concentration of 5.3 mg/L.

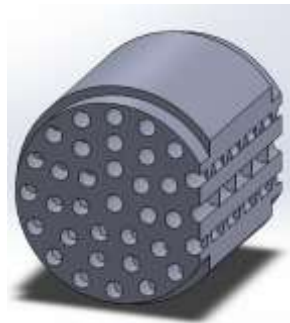


**Fig 7.5** Spiraled microchannel 3D model

The test analysis was performed and the result obtained is shown in Fig 7.6. From the attained curve it was observed the around 3.5 L of water could be treated using the developed setup.

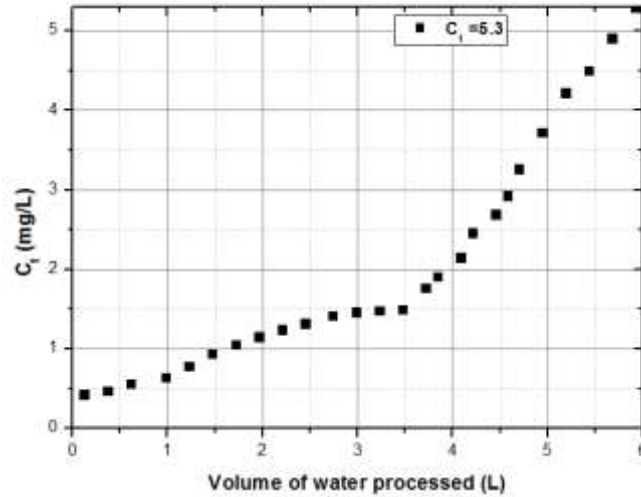


**Fig 7.6** Fluoride removal efficiency of spiraled microchannel

Quantity of adsorbed fluoride at service time in the exhausted channel

$$q_{t_e} \text{ in } \frac{\text{mg}}{\text{g}} = \frac{Q_v t_e C_o}{m} = 18.39 \frac{\text{mg}}{\text{g}}$$

where  $t_e$  is the service time in the exhausted channel (min) = 3470 min,  $C_o$  is the inlet ion's initial concentration (mg/L) = 5.3 mg/L,  $Q_v$  is the effluent volumetric flow rate (L/min) = 0.001 L/min, and  $m$  is the amount of adsorbent (g) = 1 g.

#### 7.4 WATER QUALITY QUANTIFICATION

To understand the water quality for drinking after the treatment process was followed by the quantification of some basic parameters such as pH, total dissolved solids (TDS), and Fluoride concentration level. The pH and TDS tests were performed onsite by using available electrode sensors. The pH level detected was 7.0, the TDS level was found to be 355 mg/L and the continuous fluoride concentration was measured using the ion-selective electrode discussed in Chapter 3 (SWDF, 2017).

#### 7.5 REGENERATION OF LOADED ADSORBENT

As discussed in Chapter 6, the adsorbent was collected in a beaker after adsorption had achieved equilibrium in a fluoride solution. The collected adsorbent was dispersed into a 10 mM hydrochloric (HCl) solution for a fixed

period of continuous shaking for fluoride desorption from the surface of the adsorbent. The fluoride concentration in the solution was measured after the shaking time and regeneration efficiency. For 10 mM HCl solution processing, the regeneration efficiency was approximately 90.23 per cent. The regenerated, adsorbents have been furthermore collected and loaded into the spiraled microchannel for the removal of fluoride from the water.

## 7.6 COST ANALYSIS

The real time setup was developed for treating fluoride containing water of concentration 5.3 ppm. The cost analysis was performed for the device upto 5 regeneration-reuse cycles of water purification (Table 7.1). The cost of water treated per litre was found to be 12.9 INR. In this calculation only materials cost for the preparation of device and the adsorbent was used. Other cost such as manpower, electricity, water use, capital cost and maintenance cost is not included, due to inadequate data.

**Table 7.1** Cost calculation for laboratory prototype

Particular	Parameters	Cost (INR)
3D Device	1 unit	220
Activated carbon	1 g	0.15
Adsorbent Regeneration	5 cycles	6
Water Purification Cost (Initial Fluoride Concentration = 5.3 ppm)	Per Litre	12.9

## 7.7 CONCLUSION

The developed system has shown the potential for the real time application. The setup successfully separated the dust particle at the mesh membrane stage. Further the treatment of fluoride concentration level of 5.3 mg/L using 1 g activated carbon dosage was performed and found that the adsorption capacity was around 18.39 mg/g. The volume of treated water obtained was about 3.5 L. The selection of activated carbon for real time application was done due to

its fluoride removal efficiency observed in Chapter 6 and also the regeneration efficiency of the adsorbent.

## 7.7 REFERENCES

- CGWB. (2018). *Ground Water Year Book - Madhya Pradesh*.
- Nabizadeh, R., Jahangiri-rad, M., & Sadjadi, S. (2015). Modelling the effects of competing anions on fluoride removal by functionalized polyacrylonitrile coated with iron oxide nanoparticles. *South African Journal of Chemistry*, 68(1), 201-207.
- Project, H. (September 1999). *Major Ions in Water*. Retrieved from New Delhi:
- SWDF. (2017). TDS and PH. Retrieved from <https://www.safewater.org/factsheets-1/2017/1/23/tds-and-ph>
- Wiercik, P., Matras, K., Burszta-Adamiak, E., & Kuśnierz, M. (2016). Analysis of the properties and particle size distribution of spent filter backwash water from groundwater treatment at various stages of filters washing. *Inżynieria i Ochrona Środowiska*, 19.

## CHAPTER 8

### CONCLUSION AND RECOMMENDATION

*This chapter outlines the findings drawn from various studies and recommendations for further scope of research made in this dissertation.*

#### 8.1 CONCLUSION

Fluoride is a micro nutritional component, essential for both teeth and skeletal growth. If the concentration of fluoride intake increases above 1.5 mg/L, it causes various health problems such as dental and skeletal fluorosis. Among the different processes used to eliminate fluoride from water, adsorption technology seems to be the easiest mode to maintain the required concentration of fluoride in water as per WHO guidelines. In order to accomplish this, advancement in 3D printing technology was integrated with the available adsorption technology for the removal of fluoride from water. In recent years various adsorbents have shown their better potential for the removal of anionic constituents from water. The better adsorption capacity of these adsorbents was due to the high surface area available for the removal process. In this study a 3D model was successfully fabricated using the MiiCraft 3D printer that was divided into three parts: (i) inlet section, (ii) cylindrical structure, and (iii) outlet section. The cylindrical structure consists of two variants (a) plain microchannel device having 1.5 mm and 2 mm pore size and (b) spiraled microchannel of 2 mm pore size. The printer used here works on stereolithography (SLA) technology which belongs to the vat photopolymerization family. These printed microchannels were loaded with three different synthesized fluoride removal adsorbents at lab scales such as hematite, titanium dioxide, and activated carbon to study their adsorption efficiency. To understand the successful synthesis of adsorbent these adsorbents were characterized comprehensively using X-ray diffraction (XRD), Scanning electron microscope (SEM)/ Energy dispersive X-ray

Spectrometry (EDS), Brunauer-Emmett-Teller (BET) and Fourier transform infrared spectroscopy (FT-IR) and finally the characterization results have shown that the adsorbents required were prepared successfully. After the successful printing of the 3D model and loading of synthesized adsorbent the adsorption capacity of the setup was evaluated. The adsorption capacity of 2.47 mg/g for hematite adsorbent, 4.59 mg/g for titanium dioxide, and 14.45 mg/g for activated carbon adsorbent were observed using the proposed lower-concentration system (3 mg/L). The device used to achieve this adsorption capacity had a microchannel of 2 mm in diameter and a 4 g adsorbent dose for hematite and titanium dioxide, whereas 1 g for activated carbon. During the leaching test of treated water ICP-OES was used to detect heavy metals. The result obtained indicated that no harmful chemicals were detected in leachate. Finally, the spiraled microchannel device with a pore size of 2 mm was loaded with 1 g of activated carbon and 5.3 mg/L of fluoride containing water was passed through the system for real time application. The observed adsorption capacity for this setup was about 18.39 mg/g. The economical evaluation for the laboratory based single device was calculated for 5 regeneration-reuse recycles. The estimated value for producing per litre of purified water was 12.9 INR.

The overall developed process was promising for developing a 3D printing technology based device, integrated with the existing fluoride removal adsorption technology for obtaining the fluoride containing water as per WHO guidelines. The developed process is relatively economic, ease to use and technically comparable to the available traditional alternatives. However, more detailed investigation is necessary to establish its feasibility in large scale water treatment.

## **8.2 RECOMMENDATIONS**

Recent results in this study have provided a great outcome with respect to 3D printing applications integrated with the adsorbent for the removal of fluoride from water.

Following are a few recommendations for further scope of research:

- ✓ Adaptive 3D printed model for water treatment at a small scale in the continuous treatment process.
- ✓ Reusability of the 3D printed model in order to reduce the resin wastage.
- ✓ Evaluation for the aging of 3D printed device in water.
- ✓ For better fluoride removal efficiency the low-cost green adsorbents require exploration.
- ✓ Hydraulic characterization for 3D printed developed model.
- ✓ Automated system development for the uninterrupted water treatment process.
- ✓ Investigation on the combination of the available water treatment techniques being used for water treatment with the advanced 3D printing technology.
- ✓ During the treatment process a huge amount of sludge was formed, a proper disposal strategy for sludge is a major concern for the environment.
- ✓ Regeneration of adsorbents with other eluents.

## CURRICULUM VITAE

**RAVI KUMAR PATEL**

**S/O:** Lal Bahadur Patel

**Address:** NH-3, B-247, NTPC Colony, Vindhya Nagar, Dist. Singrauli (M.P),  
India, 486885

**Email ID:** ravikumarpatel28@gmail.com, Mobile No: (+91)-7805820939

**Date of Birth:** January 28, 1990

**Nationality:** Indian

**Academic Qualification:** B.E. in Electronics and Communication Engineering from LNCT, Indore, Rajiv Gandhi Proudyogiki Vishwavidyalaya in 2011 and M.Tech in Robotics Engineering from University of Petroleum and Energy Studies, Dehradun.

### INTERNATIONAL EXPOSURE

(Oct 2016 – May 2018)

**Project Title:** SwachhNeer - Une Vie Meilleure: Combating Water Issues Through Indo-French Networking (IFWN/2015/1)

**Funded by:** Indo-French Centre for the Promotion of Advanced Research (IFCPAR), Department of Science & Technology, Government of India and the Ministry for Europe & Foreign Affairs, Government of France

- ✓ Development of a water network between India and France
- ✓ Evaluation of the feasible in-house technology developed by collaborators from France for treating drinking water
- ✓ Specific contaminants evaluation through analysis of available water resources both in France and India
- ✓ Data collection of the water quality and water quantity present both in India and France
- ✓ Scholarship received by IFCPAR, Government of India for travel to France
- ✓ Primary, secondary data analysis, working experience on various data base for data collection, data presentation to government agencies and report writing and submission to Government of India
- ✓ **International visit to France Universities**
  - ❖ University of Poitiers: 11<sup>th</sup> until 15<sup>th</sup> September 2017 with Dr. B.Teychene
  - ❖ University of Rennes: 18<sup>th</sup> until 21<sup>th</sup> September 2017 with Dr. P. Loulergue & Pr. A. Szymczyk

### PATENT (03)

- ✓ Alterable and Effectual Microchannel Rapid Prototyping for Removal of Toxic Effluent from Water through Adsorption onto Nano-adsorbent (Application Number: 201911010347)
- ✓ A Biomass Stove (Application Number: 201911011348)
- ✓ Patient Health Monitoring & Tracking System (Application Number: 201611039333)



**PUBLICATION / SEMINAR / CONFERENCE**

**A. International Journal**

Title	Authors	Journal/DOI
1. 3D printed microchannel loaded with hematite nanoadsorbent for fluoride removal from water	<b>Ravi Kumar Patel</b> , Amit Kumar Chawla, Patrick Loulergue, Benoit Teychene and Jitendra K. Pandey	Materials Letters; 254 (2019): 190-193, <i>IF: 3.019</i>
2. Elimination of Fluoride, Arsenic and Nitrate from water through adsorption onto nano-adsorbent: A Review	<b>Ravi Kumar Patel</b> , Sanjay Kumar, Amit Kumar Chawla, Prasenjit Mondal, Neelam, Benoit Teychene, Jitendra K. Pandey	Current Nanoscience; 15.6 (2019): 557-575, <i>IF: 1.586</i>
3. A Review On Visual Odometry Techniques For Mobile Robots: Types And Challenges	Vikas Thapa, Abhishek Sharma, Beena Gairola, Amit Kumar Mondal, Vindhya Devalla, <b>Ravi Kumar Patel</b>	Recent Advances in Electrical and Electronic Engineering; 13.5 (2020)
4. Biodiesel Wastewater Treatment and Power Generation using Earthen Membrane Microbial Fuel Cell	Debajyoti Bose, Deepali Yadav, <b>Ravi Kumar Patel</b> , Anubhav Dhoundiyal, Laxman Gusain and Anubhav Tyagi	Nature, Environment and Pollution Technology; 17.4 (2018): 1293-1297
5. Internet of Things for Smart Environment and Integrated Ecosystem	Renu Thapliyal, <b>Ravi Kumar Patel</b> , Ajit Kumar Yadav, Akhilesh Singh	International Journal of Engineering and Technology; 7.3.12 (2018): 1219-1221
6. 3D Printing: It's Microfluidic Functions and Environmental Impacts	Abhishek Sharma, Surajit Mondal, Amit Kumar Mondal, Soumadeep Baksi, <b>Ravi Kumar Patel</b> , Won-Shik Chu, Jitendra K. Pandey	International Journal of Precision Engineering and Manufacturing Green Technology; 4.3 (2017): 323-334, <i>IF: 4.561</i>
7. Onset of triply diffusive convection in a Maxwell fluid saturated porous layer with internal heat source	Mukesh Kumar Awasthi, Vivek Kumar and <b>Ravi Kumar Patel</b>	Ain Shams Engineering Journal; 9.4 (2018): 1591-1600, <i>IF: 3.091</i>

## B. Conference

1. Classification of stutter through Machine Learning for Indian languages  
Meera C.S, R.V. Kashyap, Jagriti Mishra, Vinit, Varnita Verma, **Ravi Kumar Patel**  
**National Conference** on Application of Indian Languages in Robotics, on 8th March, 2019
2. Nanotechnology for water treatment  
Jitendra K. Pandey and **Ravi Kumar Patel**  
Nanocon 2018, 4th **International Conference** on Nanotechnology Applications, Advances and Innovations.
3. Experimental analysis of 3D printed Microfluidic device for detection of adulteration in fluids  
**Ravi Kumar Patel** and Mukesh Kumar Awasthi  
**International Conference** on Nano for Energy and Water (NEW) & Indo French Workshop on Water Networking, Energy Procedia: **Springer**
4. Comparative Analysis of Floating Aerogenerators  
Amit Kumar Mondal, **Ravi Kumar Patel**, Abhishek Sharma, Vindhya Devalla and Surajit Mondal  
**International Conference** on Nano for Energy and Water (NEW) & Indo French Workshop on Water Networking, Energy Procedia: **Springer**
5. Investigation on optimized relative localization of a mobile robot using regression analysis  
Abhishek Sharma, **Ravi Kumar Patel**, Vikas Thapa, Beena Gairola, Bhupesh Pandey, Barre Alex Epenetus, Sushabhan Choudhury and Amit Kumar Mondal  
2016 **International Conference** on Robotics: Current Trends and Future Challenges (RCTFC)
6. A novel design of Inexpensive, Heavy Payload and High Mobility ORQ robot  
Praveen Kumar, Parag Verma, Rajesh Singh and **Ravi Kumar Patel**  
**International Conference** on Intelligent Communication, Control and Devices 2016; **Springer**

### **C. Book Chapter**

1. Wearable Fitness Band Based U-Health Monitoring **Ravi Kumar Patel**, Akash Gupta, Vinay Chowdary, Vivek Kaundal, Amit Kumar Mondal Sensors for Health Monitoring; **Elsevier**

### **ACCOLADES**

- Scholarship by Indo-French Centre for the Promotion of Advanced Research (IFCPAR), Ministry of Science and Technology, Government of India for international visit to Collaborators
- Research Reward from R&D UPES for publication of peer-reviewed research articles.
- Presented research work to BIRAC, Department of Biotechnology, and Government of India.

### **MEMBER OF PROFESSIONAL BODIES**

- ✓ International Association of Engineers (IAENG) - 250434
- ✓ American Chemical Society (ACS) – 32182098

# DEVELOPMENT OF NANOPARTICLES LOADED 3D PRINTED MICROCHANNEL FOR FLUORIDE REMOVAL FROM WATER

## ORIGINALITY REPORT

8%

SIMILARITY INDEX

4%

INTERNET SOURCES

7%

PUBLICATIONS

4%

STUDENT PAPERS

## PRIMARY SOURCES

- 1 Leonard D. Tijing, John Ryan C. Dizon, Idris Ibrahim, Arman Ray N. Nisay, Ho Kyong Shon, Rigoberto C. Advincula. "3D printing for membrane separation, desalination and water treatment", Applied Materials Today, 2020  
Publication 2%
- 2 Hammed Abiodun Balogun, Reyihangu Sulaiman, Sarah Sayed Marzouk, Adewale Giwa, Shadi Wajih Hasan. "3D printing and surface imprinting technologies for water treatment: A review", Journal of Water Process Engineering, 2019  
Publication 2%
- 3 [www.un-ihe.org](http://www.un-ihe.org)  
Internet Source 1%
- 4 Jadhav, Sachin V., Eugenio Bringas, Ganapati D. Yadav, Virendra K. Rathod, Inmaculada Ortiz, and Kumudini V. Marathe. "Arsenic and fluoride contaminated groundwaters: A review of current technologies for contaminants removal", 1%